NASA CR 54664
HTL TR No. 70

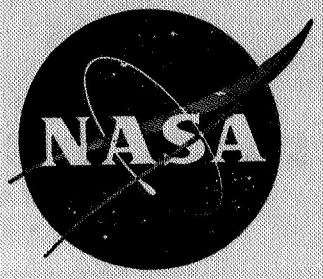

THERMAL ANALYSIS OF CATHODE AND ANODE REGIMES OF AN MPD-ARC

by

K. T. SHIH, E. PFENDER AND E. R. G. ECKERT

prepared for

NATIONAL AERONAUTICS AND SPACE ADMINISTRATION

HEAT TRANSFER LABORATORY
MECHANICAL ENGINEERING DEPARTMENT
UNIVERSITY OF MINNESOTA

NASA CR-54664
HTL TR No. 70

Summary Report

Thermal Analysis of Cathode and Anode Regimes of an MPD-Arc

by

K.T. Shih, E. Pfender and E.R.G. Eckert

Prepared for

National Aeronautics and Space Administration

January, 1968

Contract NAS 3-2595

Project Manager
NASA-Lewis Research Center
Spacecraft Technology Procurement Section
S. Domitz

HEAT TRANSFER LABORATORY
DEPARTMENT OF MECHANICAL ENGINEERING
UNIVERSITY OF MINNESOTA
MINNEAPOLIS, MINNESOTA

FOREWARD

This report summarizes the work done by the High Temperature Laboratory of the Heat Transfer Division, Department of Mechanical Engineering, University of Minnesota, Minneapolis, Minnesota, during the fourth year of a research program sponsored by the National Aeronautics and Space Administration, Lewis Research Center, Cleveland, Ohio, under Contract No. NAS 3-2595. In the first part of this program the contract's technical project manager was Mr. J. Sovey of the Spacecraft Technology Division, Lewis Research Center. During the last part of this program the contract's technical project manager was Mr. S. Domitz of the Spacecraft Technology Procurement Section, Lewis Research Center. The report covers work conducted from June 1965 to January 1967.

The authors wish to express their sincere thanks and appreciation to R. C. Erickson for his contribution to this work, and to the members of the Heat Transfer and Research Shops for their supreme efforts to complete the modification of the arc tunnel. The many helpful contributions by the other members of the Heat Transfer Division are also acknowledged. Thanks are expressed to Mr. H. Hunczak and Mr. S. Domitz of the Lewis Research Center for a number of informative discussions.

ABSTRACT

A new test chamber which was incorporated into an existing arc tunnel test facility was especially designed and constructed for anode heat transfer studies in MPD-arc configurations. Three different axially symmetric anode designs of the same overall dimensions were used in the experimental program, namely a solid anode (Configuration 1), a longitudinally segmented anode (Configuration 2) and an axially segmented anode (Configuration 3). Anode heat transfer and current distribution data were taken over a wide range of parameters (arc current, mass flow rate, pressure, magnetic field strength, cathode position) with these three configurations, using argon and ammonia as working fluids.

The experimental results show that there is a linear relationship between the anode heat fluxes and the arc currents corresponding to a proposed heat transfer model for the anode. With increasing mass flow rate a transition from laminar to turbulent flow seems to occur as indicated by the appearance of the plasma plume emanating from the anode orifice. This transition has a severe influence on the observed anode heat fluxes, especially at low pressure levels. A slight increase of the anode heat fluxes is observed with increasing magnetic field strength.

The current and heat flux distribution determined with an axially segmented anode is found to be affected by the mass flow rate, the magnetic field strength and the cathode position.

TABLE OF CONTENTS

Section	Title	Page
	FOREWORD	ii
	ABSTRACT	iii
	TABLE OF CONTENTS	iv
	NOMENCLATURE	vi
I.	INTRODUCTION	1
II.	THE ARC PLASMA	5
	A. Arc Column	6
	B. Anode Phenomena	7
	C. Cathode Phenomena	8
	D. MPD Arcs	9
III.	HEAT TRANSFER MODELS	10
	A. Heat Balance	10
	B. Anode Heat Transfer	10
	C. Cathode Heat Transfer	15
	D. Thermal Efficiency	16
IV.	ARC TUNNEL FACILITY	18
	A. Arc Tunnel Description	18
	B. Longitudinally Segmented Anode	20
	C. Axially Segmented Anode	21
	D. Magnet	21
	E. Auxiliary Equipment	22
	F. Instrumentation	22
V.	EXPERIMENTAL RESULTS	24
	A. Overall Heat Balance	25
	B. Arc Behavior and Anode Heat Transfer	26

Section	Title	Page
	C. Arc with Zero Mass Flow Rate	29
	D. Longitudinally Segmented Anode	31
	E. Axially Segmented Anode	45
	F. Experiments in Ammonia	48
VI.	SUMMARY	49
	REFERENCES	51
	TABLES	54
	FIGURES	
	DISTRIBUTION LIST	

NOMENCLATURE

Symbol	Unit	Definition
A	cm^2	area
b	cm^2/V-sec	mobility
B	gauss	magnetic field strength
c_p	kJ/kg-K	specific heat of gas at constant pressure
d	cm	diameter of anode orifice
e	amp-sec	electron charge
E	V/cm	electrical field strength
h	g/cm^2-sec	heat transfer coefficient based on enthalpy difference
i	kJ/kg	enthalpy
I	amp	current
j	amp/cm^2	current density
k	kJ/K	Boltzmann constant
l	cm	length of the arc column
L	cm	length of the tungsten cathode tip
Le		Lewis number
m	g	mass
$\dot{m}$	g/sec	mass flow rate
n	cm^{-3}	number of particles per unit volume
Nu		Nusselt number
P	mmHg	chamber pressure
Pr		Prandtl number
q	kW/cm^2	heat flux per unit area
Q_A	kW	total heat transfer to anode
Q_C	kW	total heat transfer to cathode
Q_{Conv}	kW	heat transfer to anode by convection

Symbol	Unit	Definition
Q_{CR}	kW	heat transfer to anode by convection and radiation
Q_G	kW	heat transfer to the gas
Q_R	kW	heat transfer by radiation from cathode to anode
r	cm	radius of cathode
Re		Reynolds number
T	K	temperature
U	volt	arc voltage
U_a	volt	anode fall
U_A	volt	characteristic anode voltage defined by equation (18)
U_{AV}	volt	available voltage, defined by equation (21)
U_c	volt	cathode fall
U_C	volt	characteristic cathode voltage defined by equation (19)
U_{Conv}	volt	defined by equation (22)
U_{CR}	volt	defined by equation (22)
U_I	volt	defined by equation (14)
U_i	volt	ionization Potential
U_R	volt	defined by equation (22)
v	cm/sec	drift velocity
V	cm/sec	gas velocity
w	cm/sec	thermal velocity
ε		emissivity
ϕ	volt	work function
κ	kW/cm-K	thermal conductivity
λ	cm	mean free path
μ	g/cm-sec	viscosity

Symbol	Unit	Definition
ρ	g/cm^3	density
σ	$kW/cm^2\text{-}K^4$	Stefan-Boltzmann constant
η	%	thermal efficiency

Subscripts

a	anode surface
c	cathode surface
e	electron
i	ion
s	plasma stream
r	radiative

I. INTRODUCTION

The Heat Transfer Laboratory at the University of Minnesota has been engaged for a number of years in a program of theoretical and experimental investigation of heat transfer phenomena occuring in electric arcs. In the development of arc plasma devices, special problems arise due to the intense heat fluxes into the electrodes. In order to gain a basic understanding of the heat transfer mechanisms and their parametric dependence, the Heat Transfer Laboratory started, in December 1961 under the sponsorship of NASA, a long-range research program in the specific area of high-temperature plasmas generated by electric arcs. The primary purpose of these investigations has been to study the basic heat transfer phenomena as they occur in electric DC arc plasmas with particular attention being focused upon the anode regimes. It is felt that such a basic understanding of the fundamental process involved will then permit the prediction, at least on a qualitative scale, of the heat transfer in various other situations.

Due to the complex nature of the physical phenomena and the limited access afforded by the geometries of electric arc plasma devices, it was imperative to start the research where at least the geometries involved were simple and well defined. Therefore, the first electrode geometry investigated was a free-burning, high intensity DC arc operated between a plane, water-cooled, tungsten cathode arranged with its axis normal to the plane of the anode. These electrodes were mounted in a spherical test chamber which permitted unobstructed viewing of the plasma column as well as of the cathode and anode regimes.

The following measurements were taken using argon as working fluid in a pressure range between 20 mmHg and 1 atmosphere for various electrical input powers up to 20 kW:

1. Total energy flux to the anode and establishment of an overall energy balance for the arc.
2. Temperature distributions in the arc plasma by spectroscopic means.
3. Distribution of local energy and current flux into the anode.
4. Total arc radiation to its surroundings.
5. Establishment of a cathode energy balance.

The results of these measurements were reported in the Summary Report which was submitted to NASA in 1963 (1).

The second electrode geometry selected for these studies consisted of a plane, water-cooled, copper anode and a tungsten cathode which could be positioned with its axis either normal or inclined to the anode surface. In addition, a free jet gas stream was directed parallel to the surface of the anode with different velocities in order to study the influence of such a gas flow on the heat fluxes using various power inputs and gases. The entire assembly was again mounted in a spherical test chamber. This second geometry was thought to represent the best compromise between the situation encountered in plasma generators and the accessibility of a simple model, because the flow conditions are quite similar to those of nozzle-shaped anodes of a number of plasma generators while all the previous tools and methods of investigation can still be applied.

The experiments performed with the second geometry were

mainly of a qualitative nature, and the results of these experiments are also included in the report mentioned before (1). It was determined that the experimental apparatus in the spherical test chamber had several limitations both from a scientific and an economic viewpoint. First, the size of the blow-down type free jet was too small to encompass the entire arc in a uniform flow field. Second, since the test chamber had to be exhausted into the atmosphere -- our vacuum system was too small to handle the required amount of low pressure gas -- tests could only be performed at atmospheric or higher pressures. Finally, the blowing velocities needed for meaningful results turned out to be higher than expected, requiring unreasonable quantities of cylinder gas.

It was necessary, therefore, to construct an arc tunnel in order to more adequately carry out the aims of the experimental part of the ensuing research program. With this arc tunnel it has been possible to adjust the independent parameters such as arc current, gas flow velocity, gas pressure, and arc electrode spacing, over a wide range. In addition, different gases and cathode-anode shapes and orientations may be utilized. Another important feature of the arc tunnel is its large window opening which provides unobstructed viewing of the entire arc including the cathode and anode attachment regimes.

In the Summary Report submitted to NASA in 1964 (2), the arc tunnel and its instrumentation were described in detail. The following measurements were performed in the arc tunnel using argon as working fluid:

1) Cold-flow velocity profiles in the test section were

determined and the flow uniformity was established.

2) The general behavior of the arc with superimposed axial flow was investigated by applying high-speed photography combined with electrical measurements.

3) The influence of the cathode orientation and of the gas flow on the overall energy balance of the arc were studied at different parameter settings.

In addition, some preliminary tests in a hydrogen atmosphere were performed which demonstrated that a hot anode permits a more diffuse arc attachment than is commonly observed with water-cooled anodes.

In the Summary Report submitted in 1965 (3), several new anode configurations were described and a number of measurements were performed in the arc tunnel using argon and hydrogen as working fluids. The following results were obtained:

1) The arc disclosed two impinging electrode jets which are strongly affected by current and pressure settings.

2) The transition from the steady mode to the fluctuating mode with restriking may be described by a critical Reynolds number.

3) Another operational mode of the arc with superimposed argon flow has been found which is designated the "fluctuating mode with takeover."

4) The percentage of heat transferred to the anode is nearly independent of the current in the higher current range.

5) By means of an optical system built for viewing the arc, the temperature distribution at atmospheric pressure in

the cathode column was determined.

The purpose of this report is to summarize the work performed during the fourth year of this research program. In order to carry out the experimental program in a MPD arc configuration using argon and ammonia, it was necessary to extensively modify the existing arc tunnel. Several new anode configurations were designed and constructed. The research efforts of this period were mainly devoted to the study of the energy transfer to the anode with superimposed axial mass flow and magnetic field using various anode designs over a certain range of parameter settings.

A brief review of the fundamentals of electric arcs and the modes of energy transfer to electrode surfaces is also included.

II. THE ARC PLASMA

Gases, at room temperature, are normally poor electric conductors. However, the application of a sufficiently high electric field may cause a breakdown of the insulating properties, after which large currents may be passed through the gas. The phenomemon which is associated with the passage of a current through the gas is called electrical discharge and depends markedly on the nature and pressure of the gas, on the materials and geometry of the electrodes, and on the magnitude of the current. Various types of discharges with characteristic features are given special names, as for example Townsend discharge, corona discharge, glow discharge, and so on. An "arc discharge" denotes, in general, a discharge of relatively large

current (greater than 1 amp) and small cathode fall (4, 5).

Three distinct regions can be recognized in an electric arc (Fig. 1). The arc column (main part of the arc), is characterized by an almost constant electric field strength and is bordered by two regions near the electrodes which are characterized by sharp potential drops within a thin sheath. The regions in which this occurs are called the anode fall and the cathode fall. Since these three distinct regions have dominant effects on the electrode heat transfer, they will be discussed separately in the following paragraphs.

A. Arc Column

The plasma consists of a mixture of electrons, ions, and neutral particles. Except for the regions very close to the electrodes, the plasma is electrically neutral. For the case in which the ions, present in the arc, are singly charged, $n_e = n_i$. Under the influence of an electric field, E, the electrons and ions move parallel to the electric field with drift velocities v_e and v_i. The current density j may be expressed as

$$j = j_e + j_i \ , \quad j_e = en_e v_e \ , \quad j_i = en_i v_i \tag{1}$$

The drift velocities may be calculated from the equations (6)

$$v_e = b_e E \quad \text{and} \quad v_i = b_i E \tag{2}$$

where b_e and b_i denote the electron and ion mobilities defined as

$$b_e = \frac{e\lambda_e}{m_e w_e} \quad \text{and} \quad b_i = \frac{e\lambda_i}{m_i w_i} \tag{3}$$

The thermal velocities w_e and w_i are calculated from the equation

$$\tfrac{1}{2}mw^2 = \frac{3}{2}kT \tag{4}$$

In the column where under certain conditions thermal equilibrium may be assumed

$$\frac{j_i}{j_e} = \frac{b_i}{b_e} = \frac{\lambda_i m_e w_e}{\lambda_e m_i w_i} \cong \frac{1}{4\sqrt{2}} \sqrt{\frac{m_e}{m_i}} \tag{5}$$

In deriving equation (5) it is assumed $\lambda_i \cong \lambda$, $\lambda_e \cong 4\sqrt{2}\lambda$ (6). Since $m_i >> m_e$, within the arc column the ion current is negligible as compared with the electron current. In the case of argon, one obtains from equation (5) $j_i/j_e \cong 0.66\text{x}10^{-3}$.

B. Anode Phenomena

The anode fall is a transition region, both electrically and thermally, between anode surface and anode column. The thickness of the anode sheath in a high intensity arc comprises several electron mean free paths (7). Within this region the following tasks must be performed:

1. Ions must be generated which diffuse in the direction of the cathode.
2. The directed velocity of the ions accelerated in the anode fall must be changed into a thermal velocity distribution.
3. The transition of the relatively low temperature of the

anode surface to the high plasma temperature must take place.

These requirements necessitate in the anode fall region an increased field strength over the column values, rapidly changing temperature and, therefore, departure from thermal equilibrium.

The basic physical processes in the anode fall region are still poorly understood. This is due to the lack of reliable and consistent experimental data, and because little theoretical work has been done. According to Hoecker and Bez (7) the ion production in the anode sheath may occur either by field ionization or by thermal ionization. In the first case a potential drop across the sheath equivalent to at least the first excitation potential of the gas forming the arc atmosphere is required. In the second case the potential drop across the sheath may be smaller than the first excitation potential. In either case, a certain electric field energy is required for the production of ions.

The results of anode fall measurements vary widely with arc parameters and conditions, such as arc current, temperature, pressure and composition of gases, and anode materials. For a comprehensive review of these experiments and theoretical analyses, see references (4) and (8).

C. Cathode Phenomena

The situation at the cathode is even more complex due to the flow of an ion current to the cathode and the emission of electrons from the cathode. In the cathode fall space charge carrier (ion and electron) production by colliding electrons takes place. The primary electrons are emitted from the cathode.

These primary electrons may be extracted from the cathode in several different ways. They may be emitted directly as thermionic emission (T-emission) current in which the cathode heating is provided by ions impinging on the cathode surface, or by the action of a strong electric field (F-emission), or a combined effect (T F-emission). It has also been suggested that a highly ionized layer of gas or vapor close to the cathode may supply a large fraction of the cathode current in the form of positive ions (4, 5). However in many cases the actual mechanism is still unknown.

D. MPD Arcs (9)

A schematic diagram of a MPD arc thrustor is shown in Figure 2. The working fluid is injected through the annular gap between the cathode and the anode. This fluid is accelerated both by aerodynamic and magneto-plasma-dynamic forces as it passes through the discharge and expands into the vacuum. The details of the acceleration mechanisms are quite complex (10) and beyond the scope of this work.

The interaction of the arc with the superimposed mass flow and the applied magnetic field further complicates the already complex arc phenomena. Although many interesting investigations have been conducted related to the interaction of the arc with aerodynamic and/or magnetic fields (11), most investigations are limited to the effects in the plasma itself and to overall arc behavior. The dimension of the electrode falls precludes the application of diagnostic tools in these regimes. Therefore, no data of local measurements within the fall regions are available.

III. HEAT TRANSFER MODELS

A. Heat Balance

Overall heat balance measurements were performed in order to determine the gross heat flux to the anode, the cathode, and to the gas, as a function of different parameter settings. Since the purpose of the arc is in many applications to produce a stream of intensely heated gas, heat transfer to anything but the gas is considered as a loss.

Experimental results have shown that the main energy loss experienced by an arc is due to the anode heat flux. The heat losses to the cathode and to the surroundings are frequently comparatively small; hence these studies are mostly concerned with anode heat transfer.

B. Anode Heat Transfer

In this section, a model for the heat transfer to the anode is proposed. It is based on a previous method developed in the Heat Transfer Laboratory of the University of Minnesota (12, 13), although some different assumptions are made.

The heat transfer to the anode of an electric arc involves a variety of transfer process, such as heat transfer by convection, radiation, by the electrons, and by some other mechanisms (8, 14) which will be discussed separately in the following paragraphs.

1. Heat transfer by convection: Convective heat transfer in a high temperature gas is calculated with a heat transfer coefficient based on enthalpies (15) according to the equation

$$Q_{Conv} = h_a A_a (i_s - i_a) \tag{6}$$

The heat transfer coefficient h_a is expressed in dimensionless form as

$$Nu = \frac{h_a c_p d}{\kappa} = Nu(Re, Pr) \tag{7}$$

A necessary condition for the validity of equations (6) and (7) is that the Lewis number, Le, defined as

$$Le = \frac{\rho c_p d}{\kappa}$$

does not differ very much from the value of one.

2. Heat transfer by radiation: The following radiative heat processes are considered here: (a) plasma to anode, (b) anode to surroundings, (c) cathode to anode.

(a) A fraction of the radiation energy emitted by the arc plasma impinges upon the anode surface. A certain portion of it is reflected and the rest is absorbed by the anode surface. For plasmas which are of interest in this report there are two types of radiation: line radiation arising from bound-bound transitions and continuum radiation from free-free and free-bound transitions. The measurements of Petschek et al. (16) in ionized argon produced by shock waves show that the contribution of the line-radiation to the radiative flux is small compared to the continuum radiation. The measurements of Schoeck (12) show that the arc radiation contributes very little to the anode heat

transfer even at atmospheric pressures. In view of the rather low pressures utilized in this work, the radiation heat transfer from the plasma to the anode may be neglected.

(b) The anode surface itself emits radiation into the surrounding space. The radiation emitted per unit time and surface area of the anode is

$$q_r = \varepsilon\sigma T^4 \tag{8}$$

where ε denotes the emissivity of the anode surface, and $\sigma = 5.61\text{x}10^{-15}$ kW/cm^2 ^oK is the Stefan-Boltzmann constant. Assuming $\varepsilon = 1$ and $T_a = 1{,}000^oK$, an upper limit of the emitted radiation is obtained as $q_r = 5.6\text{x}10^{-3}$ kW/cm^2, which is negligible compared with the magnitude of the total anode heat fluxes.

(c) At low pressure, a larger portion of the cathode upstream from the cathode tip is heated by the arc and, therefore, a certain amount of radiant energy will be transferred from the cathode to the anode. The situation at the cathode, simulating the conditions of MPD arcs, has been investigated by Hügel, Kruelle and Peters (17), and they found that the pressure has a pronounced effect on the arc attachment area which decreases considerably with increasing pressure. Increasing current leads to higher cathode temperatures and to larger attachment areas. Increasing mass flow rate causes slightly increasing arc attachment areas and an insignificant decrease of the cathode temperature.

In order to determine the energy emitted from the cathode, the temperature distribution of the cathode has to be known. A

measurement of such a temperature distribution is quite involved and is not included in this work. An estimation of the energy emitted from the cathode will be presented in section V.D.5.

3. Energy transfer by electrons: The electrons enter the anode surface with a thermal energy corresponding to the electron temperature in the plasma column in the vicinity of the anode surface plus the energy gained through the anode fall. In addition, an amount of energy proportional to the work function of the anode material, comparable with a condensation energy, appears also as an energy input. The equation for the total energy carried by electron currents into the anode can be derived by considering an energy balance of electrically charged particles near the anode surface (Figure 3). Let the control volume be bounded between the anode sheath and the anode surface. Neglecting energy transfer in the direction parallel to the anode surface, the number of electrons, j_e/e, entering the anode surface per unit time and area from the arc column carry an enthalpy $5kT_e/2$ per electron, plus the kinetic energy due to the electron drift velocity $\frac{1}{2}m_e v_e^2$ gained in the anode fall. (Eberhart (18) has shown that the electron drift kinetic energy in an arc column is much less than the electron enthalpy term, hence it is neglected.) The electrons and ions representing the total current density $j = j_e + j_i$ acquire an amount of energy jU_a in the anode fall region. Of this energy the fraction $j_i U_i$ is used to produce ions. Including the condensation energy of the electrons which penetrate the anode surface, $j\phi_a$, and neglecting the energy loss by elastic collision within the anode fall region, the electron anode energy transfer is then

$$q_{ea} = \frac{j_e}{e}\frac{5}{2}kT_e - \frac{j_i}{e}\frac{5}{2}kT_i + jU_a - j_iU_i + j\phi_a \qquad (9)$$

where q_{ea} is the anode heat flux carried by electrons. The quantities on the right-hand side of equation (9) represent in sequence the enthalpy flux due to the electron current from the plasma column into the control volume, the enthalpy flux of the ion current out of the control volume into the plasma column, internal heat generation due to the anode fall, absorption of energy by the ionization process and the electron condensation energy. Since $j_e >> j_i$ (see section II.A), $T_e \geq T_i$, and $U_i = 0$ $(U_a + \phi_a)$ equation (9) can be simplified to

$$q_{ea} = j(\frac{5k}{2e}T_e + U_a + \phi_a) \qquad (10)$$

Integrating over the total anode area yields

$$Q_{ea} = I(\frac{5k}{2e}T_e + U_a + \phi_a) \qquad (11)$$

In performing the integration it is assumed that T_e, U_a, and ϕ_a are constant over the anode area. Otherwise average values should be used.

4. Heat transfer by other mechanisms: Since the anode surface temperature was kept below the melting point of copper and no appreciable erosion of the anode surface could be detected, ablation of the anode may be neglected. Joule's heat generated in the anode by the current flow itself is also negligible.

The anode energy balance is now completed with the assumption that the energy transferred to the anode is found as heat in the

calorimetric fluid.

5. Anode heat balance: The results of the previous section are now collected and equated to Q_A, the total heat input to the anode

$$Q_A = Q_{Conv} + Q_R + I(\frac{5k}{2e}T_e + U_a + \phi_a) \tag{12}$$

By denoting

$$Q_{CR} = Q_{Conv} + Q_R \tag{13}$$

$$U_I = \frac{5k}{2e}T_e + U_a + \phi_a \tag{14}$$

equation (12) can be reduced to

$$Q_A = Q_{CR} + U_I I \tag{15}$$

which shows that the heat flux to the anode, Q_A, is linearly related to the arc current, I, provided that Q_{CR} and U_I do not depend on the current or that their current dependence may be described as a second order effect. Experiments are conducted in order to verify this anode heat transfer model and to determine the quantities in equation (15).

C. Cathode Heat Transfer Model

The energy balance at the cathode is more involved due to the existence of an ion current and the emission of electrons. An ion which impinges on the cathode surface transfers thermal

energy to the cathode according to the accommodation coefficient. Besides their thermal energy, the energy gained through the cathode fall may also at least partially be transferred to the cathode. Each ion arriving at the cathode surface uses up one emitted electron for its own neutralization. This process releases an amount of energy proportional to the ionization potential. The total electron current emitted by the cathode is in part used for neutralization of ions and provides in addition, free electrons necessary to maintain the arc. The emitted electrons cool the cathode by an amount proportional to the work function of the cathode material. By including convective heat transfer and radiation losses and assuming an accommodation coefficient of unity, which is only approximately true for heavy ions (19), the net heat input to the cathode is given by

$$Q_C = h_c A_c (i_s - i_c) - Q_R + I_i (\frac{5k}{2e} T_i + U_i + U_c) - I\phi_c \qquad (16)$$

In this work only measured net heat fluxes to the cathode are reported. No attempt has been made for a more detailed study of the cathode heat transfer, because it is less important compared with the heat transfer to the anode.

D. Thermal Efficiency

The thermal efficiency of an MPD arc thrustor is defined by

$$\eta = 1 - \frac{\text{Energy loss}}{\text{Power input}} \qquad (17)$$

The power input to the arc equals the product of the arc voltage, U, and the arc current, I. Neglecting heat losses to the sur-

roundings, and defining a characteristic anode voltage, U_A, and a characteristic cathode voltage, U_C, as

$$U_A = \frac{Q_A}{I} \tag{18}$$

$$U_C = \frac{Q_C}{I} \tag{19}$$

the thermal efficiency can be written in the form

$$\eta = 1 - \frac{U_A + U_C}{U} \tag{20}$$

In order to increase the thermal efficiency the ratio of the voltage describing the electrode losses to the overall arc voltage should be reduced. It is convenient to define the voltage available for heating and accelerating the propellant, U_{AV} as

$$U = U_{AV} + U_A + U_C \tag{21}$$

also let

$$U_{CR} = Q_{CR}/I, \quad U_{Conv} = Q_{Conv}/I, \quad U_R = Q_R/I \tag{22}$$

then

$$U = U_{AV} + U_I + U_{CR} + U_C \tag{23}$$

and equation (20) becomes

$$\eta = U_{AV}/U \tag{24}$$

IV. ARC TUNNEL FACILITY

A. Arc Tunnel Description

A number of major modifications were made to adapt the arc tunnel facility for the proposed experiments. A new test chamber was built permitting the installation of a magnet and the operation as an open flow system. The general layout of the arc tunnel is shown schematically in Figure 4. The tunnel consists of a blower, a venturi tube, a test chamber with the arc thrustor mounted on the inside of the end flange, control valves, and vacuum pumps. Welded aluminum construction is used throughout, and 0-ring seals are employed in all joints and flanges. The tunnel is arranged so that it can be operated as either a closed-loop or an open-loop device.

The gas flow is provided by a 10 x 9 Roots-Connersville blower unit for the closed-loop operations. The blower delivers approximately 700 cfm when operated at a speed of 720 RPM. The flow rate is controlled by means of a throttling valve and a by-pass valve. A venturi tube serves for flow measurements. For the open-loop operations, a valve in front of the upstream plenum chamber is closed, the working gas is injected through the thrustor, and the exhaust is pumped out of the system by a vacuum pump. In the present investigations, closed-loop operation is used only during the arc starting process.

Figure 5 shows the arc jet assembly. The upstream plenum chamber is made of a 10-cm aluminum tee with welded flanges.

It acts as a settling chamber as well as a cathode housing. The inlet section consists of a converging nozzle, made of teflon, 20 cm O.D. and 10 cm long. This teflon piece also provides sixteen water passages and eight electrical connections to the different anode segments. Figure 6 shows the teflon piece which holds the anode sections and contains the water passages.

The anode (Configuration 1) consists of a brass holder and a copper insert. The brass holder (Figure 6) is 7.5 cm O.D. and 5 cm long. A magnet can be situated and slid along the holder. The inside diameter of the anode can be readily changed by installing a different size copper insert. A 1.27 cm I.D. insert is used for these experiments.

The design of the anode and its holder incorporates several useful features. First, the entire assembly can be easily removed. Second, eroded copper anode inserts may be simply exchanged. Finally, a segmented anode (Configurations 2 and 3) which retains only the general outline of the anode holder can be readily installed. In this study all three anode configurations had the same internal dimensions given in Figures 5, 8 and 9.

The thoriated (2%) tungsten cathode is held parallel to and in the center of the anode by means of a special water-cooled cathode holder. The cathode tip is adjustable in all three dimensions. The diameter of the tunsten cathode can be changed by changing the tungsten insert. A 0.64 cm diameter hemispherical tip tungsten insert was used first (for data presented in Table 1 only). However, due to excessive erosion, the tungsten tip diameter was later enlarged to 0.95 cm.

The anode assembly protrudes into a double wall, water-

cooled, welded, aluminum chamber of 60 cm inside diameter and a length of 136 cm. Four 25 cm diameter and two 15 cm diameter openings are located around the test chamber for optional use as viewing windows and/or feed throughs.

The heat exchanger is a finned-tube device manufactured by the Trane Company and has specially made copper heads and a non-magnetic alloy casing to avoid magnetic field distortions.

A throttling valve is located between the test chamber and the return pipe (see Figure 4) to help control the pressure in the test chamber. Figure 7 pictures the final assembly of the arc tunnel.

B. Longitudinally Segmented Anode (Configuration 2)

The longitudinally segmented anode is shown schematically in Figure 8 and photographically in Figure 8a. There are eight segments in all, each isolated both electrically and thermally from adjacent segments by means of a 10-mil thickness of "Burnil" paper, a synthetic mica manufactured by the 3M Company. In addition, all segments have been relieved approximately 0.025 cm on their adjoining surfaces so that only a small rim around the edges actually touches the Burnil paper. This leaves a dead-air space between segments which further decreases the heat exchange between segments. The current lead for each segment is brought out through a connecting bolt at the base of each segment.

Each segment is made of copper and has water passages drilled in it. The water flow is connected in series, and a thermocouple is located at the inlet of the first and the outlet of all segments in order to measure the temperature rise of the

cooling water for calorimetric purposes.

C. Axially Segmented Anode (Configuration 3)

The axially segmented anode is shown schematically in Figure 9 and photographically in Figure 9a. This anode configuration consists of four segments cut perpendicular to the electrode center line. Each segment is isolated both electrically and thermally from neighboring segments by means of a 10-mil thick Burnil paper making use of the same provisions as for the longitudinally segmented anode to keep the heat exchange between segments as small as possible. The current lead is brought out through a connecting bolt at the base.

Each segment is made of copper with a .48 cm O.D. copper tube soldered around to provide water cooling. The cooling circuits are connected in series, and thermocouples are located at the inlet of the first and at the outlet of all segments to determine the temperature rise of the cooling water for calorimetric purposes.

The segmental current for the axially segmented anode was measured by calibrating the resistance of the copper tubes used as cooling water passages.

D. Magnet

The magnet is a 38 turn coil of 0.64 cm O.D. copper tubing insulated with teflon tape and wrapped with 3M Glass Cloth Electrical Tape. The coil is cooled with city water which is able to remove about 5 kW.

A water-cooled shield is placed over the front face of the magnet to protect the insulation of the coil from possible over-

heating by the plasma jet.

E. Auxiliary Equipment

The auxiliary system layout is shown in Figure 10. The electrical power for the arc is supplied by a 200 kW American rectifier and/or a 40 kW Miller rectifier.

The initial pump-down of the arc tunnel is accomplished by means of a Dresser Vacuum DPD4-1000B oil diffusion pump connected to a NRC 40 cfm mechanical vacuum pump. A liquid nitrogen cold trap is placed between the diffusion pump and the arc tunnel as shown in Figure 4.

A Dresser Vacuum DS-300 mechanical vacuum pump is installed in order to provide sufficiently high gas flow rates at low pressure for open-loop studies.

The argon and ammonia gases are provided from commercial gas cylinders with the usual valves and pressure regulators.

Cooling for the anode is accomplished with a high-pressure, distilled water system while the remaining portions of the arc tunnel are cooled with city water. A Masonneilan pressure regulator was installed to regulate the city water pressure.

F. Instrumentation

For closed-loop operation, the gas flow rate, $\dot{m}$, is determined by measuring the pressure drop across the venturi tube. The pressure measurement is made with a standard U-tube manometer. Dibutyl phthalate (Meriam fluid number D-3116) having a specific gravity of 1.04 at standard conditions is used in the manometer because a low vapor pressure oil is required to keep the arc tunnel clean. The venturi tube has been calibrated

using a pitot-static probe.

For open-loop operations, the flow rate is measured with a standard Fisher and Porter flowrator accurate to ±2 percent of full scale.

The test section pressure is measured to within ±0.5 mmHg with a Wallace and Tierman model FA-173, absolute pressure mercury manometer. Between every manometer and the arc tunnel, cold traps are installed, filled with liquid nitrogen to prevent backflow of oil and mercury vapor during evacuation.

A thermocouple type vacuum gauge, model DTG-101, manufactured by Dresser Vacuum is used to measure the rough vacuum pressure. For the high vacuum, an ionization gauge, model RG-75 K, manufactured by Veeco Instrument, Inc. is employed.

The cooling water flow rates are measured with standard Fisher and Porter flowrators. These flowrators have been individually calibrated in our laboratory and are considered to be accurate to within ±1 percent of full scale.

The thermocouples are made of 30 gauge copper-constantan wire placed in a boron nitride insulator which is enclosed in a 0.32 cm stainless steel tube. All leads to the switch box are shielded with tinned braided copper wire. The locations of the thermocouples are shown schematically in Figures 5 and 10. The thermocouples have been calibrated in our Calibration Laboratory against a secondary standard which has been previously calibrated by the National Bureau of Standards.

The total and segmental arc currents are measured with a Weston external 50 mv precision shunt. The voltage drop across the shunt, the arc voltage, and the emf of the thermocouples are

measured with the aid of a Dymec Data Acquisition System consisting of an integrating digital voltmeter, amplifier, scanner and printer. The integrating digital voltmeter operates on five full scale ranges of 0.1v, 1v, 10v, 100v, and 1000v, and, by switching the sample period selector, fixed sample periods of 0.01, 0.1, or 1.0 seconds are available. The input scanner which contains 25 input channels can be set to scan from channel to channel, or automatically make a single or continuous scan of all channels in a closed-loop operation. The overall maximum error of these voltage readings is ±0.17 percent of full scale. A Tektronix model 555 oscilloscope is used to measure instantaneous voltage fluctuations.

V. EXPERIMENTAL RESULTS

Using argon as a working fluid, experiments have been conducted in two different ranges of chamber pressure. The higher range covers pressures from 10 to 100 mmHg, and the lower range covers pressures from 0.1 to 1.0 mmHg. In the intermediate pressure range, the arc is extremely unstable, and no reproducible data can be obtained. In the higher pressure range the test chamber pressure can be easily controlled while in the lower pressure range the gas flow rate and the chamber pressure cannot be adjusted independently.

Some data have been taken with the solid anode (Configuration 1) by using ammonia in the lower pressure range. The ammonia arc tends to become unstable as indicated by a sudden change of the arc mode resulting in a constricted anode attachment which

frequently destroys the anode.

One of the main difficulties experienced during the experimental program is the lack of reproducibility in arc data. It is found that the experimental data are more reproducible in the lower pressure range and above 30 mmHg, whereas in the intermediate range serious reproducibility problems are encountered. At 20 mmHg for example, the arc voltage may change from 25 to 50 volts without any obvious reason. Although several possible causes are suspected, such as impurities in the gas, electrode erosion, formation of thin surface films on the anode and the effects of cathode position (20), no conclusive explanation for this behavior can be given. However, in spite of this erratic arc behavior, the general trend of the heat transfer data is not disturbed.

A. Overall Heat Balance

Overall heat balance measurements are performed as a cross-check for the accuracy and consistency of anode and cathode heat transfer data. For such a balance heat fluxes to the anode, cathode, downstream heat exchanger and test chamber water-jacket are determined calorimetrically by measuring the flow rate and the temperature rise of the respective coolant. The total heat fluxes are compared with the power input according to the equation:

$$UI = Q_A + Q_C + Q_G \tag{25}$$

where Q_G is the heat flux absorbed by the gas and then released to the downstream heat exchanger and to the water jacket. The measurements show that the net heat flux to the cathode is much

less than the net heat flux to the anode. Therefore, more emphasis will be put on the anode heat transfer studies.

Table 1 shows that the overall heat balance according to equation (25) closes within ±5% or better indicating the accuracy which may be expected from the calorimetric heat transfer measurments. There is experimental evidence that the error is mainly due to fluctuations of the arc current and voltage. Because of the large heat capacity of the downstream heat exchanger and the water jacket, a rather long period of time is required for the establishment of a thermal equilibrium. Hence, in the latter part of this program, overall heat balances are performed occasionally for a double check of the results. For the anode heat flux measurements, near-instantaneous readings could be taken with an accuracy of about ±2%. The response time of the thermocouples (90% of reading after temperature change) is less than 0.5 sec.

B. Arc Behavior and Anode Heat Transfer

The shape of the arc and of the plasma plume is influenced by the chamber pressure, the mass flow rate of the working fluid and the current. At a pressure of 200 mmHg, in argon atmosphere, a stable cathode jet accompanied by an anode jet is observed (Figure 11). The latter moves randomly in a circumferential direction and, to a certain degree, also in a radial direction on the anode surface. The two jets are connected by a current-carrying bridge downstream of the anode nozzle exit. With decreasing pressure, the anode jet gradually disappears and the plasma plume increases both in diameter and length. Finally at a pressure of about 0.2 mmHg the plasma plume almost fills the

test chamber completely (Figure 12) and at the cathode tip a blue core appears which is probably the region of the highest temperature in the arc. Close to the anode orifice a relatively dark region exists followed by a bright plasma plume. With the application of the external magnetic field the blue core in front of the cathode becomes more intense and extends farther downstream. Figure 13 (ignore the reflection of the back window which appears in some of the pictures) shows the effects of mass flow rate of the working fluid on the plasma plume. At zero mass flow rate the shape of the plasma appears as a luminous ball originating from the cathode tip. With increasing mass flow rate the length of the plasma plume increases until a rather long laminar plume is reached. A further increase of the mass flow rate induces fluctuations in the tail of the plasma plume, and, after passing through a certain transition region, the length of the plasma plume decreases with increasing mass flow rate. It is suspected that this is caused by turbulent motion in the fringes of the plasma plume. By further increasing the mass flow rate, which is equivalent to an increase in the upstream pressure, the flow becomes supersonic and one or several Mach diamonds appear behind the tip of the cathode.

Figure 14 shows oscillograms of voltage fluctuations of the arc at different parameter settings. The voltage traces show two distinct frequency ranges. Basically, there are three different arc modes (2, 3, 21); a steady mode with no voltage fluctuations, a restrike mode with a sawtooth voltage shape, and a takeover mode with more or less sinusoidal voltage fluctuations. The steady mode is trivial and is not shown in Figure 14. The occur-

rence of the restrike mode is favored by high pressure and low current, as shown in Figure 14 at the top. The remaining oscillograms correspond to conditions which are more or less favorable for the takeover mode. For a description of these phenomena, an arc model is proposed as shown in Figure 15. The plasma plume contains an intense cathode jet, an anode jet, and a current-carrying bridge between the two jets. The arc anode attachment may move both circumferentially and radially on the anode surface. The former has no influence on the arc voltage as long as the anode surface is uniform and not contaminated, while the latter definitely causes voltage fluctuations. The current-carrying bridge between the two jets, which is exposed to a crossflow, may oscillate in the direction of the electrode axis. This represents another source of voltage fluctuations. It was first suspected that a transition from laminar to a turbulent arc plume may be closely related to the observed transition from the steady mode to the restrike or the takeover mode. A close observation, however, showed that this transition appeared before a pronounced change to the turbulent arc plume occured.

Figure 16 shows the effect of mass flow rate on the arc voltage, U, and the characteristic anode voltage, U_A (see Equation 18). At zero mass flow rate the arc voltage is very low and almost the entire power input is transferred to the anode and cathode. With increasing mass flow rate the arc voltage increases, while the characteristic anode voltage decreases. At a chamber pressure of 10 mmHg a deviation of the described trend of the arc voltage is observed, which may be due to the

previously mentioned irregular behavior of the arc at this pressure. By further increasing the mass flow rate, the arc plume seems to pass through a transition from laminar to turbulent flow. At the same time, both the values of arc voltage and characteristic anode voltage level out. This finding shows that the suspected transition of the flow has a severe influence on the anode heat transfer, especially at low pressure levels. In the laminar flow regime the thermal efficiency (see section III.D.) is a very sensitive function of the mass flow rate.

The suspected transition from laminar to turbulent flow is corroborated by the magnitude of the critical Reynolds number. If the Reynolds number is based on the anode orifice diameter, d, one obtains

$$Re = \frac{\rho V d}{\mu} \simeq \frac{4\dot{m}}{\pi d \mu} \qquad (26)$$

The critical Reynolds number calculated from (26) is found to be about 1000 - 2000 which is higher than the values reported by other investigators (22, 23).

Figure 17 shows the arc voltage and the characteristic anode voltage again as a function of mass flow rate, but with the arc current as the parameter. The arc voltages show a much stronger spread at different currents than the characteristic anode voltages, which leads to higher thermal efficiencies at lower currents.

C. Arc with Zero Mass Flow

Figure 18 shows the arc voltage, U, and the characteristic anode voltage, U_A, as a function of the reciprocal of the chamber

pressure, 1/P, with different current settings at zero mass flow rate. Some interesting results observed from these data are as follows:

1. The arc voltage is an almost linear function of both the reciprocal of the pressure and the reciprocal of the arc current. The data which are collected in Figure 18 can be represented by an empirical equation of the form

$$U = 9 + \frac{320}{I} + \frac{140}{P} \qquad (27)$$

(I in amps and P in mmHg)

Since the arc voltage is the sum of the anode fall, the integral of the electrical field strength over the length of the arc column and the cathode fall, one obtains

$$U = U_A + \int_0^1 E dx + U_C \qquad (28)$$

All quantities on the right hand side of equation (28) are usually complex functions of current and pressure. Therefore, one expects a complicated equation U = U(P, I). However, equation (27) is surprisingly simple, which may not be generalized and extended to other arc conditions.

In the case of constant pressure, equation (27) reduces to the Ayrton equation (24). Since the anode fall as well as the cathode fall may be assumed to be independent of the current (25, 26), the falling characteristic (arc voltage decreases with increasing current) may be explained by the combined behavior of the electrical conductivity and conductance. In most cases the

electrical conductivity increases with increasing current. The arc cross section is also of importance because it determines the conductance of the arc.

The pressure has a strong and complex influence on the field strength (4, 27), as well as on anode and cathode fall (28). Since the mean free path of the electrons between the electrodes decreases with increasing pressure, there is an effect on the ionization and energy transfer processes in the arc. It was observed that the arc voltage decreases with increasing pressure in the high pressure range (25).

2. Arc voltages lower than the first excitation potential of argon (12.9 volts) are observed under some conditions. This low arc voltage has also been reported by Busz and Finkelnburg (29) and studied by Druyvesteyn and Penning (30). The latter found that in a neon arc, the plasma potential may assume a maximum value of 18.7 volts with respect to the cathode potential (the excitation energy of neon is 18.5 volts) in a bright region between the electrodes, while the voltage across the arc was only 12.3 volts.

3. The characteristic anode voltages are found to be independent of current, and are linearly dependent on the reciprocal of the pressure.

D. Longitudinally Segmented Anode (Configuration 2)

The longitudinally segmented anode is used for "local" energy transfer and current measurements. The word "local" should be understood here only in the sense that the anode is divided into eight segments. It should be noted that the anode arc attachment area is usually smaller than the area of a single

segment. Thus, the measured values are used only in establishing qualitative trends.

Due to its limited heat dissipation capacity, the longitudinally segmented anode is operated, using only argon as a working fluid, at relatively low currents ($I \leq 250$ amps) to prevent erosion of the segments.

The anode is made of eight segments with each segment connected electrically through a shunt to a common bus bar, so that individual current measurements can be made. Thermocouples are installed in the cooling water circuit to measure the temperature rise in the water for each segment.

1. Current and Heat Flux Distributions

Current and heat flux distributions under two different operating conditions are shown in Figures 19 and 20. The current is distributed to all segments of the anode but not in a homogeneous manner. This distribution can be changed by small adjustments of the cathode position. However, it seems to be impossible to obtain a stable, uniform current distribution by adjustment of the cathode position alone, since neither the cathode nor the anode orifice are perfectly round or perfectly concentric to each other. In addition, any tendency of the arc to attach at the anode in a more or less constricted manner immediately destroys the symmetry. Figure 21 shows the current and heat flux into one segment as a function of time. For the 100-amp case the current and the heat flux remain almost constant to each segment during the chosen time period. This indicates that the arc is operating in a stable manner. At 200 amps the arc does not show this same stability as both the current and the

heat flux varied with time, which indicated that the arc anode attachment has a tendency to move. Since there is no periodic variation in current, it appears that the arc attachment moves in some random fashion. In both cases the total current and arc voltage remain constant.

2. Verification of Anode Heat Transfer Model

For a verification of the proposed anode heat transfer model according to equation (15) it is desirable to choose conditions under which the current dependence of Q_{CR} and U_I can be eliminated. This can be easily accomplished by using the axially segmented anode (Configuration 2) and keeping the total arc current as well as the other arc parameters constant. The change of Q_{CR} with varying current distribution to the individual segments is probably negligible. The same argument holds for U_I because the electron temperature and the anode fall are understood as average values in case of a non-symmetric current distribution. Therefore, simultaneously taken data of segmental currents, I_s, plotted versus segmental heat fluxes, Q_s, should result in a straight line. The slope of the straight line yields the value of U_I and the intercept with the ordinate yields the average heat flux Q_{CR} per segment. One might argue that one set of measurements is not sufficient to prove the validity of the proposed anode heat transfer model because such a procedure comprises only one current and heat flux measurement per segment. The symmetry of the segmentation, however, allows a more extensive interpretation of the measurements. The 8 different data points of Figure 22 could also be obtained for a single segment by artificially varying the current to this segment in the same way as

prescribed by the 8 data points in Figure 22 in which each data point corresponds to a different segment. There is no reason why the corresponding heat fluxes should not be the same as found in Figure 22. Therefore, the data points of Figure 22 may actually be considered as 8x8 measurements. Within experimental accuracy the findings of Figure 22 represent a confirmation of the anode heat transfer model. The quantities included in Q_{CR} and U_I may further be subdivided according to equations (13) and (14), which requires measurements to find the electron temperature and the anode fall potential. The latter measurements are beyond the scope of this work.

The technique as described above is used in the following section for acquiring anode heat transfer data for different parameter settings.

3. Parametric Heat Balance Studies

For the following studies, the power input, heat flux into the anode and cathode are measured separately for different arc parameter settings. Furthermore, the heat fluxes into the anode are subdivided into two parts as mentioned in the previous section. The data are represented graphically according to equation (23), which represents a total energy balance in terms of a voltage balance. The corresponding energy fluxes may be obtained by multiplying the voltages in these graphs with the specified current.

In Figure 23 the quantities contained in equation (23) are plotted against the mass flow rate, $\dot{m}$, at I = 100 amps, and P = 20 mmHg. The curve at the top of the drawing is the total arc voltage; all the other quantities are explained in connection

with equation (23). From Figure 23 (also see Table 2), the following results are observed for an increasing mass flow rate:

(a) The total arc voltage, U, increases as previously described in section V.B.

(b) U_I decreases; U_{CR} increases first and then decreases, while the characteristic anode voltage, $U_A = U_I + U_{CR}$ decreases.

(c) There is a slight decreasing tendency of the characteristic cathode voltage.

(d) The available voltage, U_{AV} increases.

From equation (28), it follows that the total arc voltage is the sum of anode fall, cathode fall and electrical field strength integrated over the length of the arc column. Both anode and cathode fall are probably not strongly influenced by the mass flow rate, because the thickness of the sheath in front of the electrodes is normally only of the order of several mean free path lengths, which is much thinner than the boundary layer thickness. Therefore, the conditions within the sheath should be effectively protected from the flow field by the boundary layer. However, there may be some secondary effects on the electrode falls, such as property changes in the arc column, changes of the upstream pressure, etc. The electrical field strength as well as the length of the arc column will increase with increasing mass flow rate. The former is caused by greater energy exchange between plasma column and gas flow, while the latter is due to arcflow interactions (11).

According to equation (14) there are three quantities which can influence the value of U_I, namely the electron temperature,

T_e, the anode fall, U_a, and the work function of the anode material, ϕ_a. Since ϕ_a does not vary with mass flow rate (for copper $\phi_a \approx$ 4V (31)), the electron temperature and/or the anode fall would have to decrease with increasing mass flow rate. By means of a simple analytical model, Sherman and Yeh (32) have shown that the electron temperature decreases with increasing mass flow rate, which would be consistent with the results of this study. The effects of the mass flow rate on the anode fall are still unknown, although in the previous paragraph it is argued that it will not be strongly affected. A final answer to this question requires separate measurements of electron temperature and anode fall.

U_{CR}, as defined by equations (13) and (22), includes the radiative and convective part of the anode heat transfer. A calculation for an estimate of radiative and convective anode heat fluxes based on the experimental data will be presented in section V.D.6 and 7 respectively.

The characteristic anode voltage, U_A, which is the sum of U_I and U_{CR}, varies for the conditions shown in Figure 23 from about 10 to 20 volts, which is comparable to some other investigations which have recently been reported (33, 34). Figure 24 taken with a current of 200 amps, shows a peculiar maximum of U_I at lower mass flow rates, which coincides with a sudden jump of the arc voltage.

In Figure 25, data are shown taken in the low pressure range ($P \leq 1$ mmHg). The chamber pressures are now a function of the mass flow rate as indicated in Table 2. The general trend of the quantities U_{AV}, U_I, U_{CR}, and U_C is the same as before. The arc

voltage, however, is independent of mass flow rate. At a mass flow rate $\dot{m} \leq 0.07$ g/sec the arc becomes unstable and extinguishes with the chosen parameters. The similarity of the results in Figure 24 beyond 0.07 g/sec flow rate and Figure 25 suggests that a similar arc condition prevailed in spite of the different test chamber pressures. Measurements of the pressures upstream of the anode orifice show that the back pressures are about the same in both cases (35 - 50 mmHg depending on mass flow rate). Since the majority of the current attaches to the anode close to the orifice (35), the arc is in both cases operated in the same pressure environment, so that arc voltage and electrode heat transfer are governed by the back pressure rather than the test chamber pressure.

4. Magnetic Field Effects

The magnetic fields have a very strong effect on the shape of the plasma plume. In the medium pressure range the long plasma plume is shortened and widened by the action of a magnetic field. Sometimes the plume is deflected to one side. At low pressures the blue core in front of the cathode is stretched and extends farther downstream.

For the geometry and parameters used in this experiment, the current and anode heat flux distributions as shown in Figures 19 and 20 do not change their pattern of asymmetry with an applied magnetic field strength up to 2,000 gauss, and no evidence of a rotating current spoke can be observed under those conditions. Actually, such a rotation should occur, due to the action of $\bar{j} \times \bar{B}$ forces, as soon as a constricted arc attachment is observed. Larson (36) and Lovberg (37) showed experimental evidence of

rotating current spokes. The reason that these rotating current spokes did not appear in our experiments must be connected with significant differences in the arc parameters. By decreasing the flow rate of the injected argon below 0.04 g/sec and increasing the diameter of the anode orifice from 1.27 cm to 1.91 cm a rotating current spoke can be clearly detected using Rogowski coils for the measurements. The change of the anode geometry and of the flow rate result both in a reduced gas velocity in the annular gap between cathode and anode. Higher gas velocities probably blow the arc farther downstream where the $\bar{j} \times \bar{B}$ interaction is much weaker. Therefore, the arc does not rotate under these conditions. No quantitative measurements related to this effect have been undertaken. Qualitative observations may be summarized as follows:

1. The rotation frequency of the current spoke is strongly influenced by the gas velocity. The frequency increases with decreasing gas velocity.
2. There is no continuous transition from the rotating to the non-rotating mode. At certain parameter settings, the arc may indeed shift back and forth between these two modes.
3. The rotation frequency increases with increasing arc current and/or magnetic field strength as anticipated.

Figures 26 and 27 show the effects of the magnetic field strength on quantities contained in equation (23). The arc voltage increases with increasing magnetic field strength. Patrick and Schneiderman (38) have derived a simple linear relationship between the arc voltage and the superimposed magnetic field

strength in an MPD arc. The data of this work support their theory in the low pressure range (Figure 27), but in the medium pressure range (Figure 26) deviations from the linear relationship occur. The characteristic cathode voltage, U_C, remains almost constant, while the characteristic anode voltage increases slightly with increasing magnetic field strength. The small increase of U_{CR} with increasing magnetic field strength may be caused by a somewhat higher convective heat transfer (see section V.D.6). The effect of the magnetic field on U_I is rather small. At this time no conclusion can be drawn with regard to the individual changes of T_e and U_a. McBee and Dow (39) have studied the electrode regimes of a glow discharge in the presence of a transverse magnetic field. They found that with increasing magnetic field strength, the anode fall and the positive column gradient increases while the cathode fall first decreases and then becomes constant. The combination of both yields a minimum in the total discharge potential. To the author's knowledge, there are no data available which describe the effect of a magnetic field on the electrode regimes in an MPD arc configuration.

From Figures 26 and 27 it follows that the magnetic field has a favorable influence on the thermal efficiency, because the slope of the arc voltage versus the magnetic field strength is larger than the slope of the characteristic anode voltage. A more detailed discussion of the thermal efficiencies follows in section V.D.7.

5. Cathode Heat Balance

With the present experimental arrangement, a parametric study of the cathode heat balance is rather difficult. In ad-

dition to the complex heat transfer mechanisms which are involved (see section III.C), the unfavorable cathode geometry (Figure 2) further complicates the interpretation of experimental data. The configuration is unfavorable because between the heat input at the cathode tip and the water-cooled cathode base a large amount of heat is transferred to the anode by radiation and some by convective heat transfer. This effect becomes obvious when the cathode diameter is changed from 0.63 cm to 0.95 cm, and the distance between the cooling water base and the cathode tip is shortened from 8 cm to 2.5 cm. Although the overall arc conditions remain essentially the same, the measured cathode heat fluxes increase by an order of magnitude (compare values listed in Tables 1 and 2).

For a detailed cathode heat balance the knowledge of the cathode fall potential, of the ion temperature and of the accommodation coefficient is required. In addition, the cathode temperature distribution has to be known in order to estimate radiation and convection losses. In this work no attempt has been made for such measurements, hence only some qualitative conclusions can be drawn from the calorimetric cathode heat transfer data listed in Table 2.

(a) The characteristic cathode voltage decreases slightly with increasing chamber pressures and/or mass flow rate. Apparently, this is caused by increasing convective heat losses to the gas.

(b) The characteristic cathode voltage decreases with increasing arc current, while the heat flux to the cathode coolant increases with increasing arc current.

(c) The characteristic cathode voltage decreases slightly with increasing magnetic field strength. At this time no conclusive explanation can be given for this finding. One may speculate that the cathode fall potential decreases with increasing magnetic field strength if a comparison with the glow discharge (39) is permissible.

A simple one-dimensional heat transfer model is used to calculate the radiation heat flux emitted from the cathode surface. In this calculation convection is neglected. The equation which describes combined heat transfer by conduction and radiation (see Figure 28) may be written as

$$\frac{d^2T}{dx^2} = \frac{2\varepsilon\sigma}{\kappa r}\,(T^4 - T_\infty^4) \tag{29}$$

where T_∞ is the temperature of the surroundings. The radiation heat flux emitted by the cylindrical cathode is

$$Q_R = 2\pi r\varepsilon\sigma \int_0^L T(x)^4 dx \tag{30}$$

The conduction heat flow through the water cooled end is

$$Q_C = \pi\kappa r^2 \left.\frac{dT}{dx}\right)_{x=L} \tag{31}$$

Numerical solution of equations (29) to (31) are obtained with a high speed computer specifying the following selected boundary conditions:

(a) $T_1 = 3000$ K, $\qquad Q_C = 0$

(b) T_1 = 3000 K, Q_C = 0.3 kW

(c) T_1 = 3000 K, Q_C = 0.5 kW

(d) T_1 = 3000 K, T_2 = 300 K

T_1 = 3000 K is selected to be below the melting point of tungsten. Q_C = 0 and T_2 = 300 K (water temperature) are two limiting cases. Q_C = 0.3 and 0.5 kW are chosen because most experimental data are between these values (Table 2).

The constants used for this calculation are

ε = 0.4 (40)

$\sigma = 5.61 \times 10^{-15}$ kW/cm^{2}K^4

$\kappa = 1.1 \times 10^{-3}$ kW/cm-K (40)

r = 0.476 cm

L = 2.54 cm

T_∞ = 300 K

Figure 28 shows the temperature profiles obtained for the different boundary conditions, while the heat transfer results are summarized in Table 3. The calculated radiation emitted from the cathode is in the same order of magnitude as the measured Q_{CR} values (Table 2, $O_{CR} = IU_{CR}$). The accuracy of the calculations is limited because (a) higher cathode tip temperatures prevail at higher currents, (b) heat losses by convection to the gas are not included, (c) a certain portion of the emitted radiation by the cathode is reflected by the anode.

6. Convective Anode Heat Transfer

In this section convective anode heat transfer is calculated according to section III.B.1. Unfortunately, in the experimental part of this work the contribution to the anode heat transfer by

convection cannot be separated from the other heat transfer mechanisms. Therefore, a direct comparison between calculations and experimental data is not possible.

The calculations of convective anode heat transfer contain a large uncertainty which is due to the following:

(a) The effective area for heat transfer is unknown because the anode arc attachment area cannot be measured in this experiment. In this calculation an area of 2 cm^2 is used, which corresponds to a length of 0.5 cm at the 1.27 cm diameter anode nozzle throat. This assumed value is partially justified by some experimental evidence (35).

(b) There is a large pressure drop across the plasma column, especially at low chamber pressures and high mass flow rates. It is questionable which reference pressure should be used for the property values needed for the convective heat transfer calculations.

(c) The transport properties of argon plasmas at low pressures are not available in the literature. Hence, all property values based on 1 atm. pressure are used in this calculation (42, 43). This gives probably higher heat transfer coefficients than the actual values at lower pressures.

(d) It is pointed out in section III.B.1 that a necessary condition for the validity of equations (6) and (7) is that the Lewis number does not differ very much from unity. This cannot be checked without knowing the proper values. Nevertheless, these calculations should establish the correct order of magnitude of the contribution of convective heat transfer to the observed total anode heat fluxes. Also, the trend of convective

heat transfer as a function of the arc parameters becomes apparent from the calculated values.

The general form of the heat transfer relationship as expressed by equation (7) assumes the following specific form for laminar flow through a tube with constant wall temperature (41)

$$Nu = 3.65 \qquad (35)$$

According to reference (15) the properties appearing in equation (32) have to be inserted at an average enthalpy between the bulk gas enthalpy and the gas enthalpy corresponding to the anode surface temperature. The bulk gas enthalpy is calculated from experimental data using the equation

$$i_s = IU_{AV}/\dot{m} \qquad (33)$$

The surface temperature of the copper anode is assumed to be 1000 K, according to reference (42); this corresponds to an enthalpy i_w = 520 kJ/kg.

Results of convective anode heat transfer calculations are collected in Table 2, from which the following conclusions may be drawn:

(a) The calculated U_{Conv} is less than U_{CR}, and seems to be in the right order of magnitude.

(b) U_{Conv} decreases with increasing mass flow rate, which is the same trend as displayed by U_{CR}.

(c) U_{Conv} decreases with increasing arc current, which is equivalent to an increased radiative heat transfer

from the cathode to the anode at higher arc currents.

(d) U_{Conv} shows a maximum between 10 and 20 mmHg as the pressure increases from 0.15 to 40 mmHg. This finding has to be verified by more experimental data.

(e) U_{Conv} increases with increasing magnetic field strength, which is the same trend as displayed by U_{CR}.

7. Thermal Efficiency

The thermal efficiencies, η, are computed using experimental data from section III.D. Results are shown in Figures 23 to 27 and listed in Table 2 from which the following conclusions may be drawn:

(a) η increases with increasing mass flow rate, and the thermal efficiencies are very low at small mass flow rates. The latter is one of the reasons for the low overall efficiencies of the present MPD-arc devices.

(b) η increases with increasing chamber pressure.

(c) η increases with increasing arc current.

(d) η increases with increasing magnetic field strength.

E. Axially Segmented Anode

The axially segmented anode is used for axial heat transfer and current distribution measurements. The parameters which are especially interesting for this study are mass flow rate, magnetic field strength and cathode position.

Figures 29 and 30 show the effect of an increasing mass flow rate on the current and heat flux distributions. At zero mass flow rate the arc terminus is more diffuse, with the current attachment mainly on segment 2, spreading partially to segment 3.

As the mass flow rate increases, the current attachment becomes more constricted and the current-carrying column is blown further downstream, attaching primarily on segment 3. Also, it can be seen that the heat flux distribution follows the current pattern. The ability of the increasing mass flow rate to blow the arc attachment further downstream is in agreement with the findings of earlier work in this laboratory although a different arc configuration has been used (3).

The effect of the magnetic field on the current distribution for different mass flow rates is shown in Figures 31 and 32. Each plot shows the current distribution as a function of the magnetic field strength. In general, the increasing magnetic field pushes the current attachment from segment 2 to segment 3. At a pressure of 20 mmHg and small gas flow rates, the magnetic field causes no significant change in the current distribution.

Included in Figures 31 and 32 is the heat flux distribution as a function of the magnetic field at different mass flow rates. These distributions follow the same general trends established by the current distribution, showing that the dominating contribution to the heat flux stems from the current. The radiation and convection contribution to the heat flux does not disturb the established trends, but does, in some cases, shift the curves so that they do not appear in the same sequence as do the curves for the current distributions. Segment 2 always receives more radiation from the cathode than segment 3, so that at 20 mmHg operating pressure, where the two segments draw approximately the same current, the order established by the current distribution is reversed in the heat flux distribution.

The effect of cathode location on the current distribution for several different mass flow rates is shown in Figures 33 and 34. Each figure shows the change in the current distribution as the cathode is moved in axial direction up- or downstream from its center position at which the cathode tip is flush with the plane at the beginning of the diverging portion of the anode. In each case the tank pressure and mass flow rate are kept constant and no magnetic field is applied, which should mean that the current-carrying path of the arc retains its shape. This is shown by the fact that a greater percentage of the current flows to the outer segments of the anode as the cathode moved downstream and to the inner segments of the anode as the cathode moves upstream. Figures 33 and 34 also show the corresponding energy flux distribution. These curves follow the same trends established by the current distribution.

The overall energy flux to the anode, Q_A, is shown in Figure 35 as a function of cathode position for different mass flow rates. In each case the overall energy flux to the anode decreases slightly as the cathode moves downstream. Because of the scatter of the data no trends can be established as the cathode moves upstream from the center position. The arc voltage, U, shown in Figure 36, shows basically the same trend as Q_A. It was pointed out by Schneiderman and Patrick (20) that the arc voltage was affected by the cathode position. With the observed data from the axially segmented anode it is possible to speculate on these trends.

As the cathode tip is moved upstream, the tip moves into the cylindrical portion of the anode. The current-carrying path

is now exposed to a more intense gas flow, resulting in a more constricted arc column which, in turn, requires a higher field intensity. Cathode and anode fall may also somewhat increase. Therefore, a higher overall arc voltage is required to maintain a constant arc current. A higher field intensity in the arc may cause a higher electron temperature which would contribute to the increase in Q_A as the cathode tip is moved upstream. A larger anode fall would have the same effect. As the cathode tip moves downstream from the center position, the tip moves into the diverging portion of the anode, which allows for a reduction in the constriction of the arc and a resulting lower arc voltage.

F. Experiments in Ammonia

A few experiments have been performed with the solid anode using ammonia as the working fluid at low pressures with and without superimposed magnetic field. The arc is struck in an argon atmosphere and then gradually changed to ammonia. The plasma plume shows a very pronounced red core (H_α) and a greenish-yellow tail. Figure 37 (see also Table 4) shows the relation between the characteristic anode voltage and the arc voltage. The data are compared with those reported by Schneiderman and Patrick (20), and are found to be somewhat below the range of values which they reported. Neglecting cathode losses the characteristic anode voltage, U_A, is identical with their V_o'. The discrepancy in the comparison may be caused by the smaller gas flow rates (0.01 - 0.05 g/sec) used in their experiments.

The data plotted in Figure 37 refer to two different diverging angles of the anode orifice (30 and 40 degrees). The over-

all arc characteristics as well as the anode heat transfer are not affected by this angle. The arc seems, however, to be more stable for an angle of θ = 40 degrees.

Figure 38 (see also Table 4) shows the effects of the magnetic field on the arc voltage and characteristic anode voltage. Basically, the results are similar to those obtained from the experiments in argon atmosphere.

VI. SUMMARY

For the study of the basic physical processes involved in arc-gas-electrode heat transfer phenomena with and without the influence of a magnetic field, the existing arc tunnel was modified. An anode energy transfer model was proposed and verified by experimental data. Three different anode configurations were studied, namely, a solid cylindrical anode, a longitudinally segmented anode and an axially segmented anode. Argon and ammonia were used as working fluids over a certain range of arc current, mass flow rates, chamber pressures, cathode positions and magnetic field strengths. In order to study the influence of the important parameters on the anode energy transfer, a large number of overall and local energy balance measurements were performed. The results of the experimental program is summarized in the following list:

1. During arc operation three different flow regimes have been observed; a laminar, a transitional, and a turbulent regime. The arc voltage as well as the characteristic anode voltages are strongly influenced by the

different regimes.

2. The characteristic anode voltage is independent of the current.
3. At zero mass flow rate, a linear relationship between the arc voltage and the reciprocal of the pressure and the arc current is found.
4. Circumferential current and heat flux distributions on on the anode surface are not uniform.
5. A confirmation of the proposed anode heat transfer model is obtained from experimental data using a longitudinally segmented anode. Plots of Q_S versus I_S result in a straight line allowing the determination of U_I and Q_{CR}.
6. The arc voltage increases with increasing magnetic field strength.
7. The characteristic anode voltage increases with magnetic field strength but not as much as the arc voltage does.
8. The axial current distribution is affected by mass flow rate and magnetic field strength. The anode current attachment moves downstream with increasing mass flow rate and/or magnetic field strength.
9. The axial current distribution as well as the arc voltage and the anode heat flux are affected by the cathode tip position.
10. Anode heat transfer data taken with ammonia as working fluid are similar to those in argon.

REFERENCES

1. S.A. Wutzke, C.J. Cremers and E.R.G. Eckert, "The Thermal Analysis of Anode and Cathode Regimes in an Electric Arc Column," HTL TR No. 56, University of Minnesota (1963).

2. E. Pfender, S.A. Wutzke and E.R.G. Eckert, "An Arc Tunnel Facility for the Thermal Analysis of Anode and Cathode Regimes in an Electric Arc Column," NASA CR 54080, University of Minnesota (1964).

3. E. Pfender, S.A. Wutzke, K.T. Shih, T. Eddy and E.R.G. Eckert, "Thermal Analysis and Study of Arc-Flow Interactions in the Anode Regime of an Electric Arc," NASA CR 54465, University of Minnesota (1965).

4. W. Finkelnburg and H. Maecker, "Electric Arcs and Thermal Plasma," Handbuch der Physik Vol. XXII, Springer-Verlag, Berlin (1956).

5. J.M. Somerville, The Electric Arc, Methuen, London (1959).

6. A. von Engel, Ionized Gases, 2nd Edition, Oxford, London (1965).

7. K.H. Hoecker and W. Bez, "Theorie des Anodenfalls," Z. Naturforsch., 91, 72 (1954).

8. G. Ecker, "Electrode Components of the Arc Discharge," Ergebn. d. exakt. Naturw. 33, Springer-Verlag, Berlin (1961).

9. N.M. Nerheim and A.J. Kelly, "A Critical Review of the State-of-the-Art of the MPD Thrustor," AIAA Paper No. 67-688, AIAA Electric Propulsion and Plasmadynamic Conference, Colorado Springs, Colorado (1967).

10. R.R. John, S. Bennett and J.F. Connors, "Experimental Performance of a High Specific Impulse Arc Jet Engine," AIAA Paper No. 64-669, AIAA Fourth Electric Propulsion Conference, Philadelphia, Pennsylvania (1964).

11. T.W. Myers and W.C. Roman, "Survey of Investigations of Electric Arc Interactions with Magnetic and Aerodynamic Fields," ARL Report, ARL 66-0184 (1966).

12. P.A. Schoeck, "An Investigation of the Energy Transfer to the Anode of High Intensity Arc in Argon," Ph.D. Thesis, University of Minnesota (1961).

13. E. Pfender, G.D. Raithby and E.R.G. Eckert, "An Anode Comparison Study in a Wall-Stabilized Argon Arc," ARL Report, ARL 65-2321 (1965).

14. E.R.G. Eckert and E. Pfender, "Advances in Plasma Heat Transfer," Advances in Heat Transfer, Vol. 4, Academic Press, New York (1967).

15. E.R.G. Eckert, "Survey on Heat Transfer at High Speeds," WACD Tech. Report 54-70 (1954).

16. H.E. Petschek, P.H. Rose, H.S. Glicke, A. Kane and A. Kantrowitz, "Spectroscopic Studies of Highly Ionized Argon Produced by Shock Waves," J. Apply. Phys 26, 83 (1955).

17. H. Hügel, G. Kruelle and Th. Peters, "Investigation of Plasma Thrustors with Self-magnetic Acceleration," AIAA Paper No. 66-237, AIAA Fifth Electric Propulsion Conference, San Diego, California (1966).

18. R.C. Eberhart, "The Energy Balance for the High Current Argon Arc," Ph.D. Thesis, University of California, (1965).

19. A. Bauer, "Untersuchungen über den Kathodenfallin den Übergangsbereichen vom Thermobogen zum Feldbogen und vom Bogen zur Glimmentladung," Ann. Phys. 18, 387 (1956).

20. A.M. Schneiderman and R.M. Patrick "Optimization of the Thermal Efficiency of the Magnetic Annular Arc," AIAA Paper No. 66-115, AIAA Third Aerospace Science Meeting, New York (1966).

21. S.A. Wutzke, E. Pfender and E.R.G. Eckert, "Study of Electric-Arc Behavior with Superimposed Flow," AIAA J. 5, 707 (1967).

22. P.W. Runstadler, Jr., "The Laminar and Turbulent Flow of an Argon Arc Plasma," AIAA Paper No. 66-189, AIAA Plasmadynamics Conference, Monterrey, California (1966).

23. F.P. Incropera, "Temperature Measurement and Internal Flow Heat Transfer Analysis for Partially Ionized Argon," TR No. SU 247-11, Stanford University (1966).

24. H. Ayrton, The Electric Arc, Van Nostrand, New York (1902).

25. G. Busz-Peuckert and W. Finkelnburg, "Zum Anodenmechanismus des Thermischen Argonbogens," Z. Phys. 144, 244 (1956).

26. W. Finkelnburg, "Versuche zum Mechanismus von Hochtemperatur-Lichtbögen Niedriger Brennspannung," Apply. Sec, Res. 5B, 201 (1955).

27. R. Rompe and W. Thouret, "Die Leuchtdichte der Quecksilberhochdruckentladung bei hohen Drucken," Z. Techn. Phys, 17, 377 (1936).

28. P. Schoeck and F. Maisenhälder, "Zur Druckabhängigkeit der Anodenfallspannung von Hochdrucklichtbögen," Beiträge aus der Plasmaphysik, 5, 345 (1966).

29. G. Busz-Peuckert and W. Finkelnburg, "Thermischer Lichtbogen hoher Temperatur," Z. Physik 139, 212 (1954).

30. M.J. Druyvesteyn and F.M. Penning, "The Mechanism of Electrical Discharge in Gases of Low Pressure," Rev. Mod. Phys., 12, 87 (1940).

31. A. von Engel and M. Steenbeck, Elektrische Gasentladungen, Springer-Verlag, Berlin (1932).

32. A. Sherman and H. Yeh, "Blowing of Current Patterns in Nonequilibrium Plasmas," AIAA Journal 5, 1689 (1967).

33. J.A. Fay and W.T. Hogan, "Heat Transfer to Cold Electrodes in a Flowing Ionized Gas," Physics Fluid 5, 885 (1962).

34. P.D. Lenn, J.R. Bodoia, D.L. Ward, G.L. Hamilton and S.T. Demetriades, "Three-Fluid Nonequilibrium Plasma Accelerators, Part II," AIAA Electric Propulsion Conference, Colorado Springs, Colorado (1963).

35. W.E. Powers, "Measurements of the Current Distribution in the Exhaust of an MPD Arcjet," AIAA Journal 5, 545 (1967).

36. A.V. Larson, "Experiments on Current Rotations in an MPD Engine," AIAA Paper No. 67-689, AIAA Electric Propulsion and Plasmadynamics Conference, Colorado Springs, Colorado, (1967).

37. C. Ekdahl, R. Kribel and R. Lovberg, "Internal Measurements of Plasma Rotation in an MPD Arc," AIAA Paper No. 67-655, AIAA Electric Propulsion and Plasmadynamics Conference, Colorado Springs, Colorado (1967).

38. R.M Patrick and A.M. Schneiderman, "Performance Characteristics of a Magnetic Annular Arc," Sixth Symposium on Engineering Aspects of Magnetohydrodynamics, P. 70 (1965).

39. W.D. McBee and W.G. Dow, "The Influence of a Transverse Magnetic Field on an Unconfined Glow Discharge," AIEE Transactions 72 Part I, 229 (1953).

40. Handbook of Thermophysical Properties of Solid Materials, Vol 1, Pergamon Press, New York (1961).

41. E.R.G. Eckert and R.M. Drake Jr., Heat and Mass Transfer, McGraw-Hill, New York (1959).

42. K.S. Drellishak, C.F. Knopp and A.B. Cambel, "Partition Functions and Thermodynamic Properties of Argon Plasma," Arnold Engineering Development Center AEDC-TDR-63-146 (1963).

43. R.S. Devoto, "Transport Coefficients of Partially Ionized Argon," Physics of Fluid 10, 370 (1967).

TABLE 1 HEAT BALANCE*

Run No	P (mmHg)	$\dot{m}$ (g/sec)	I (amps)	U (volts)	UI (kW)	Q_A (kW)	Q_C (kW)	Q_G (kW)	Q_T (kW)	$\frac{Q_T-UI}{UI}$ (%)
1	40	0.55	500	14.8	7.40	4.06	0.194	3.38	7.63	3.1
2	40	0.90	500	22.0	11.0	4.44	0.196	6.32	10.96	-0.4
3	40	1.40	500	23.5	11.75	4.47	0.196	6.96	11.63	1.0
4	40	1.05	300	26.0	7.80	3.04	0.121	4.98	8.14	4.4
5	40	1.05	295	26.0	7.67	2.94	0.119	4.89	7.95	3.6
6	40	1.55	300	27.0	8.10	2.98	0.119	5.19	8.29	2.3
7	40	1.95	300	27.2	8.16	2.95	0.116	5.46	8.53	4.5
8	40	2.65	300	27.5	8.25	2.84	0.114	5.60	8.56	3.8
9	20	0.28	200	18.0	3.60	1.80	0.111	1.65	3.56	-1.1
10	20	0.58	200	21.0	4.20	2.15	0.113	1.92	4.18	-0.5
11	20	0.58	200	21.3	4.26	2.06	0.141	2.12	4.32	1.4
12	20	0.74	200	21.5	4.30	2.02	0.109	2.15	4.27	-0.7
13	20	1.58	200	29.0	5.80	1.98	0.095	3.94	6.02	3.8
14	20	2.15	200	30.9	6.18	1.85	0.095	4.12	6.07	-1.8
15	20	2.90	200	31.8	6.36	1.87	0.089	4.43	6.39	0.5

TABLE 1 continued

Run No	P (mmHg)	$\dot{m}$ (g/sec)	I (amps)	U (volts)	UI (kW)	Q_A (kW)	Q_C (kW)	Q_G (kW)	Q_T (kW)	$\frac{Q_T - UI}{UI}$ (%)
16	20	0.44	100	30.0	3.00	0.85	0.071	1.93	2.85	-5.0
17	20	0.67	100	40.3	4.03	0.91	0.068	3.15	4.13	2.5
18	20	1.00	100	42.0	4.20	1.01	0.058	3.23	4.25	1.2
19	100	0.94	100	21.8	2.18	0.86	0.066	1.32	2.24	2.8
20	100	1.95	100	23.0	2.30	0.84	0.061	1.53	2.41	4.8
21	100	2.95	100	24.5	2.45	0.79	0.054	1.64	2.47	0.4
22	100	4.40	100	27.0	2.70	0.75	0.047	1.86	2.63	-2.6
23	100	5.55	100	29.3	2.93	0.70	0.047	2.17	2.89	-1.4
24	40	0.50	100	21.5	2.15	1.02	0.079	1.15	2.25	4.6
25	40	0.50	100	22.0	2.20	0.99	0.080	1.18	2.26	2.7
26	40	1.10	100	24.0	2.40	0.96	0.076	1.42	2.46	2.5
27	40	2.20	100	25.0	2.50	0.90	0.071	1.65	2.62	4.8
28	40	2.65	100	26.0	2.60	0.89	0.071	1.73	2.69	3.4
29	40	0.00	200	10.6	2.12	2.02	0.103	0.04	2.14	1.0
30	40	0.55	200	17.3	3.46	1.60	0.090	1.94	3.63	4.9

TABLE 1 continued

Run No	P (mmHg)	$\dot{m}$ (g/sec)	I (amps)	U (volts)	UI (kW)	Q_A (kW)	Q_C (kW)	Q_G (kW)	Q_T (kW)	$\frac{Q_T - UI}{UI}$ (%)
31	40	0.86	200	21.0	42.0	1.74	0.089	2.32	4.16	-1.0
32	40	0.90	200	21.5	4.30	1.69	0.092	2.62	4.41	2.5
33	40	2.25	200	22.0	4.40	1.69	0.094	2.76	4.54	3.2
34	40	4.00	200	30.5	6.10	1.74	0.084	4.20	6.02	-1.3
35	40	1.40	200	31.5	6.30	2.14	0.090	4.09	6.32	0.3
36	40	2.30	200	33.2	6.64	2.07	0.084	4.63	6.78	2.1
37	40	3.80	200	37.2	7.24	1.96	0.087	5.54	7.57	4.5
38	40	3.80	200	34.5	6.90	1.91	0.087	4.94	6.93	0.4
39	40	3.80	200	37.0	7.20	1.94	0.087	5.25	7.27	1.0
40	40	3.80	200	37.2	7.24	1.98	0.084	5.47	7.53	4.0
41	40	1.20	200	28.6	5.72	1.99	0.094	3.82	5.90	3.1
42	40	0.84	200	28.5	5.70	2.15	0.099	3.48	5.73	5.3

* 0.63 cm cathode diameter is used for these data, Configuration 1, B = 0.

TABLE 2 HEAT BALANCE FOR LONGITUDINALLY SEGMENTED ANODE**

Run No	P (mmHg)	$\dot{m}$ (g/sec)	I (amps)	B (gauss)	U (volts)	U_A (volts)	U_I (volts)	U_{CR} (volts)	U_{Conv} (volts)	U_C (volts)	η (%)
101	20	0	100	0	25.0	20.8	16.0	4.8	----	3.42	3.2
102	20	0.029	100	0	25.6	17.2	11.5	5.7	2.52	3.28	19.9
103	20	0.072	100	0	30.0	14.3	9.5	4.8	2.43	3.25	41.7
104	20	0.116	100	0	32.5	12.1	8.4	3.7	2.35	3.20	52.9
105	20	0.170	100	0	33.5	11.6	8.2	3.4	2.35	3.27	55.5
106	20	0.218	100	0	36.0	11.0	8.0	3.0	2.18	3.34	60.3
107	20	0.355	100	0	37.5	10.5	7.6	2.9	1.68	3.37	62.9
108	40	0	100	0	17.0	13.0	11.5	1.5	----	3.41	3.5
109	40	0.072	100	0	24.0	11.4	9.0	2.4	2.60	3.12	39.6
110	40	0.116	100	0	27.0	11.2	8.2	3.0	2.52	3.01	47.4
111	40	0.170	100	0	29.1	11.1	8.1	3.0	2.35	3.01	51.5
112	40	0.218	100	0	31.8	10.7	8.0	2.7	2.26	3.06	56.6
113	40	0.252	100	0	33.7	10.7	8.0	2.7	2.10	3.06	59.0
114	40	0.355	100	0	36.0	10.9	8.0	2.9	1.68	3.04	61.4
115	20	0	200	0	20.5	17.2	14.7	2.5	----	2.13	5.8

TABLE 2 continued

Run No	P (mmHg)	$\dot{m}$ (g/sec)	I (amps)	B (gauss)	U (volts)	U_A (volts)	U_I (volts)	U_{CR} (volts)	U_{Conv} (volts)	U_C (volts)	η (%)
116	20	0.029	200	0	34.8	23.5	16.0	7.5	1.60	2.12	26.4
117	20	0.072	200	0	34.7	18.8	12.0	6.8	1.18	2.18	39.5
118	20	0.116	200	0	34.7	15.3	10.0	5.3	1.13	2.16	49.6
119	20	0.170	200	0	35.4	12.9	8.5	4.4	1.13	2.14	57.6
120	20	0.218	200	0	35.9	11.5	8.0	3.5	1.09	2.10	62.1
121	20	0.355	200	0	37.0	10.5	7.5	3.0	0.67	2.02	66.2
122	30	0	200	0	16.8	13.9	10.8	3.1	----	1.96	5.3
123	30	0.029	200	0	29.5	20.1	14.0	6.1	1.38	2.05	25.1
124	30	0.072	200	0	32.4	17.4	12.7	4.7	1.26	2.02	40.1
125	30	0.116	200	0	34.0	15.1	10.5	4.6	1.09	2.00	49.7
126	30	0.170	200	0	35.0	13.5	8.5	5.8	1.18	2.00	55.7
127	30	0.218	200	0	36.0	12.5	7.5	5.0	1.26	1.93	59.7
128	30	0.355	200	0	37.5	11.4	7.5	3.9	0.93	1.92	64.3
129	0.27	0.072	200	0	34.0	18.4	14.2	4.2	1.30	2.54	38.5
130	0.35	0.116	200	0	34.5	14.6	11.5	3.1	1.26	2.41	50.7

TABLE 2 continued

Run No	P (mmHg)	$\dot{m}$ (g/sec)	I (amps)	B (gauss)	U (volts)	U_A (volts)	U_I (volts)	U_{CR} (volts)	U_{Conv} (volts)	U_C (volts)	η (%)
131	0.40	0.170	200	0	34.5	12.3	9.5	2.8	1.30	2.35	57.3
132	0.45	0.218	200	0	34.5	11.1	8.5	2.6	1.26	2.33	61.2
133	0.50	0.252	200	0	34.4	10.5	7.7	2.8	1.22	2.29	62.8
134	0.62	0.355	200	0	34.9	10.0	7.6	2.4	0.80	2.21	65.0
135	30	0.218	75	0	26.5	9.8	7.5	2.3	1.12	4.14	47.5
136	30	0.218	100	0	24.4	9.7	7.3	2.4	1.09	3.17	47.1
137	30	0.218	150	0	21.6	9.3	7.2	2.1	1.18	2.19	46.8
138	30	0.218	200	0	20.0	9.0	7.2	1.8	1.22	1.76	46.0
139	30	0.218	250	0	19.7	9.2	7.0	2.2	1.08	1.47	45.7
140	0.15	0.116	100	0	26.0	14.5	9.8	4.7	1.60	3.88	29.2
141	5	0.116	100	0	25.8	14.4	10.0	4.4	1.60	3.80	29.4
142	10	0.116	100	0	25.3	13.2	9.0	4.2	2.02	3.55	33.5
143	20	0.116	100	0	23.4	11.6	8.4	3.2	2.02	3.28	36.3
144	30	0.116	100	0	21.8	10.7	7.8	2.9	1.68	3.26	35.8
145	40	0.116	100	0	20.3	9.7	7.7	2.0	1.51	3.28	36.0

TABLE 2 continued

Run No	P (mmHg)	$\dot{m}$ (g/sec)	I (amps)	B (gauss)	U (volts)	U_A (volts)	U_I (volts)	U_{CR} (volts)	U_{Conv} (volts)	U_C (volts)	η (%)
146	30	0.86	100	0	35.5	12.5	7.4	5.1	0.29	3.06	56.0
147	30	0.86	100	350	37.5	12.2	7.4	4.8	0.35	3.05	59.5
148	30	0.86	100	700	39.2	12.5	7.4	5.1	0.38	2.98	60.4
149	30	0.86	100	1050	43.5	13.7	9.4	4.3	0.46	2.90	61.8
150	30	0.86	100	1400	45.0	13.9	10.0	3.9	0.50	2.79	62.8
151	30	0.86	100	1750	45.5	13.8	10.0	3.8	0.51	2.70	63.7
152	30	0.86	100	2000	46.5	14.1	10.2	3.9	0.54	2.60	64.1
153	30	1.1	100	0	30.3	10.3	7.2	3.1	0.16	2.95	56.1
154	30	1.1	100	350	34.5	10.5	7.3	3.2	0.22	2.89	61.2
155	30	1.1	100	1000	40.0	11.7	7.6	4.1	0.30	2.78	63.8
156	30	1.1	100	1400	44.0	13.0	8.0	5.0	0.35	2.73	64.3
157	30	1.1	100	2000	45.9	13.9	8.3	5.6	0.38	2.65	64.0
158	0.2	0.116	150	0	38.7	12.1	8.6	3.5	1.68	2.95	61.0
159	0.2	0.116	150	230	39.3	12.2	8.7	3.5	1.71	2.95	61.3
160	0.2	0.116	150	450	40.0	12.4	8.8	3.6	1.72	2.93	61.8

TABLE 2 continued

Run No	P (mmHg)	$\dot{m}$ (g/sec)	I (amps)	B (gauss)	U (volts)	U_A (volts)	U_I (volts)	U_{CR} (volts)	U_{Conv} (volts)	U_C (volts)	η (%)
161	0.2	0.116	150	900	42.2	12.7	9.0	3.7	1.80	2.86	63.0
162	0.2	0.116	150	1250	44.5	13.5	9.7	3.8	1.86	2.79	63.4
163	0.2	0.116	150	1800	46.3	13.8	9.8	4.0	1.88	2.70	64.4
164	0.2	0.116	150	2000	47.0	14.1	10.0	4.1	1.89	2.65	64.5
165	0.5	0.218	150	0	37.7	12.0	10.0	2.0	1.71	2.99	60.2
166	0.5	0.218	150	230	38.7	12.4	10.1	2.3	1.67	2.91	60.5
167	0.5	0.218	150	450	39.5	12.7	10.2	2.5	1.66	2.87	60.5
168	0.5	0.218	150	680	40.4	12.9	10.3	2.6	1.65	2.84	61.1
169	0.5	0.218	150	900	41.2	12.8	10.3	2.5	1.72	2.87	61.9
170	0.5	0.218	150	1250	43.5	13.4	10.5	2.9	1.84	2.84	62.8
171	0.5	0.218	150	1800	45.9	14.1	10.8	3.3	1.93	2.77	63.2
172	0.5	0.218	150	2000	46.8	14.4	11.0	3.4	1.96	2.71	63.5

** 0.95 cm cathode diameter is used for these data, Configuration 2.

TABLE 3 CATHODE HEAT TRANSFER (Calculated)

B.C.	Q_R(kW)	Q_C(kW)
a	0.68	0
b	0.54	0.3
c	0.46	0.5
d	0.28	1.16

TABLE 4 AMMONIA DATA (Configuration 1)

Run No	P (mmHg)	$\dot{m}$ (g/sec)	I (amps)	B (gauss)	U (volts)	U_A (volts)	U_C (volts)	η (%)
201	1.5	0.06	200	0	57.0	19.6	1.6	62.8
202	1.5	0.06	400	0	34.0	16.0	1.0	50.0
203	1.5	0.06	300	0	31.0	17.5	0.9	40.7
204	1.0	0.06	400	0	43.5	20.0	1.0	51.8
205	1.5	0.06	200	0	39.6	18.7	1.3	49.5
206	2.0	0.12	200	0	50.0	18.6	1.4	60.0
207	1.0	0.18	200	0	60.6	18.9	1.6	66.1
208	1.0	0.12	400	0	50.5	19.6	0.9	59.5
209	2.0	0.06	400	0	42.8	19.2	1.0	52.8
210	2.0	0.09	400	0	47.0	19.4	1.0	56.6
211	1.5	0.06	300	0	45.3	19.9	1.3	51.0
212	1.8	0.09	300	0	48.8	18.3	1.2	60.1
213	2.0	0.12	300	0	52.8	18.9	1.2	62.0
214	2.0	0.15	300	0	55.2	18.8	1.2	63.8
215	1.0	0.06	200	0	33.0	19.0	1.5	37.9

TABLE 4 continued

Run No	P (mmHg)	$\dot{m}$ (g/sec)	I (amps)	B (gauss)	U (volts)	U_A (volts)	U_C (volts)	η (%)
216	1.0	0.12	200	0	37.3	17.5	1.5	49.1
217	1.0	0.18	200	0	42.0	17.1	1.5	55.7
218	1.0	0.12	300	0	35.7	16.8	1.1	50.0
219	1.0	0.06	200	0	33.5	18.8	1.6	39.1
220	1.0	0.18	150	0	48.0	18.4	2.2	57.1
221	1.0	0.12	300	0	39.0	17.8	1.2	51.3
222	1.0	0.18	300	0	42.0	16.2	1.2	58.6
223	1.0	0.06	400	0	29.3	17.4	1.0	37.5
224	1.0	0.12	400	0	39.7	17.4	0.9	28.7
225	1.0	0.06	500	0	30.0	19.3	0.8	30.0
226	1.0	0.06	300	0	32.5	20.0	1.2	34.8
227	1.0	0.06	300	50	39.0	20.6	1.2	46.7
228	1.0	0.06	300	1000	47.2	20.9	1.2	53.3
229	1.0	0.06	300	1500	52.5	22.7	1.3	54.3
230	1.0	0.06	300	2000	57.5	26.2	1.2	52.4

TABLE 4 continued

Run No	P (mmHg)	$\dot{m}$ (g/sec)	I (amps)	B (gauss)	U (volts)	U_A (volts)	U_C (volts)	η (%)
231	1.0	0.06	200	0	36.0	17.4	1.5	47.5
232	2.0	0.09	200	0	37.0	17.0	1.5	50.0
233	2.0	0.09	200	330	41.0	18.4	1.5	51.5
234	2.0	0.09	200	670	45.7	18.8	1.5	55.6
235	2.0	0.09	200	1000	50.0	19.2	1.5	58.6
236	2.0	0.09	200	1330	55.0	19.7	1.5	59.7
237	2.0	0.09	200	1670	63.0	21.0	1.5	64.3
238	2.0	0.09	200	2000	68.0	21.8	1.5	65.7
239	2.0	0.09	200	1670	60.0	20.8	1.5	62.8
240	2.0	0.09	200	1330	54.0	19.8	1.5	60.6
241	1.0	0.09	200	1000	50.0	19.4	1.5	58.3
242	2.0	0.09	200	0	38.0	17.5	1.5	50.0
243	2.0	0.09	200	0	36.0	17.0	1.5	48.7
244	2.0	0.09	200	0	37.0	17.4	1.5	46.3
245	2.0	0.09	300	0	39.0	15.9	1.2	56.2

TABLE 4 continued

Run No	P (mmHg)	$\dot{m}$ (g/sec)	I (amps)	B (gauss)	U (volts)	U_A (volts)	U_C (volts)	η (%)
246	2.0	0.09	300	0	37.0	15.4	1.2	55.2
247	2.0	0.09	300	330	43.0	16.9	1.2	58.0
248	2.0	0.09	300	250	42.5	17.1	1.2	57.1
249	2.0	0.09	300	670	47.0	18.0	1.2	59.2
250	2.0	0.09	300	1000	52.0	18.1	1.2	62.9
251	2.0	0.09	300	1330	57.0	19.0	1.2	64.5
252	2.0	0.09	300	1670	63.5	20.4	1.2	66.0
253	2.0	0.09	300	2000	69.0	20.9	1.2	60.2
254	2.0	0.09	300	1670	63.0	20.3	1.2	66.0
255	2.0	0.09	300	1330	56.0	19.2	1.2	62.6
256	2.0	0.09	300	1000	52.0	18.5	1.2	62.2

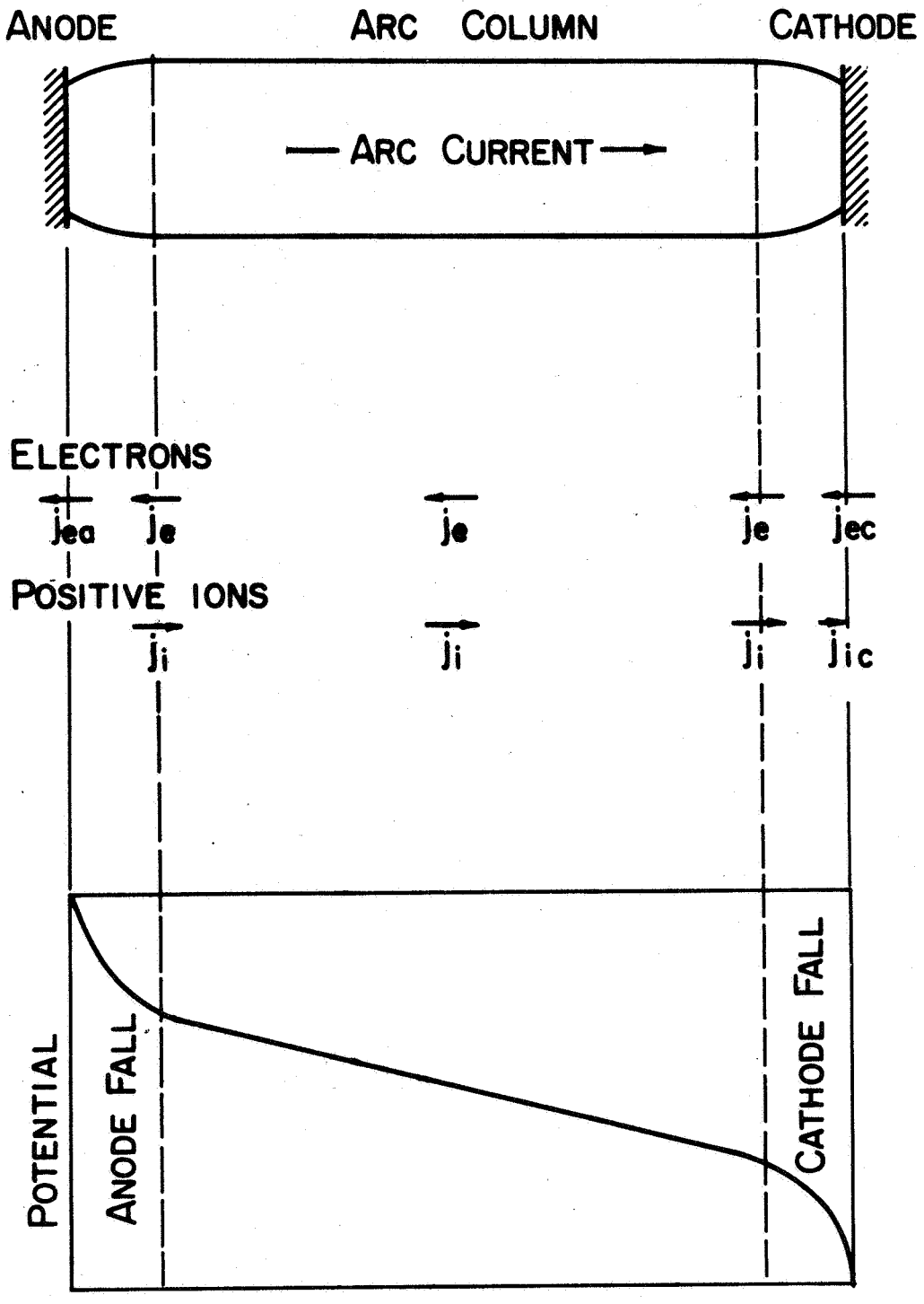

FIGURE 1 ELECTRIC ARC

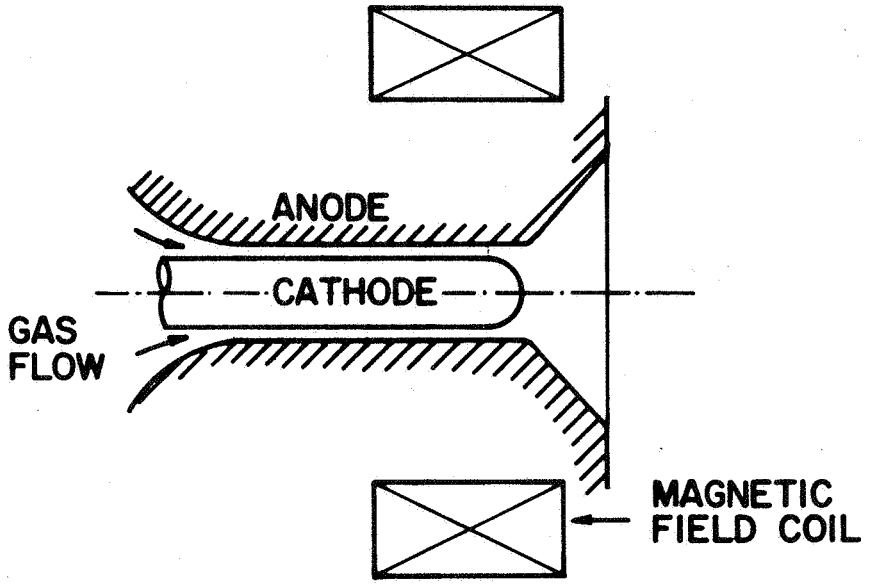

FIGURE 2 SCHEMATIC OF MPD ARC THRUSTER

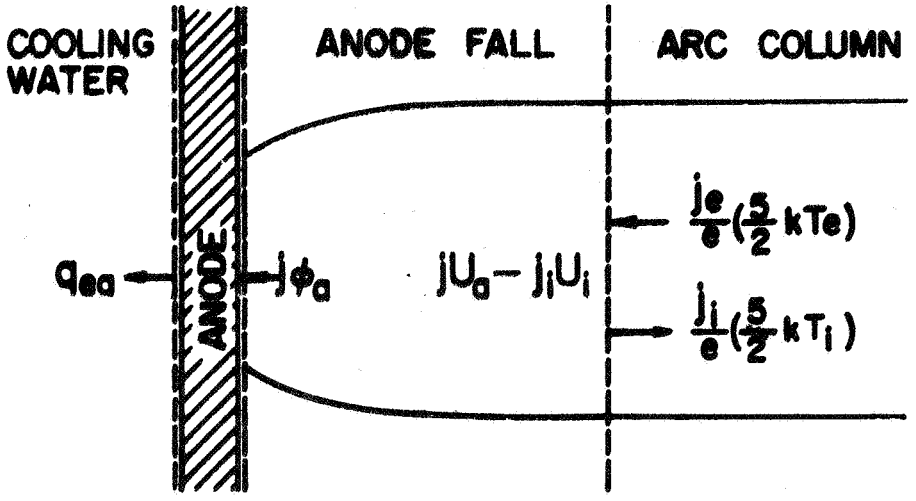

FIGURE 3 ANODE ELECTRON ENERGY BALANCE

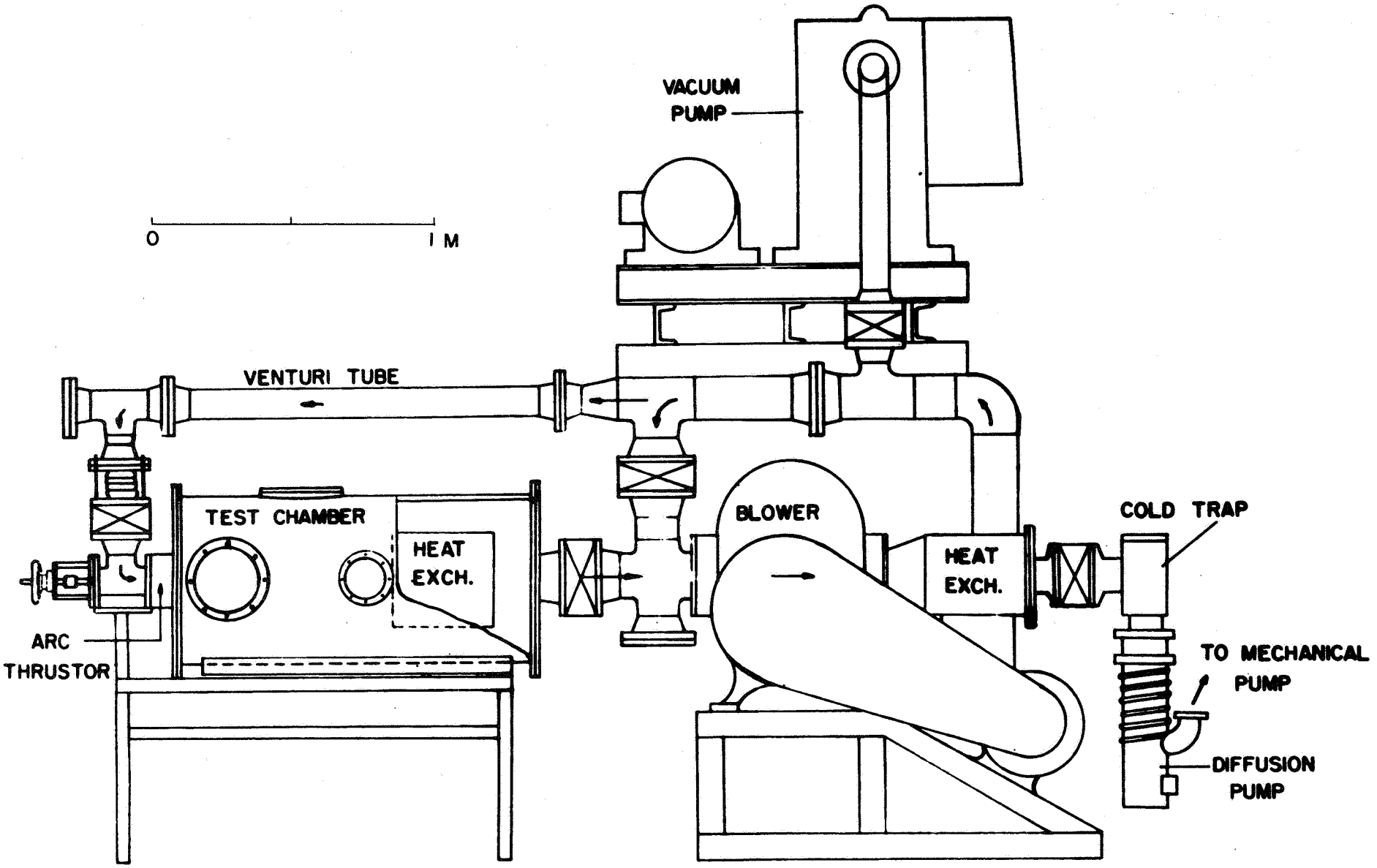

FIGURE 4 ARC TUNNEL

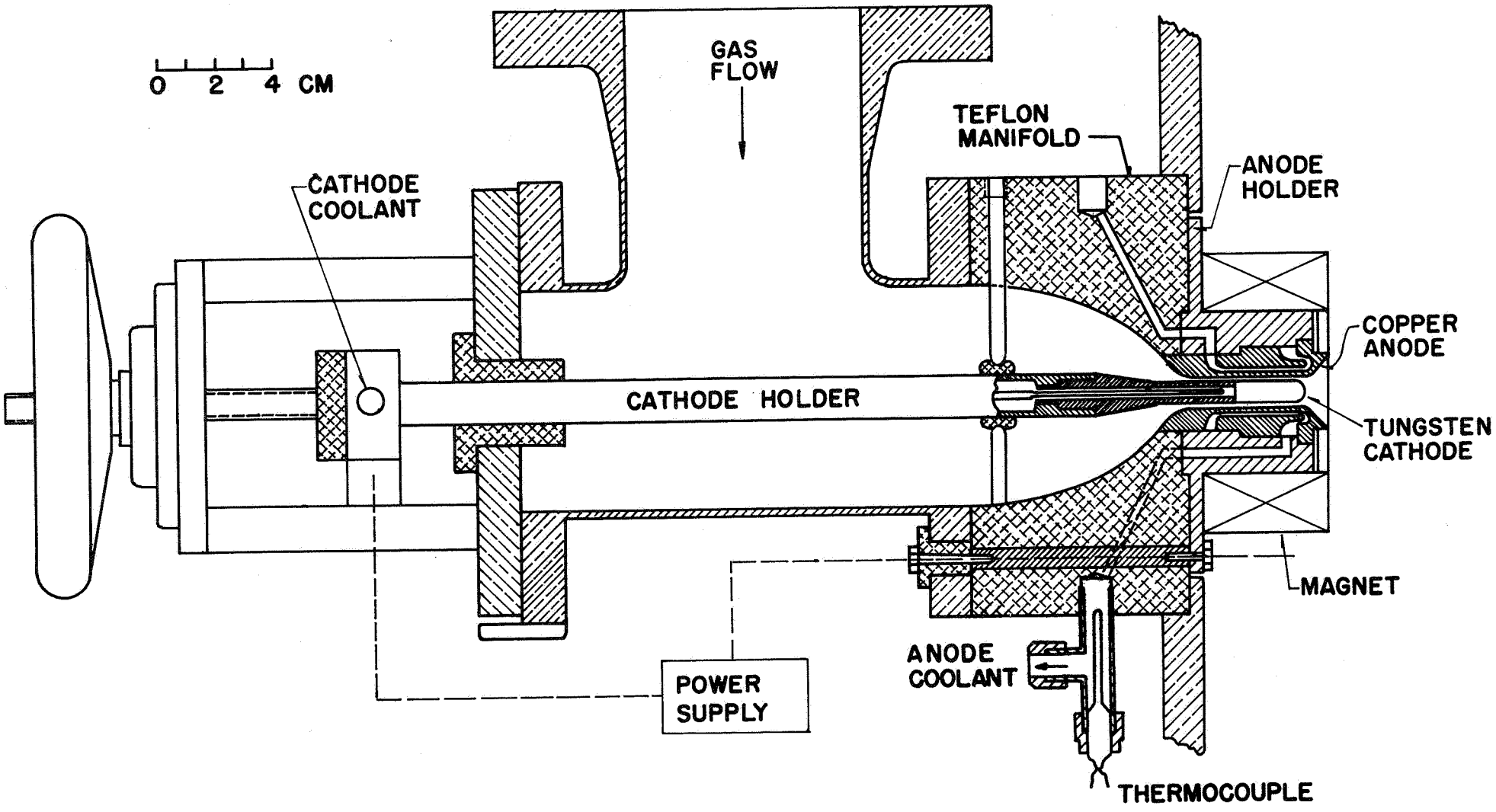

FIGURE 5 ARC JET ASSEMBLY

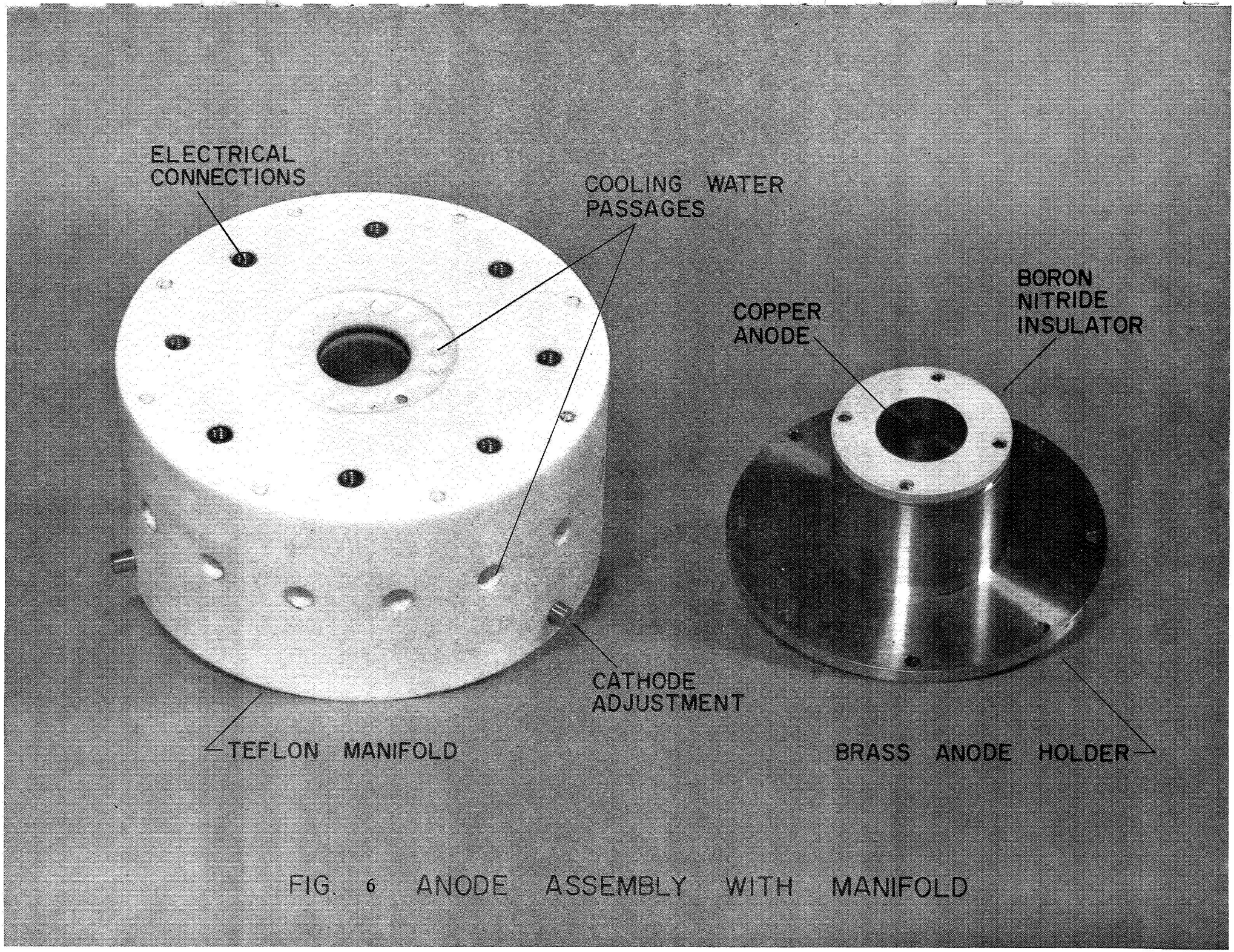

FIG. 6 ANODE ASSEMBLY WITH MANIFOLD

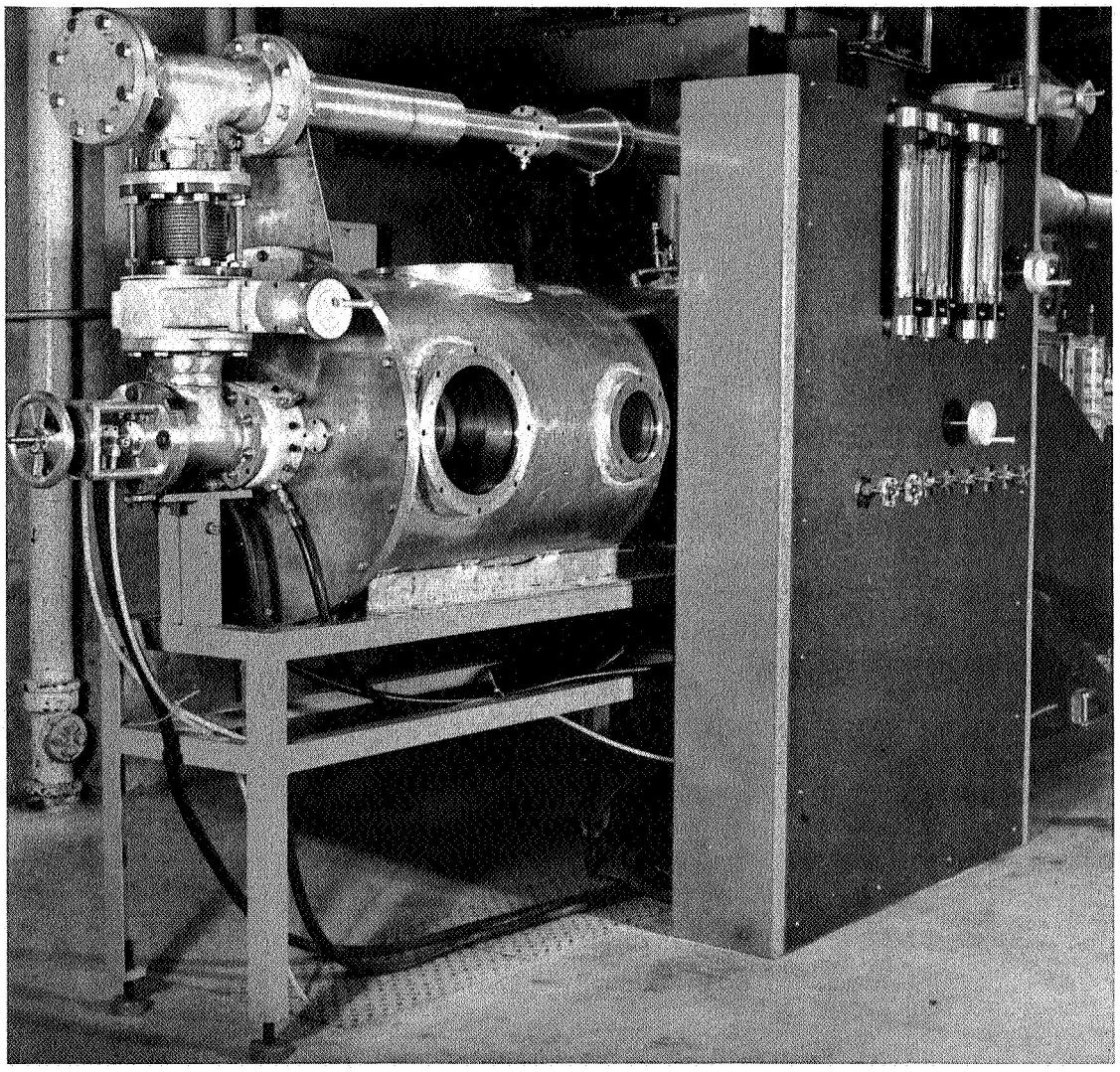

FIG. 7 MODIFICATION OF ARC TUNNEL

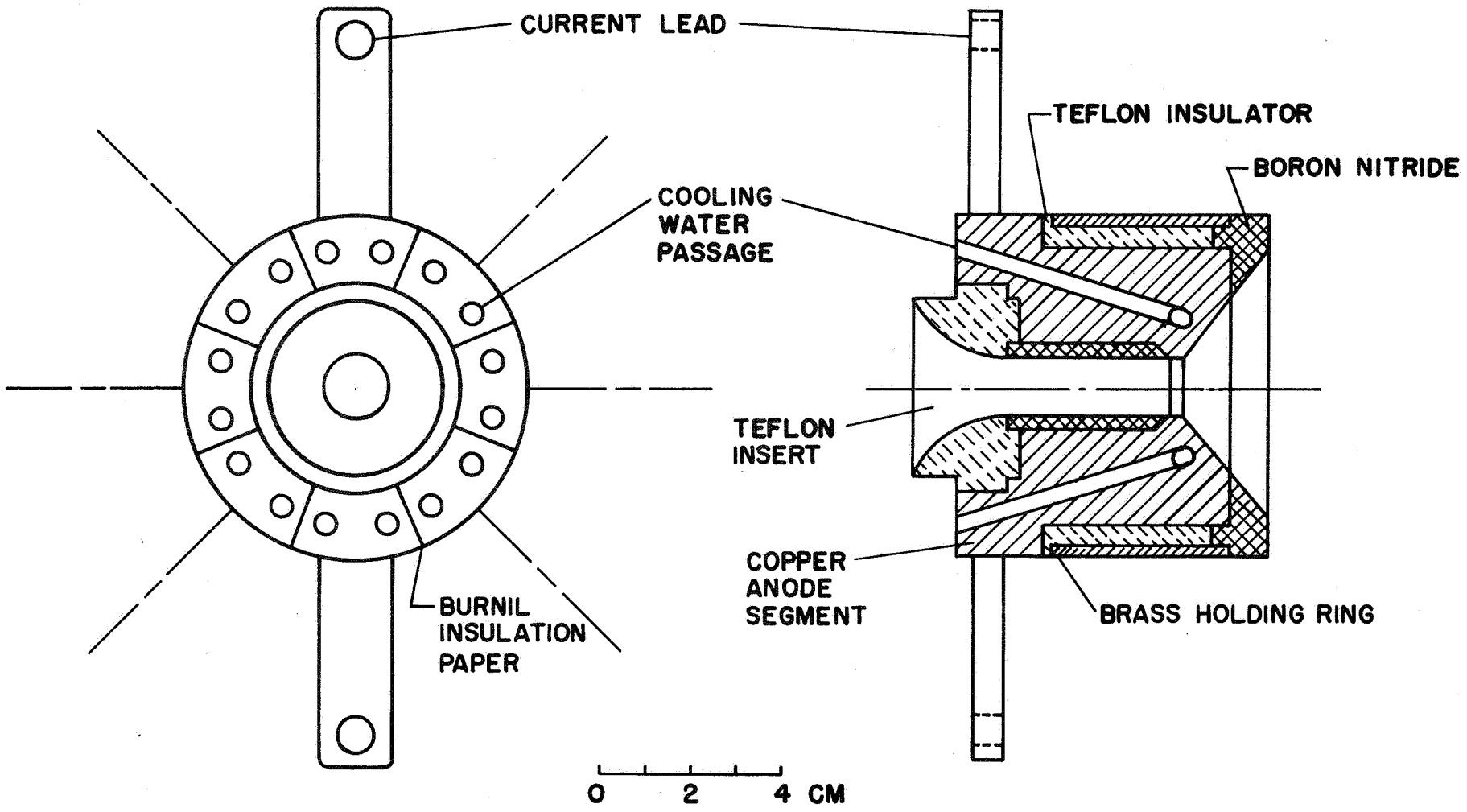

FIGURE 8 LONGITUDINALLY SEGMENTED ANODE

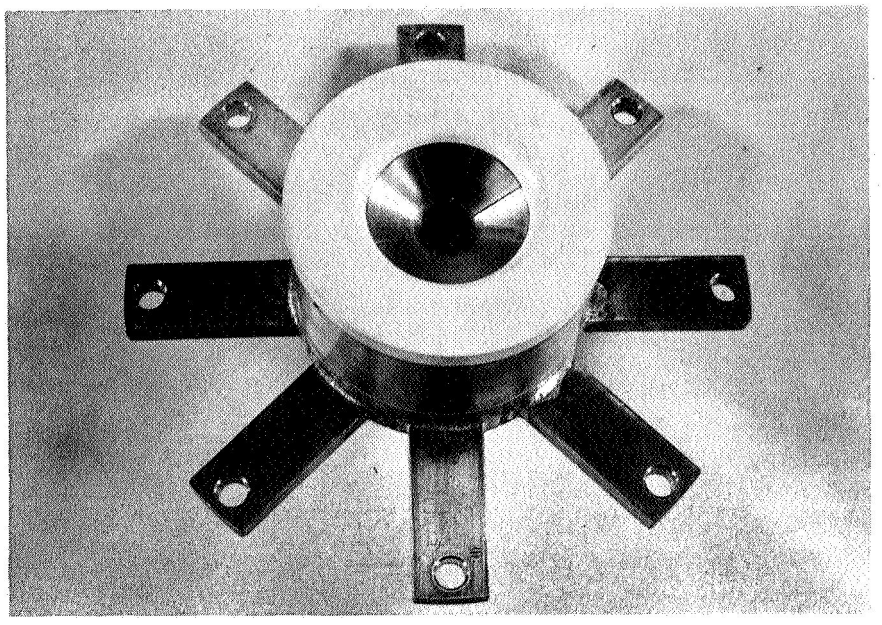

TOP VIEW

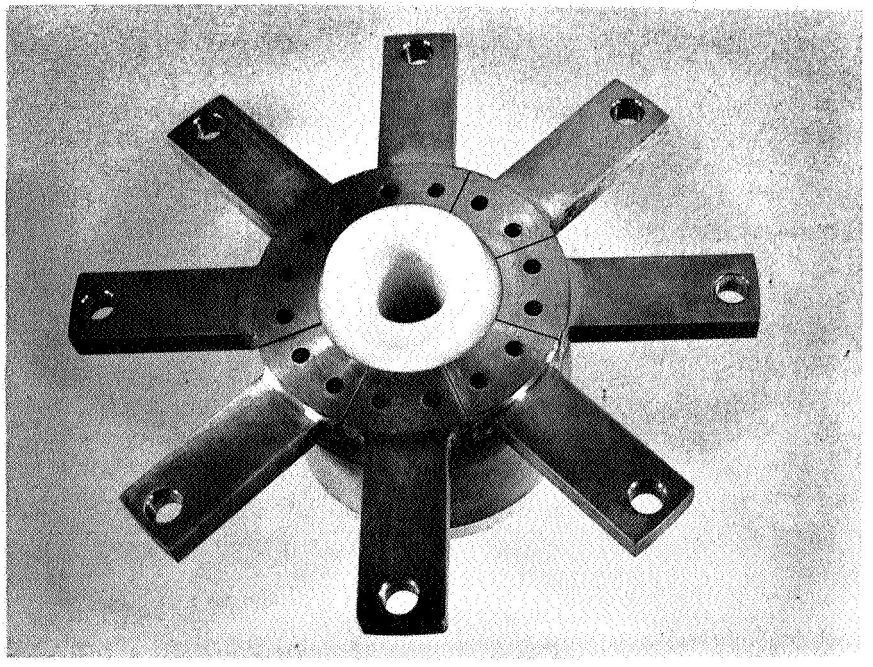

BOTTOM VIEW

FIGURE 8a LONGITUDINALLY SEGMENTED ANODE

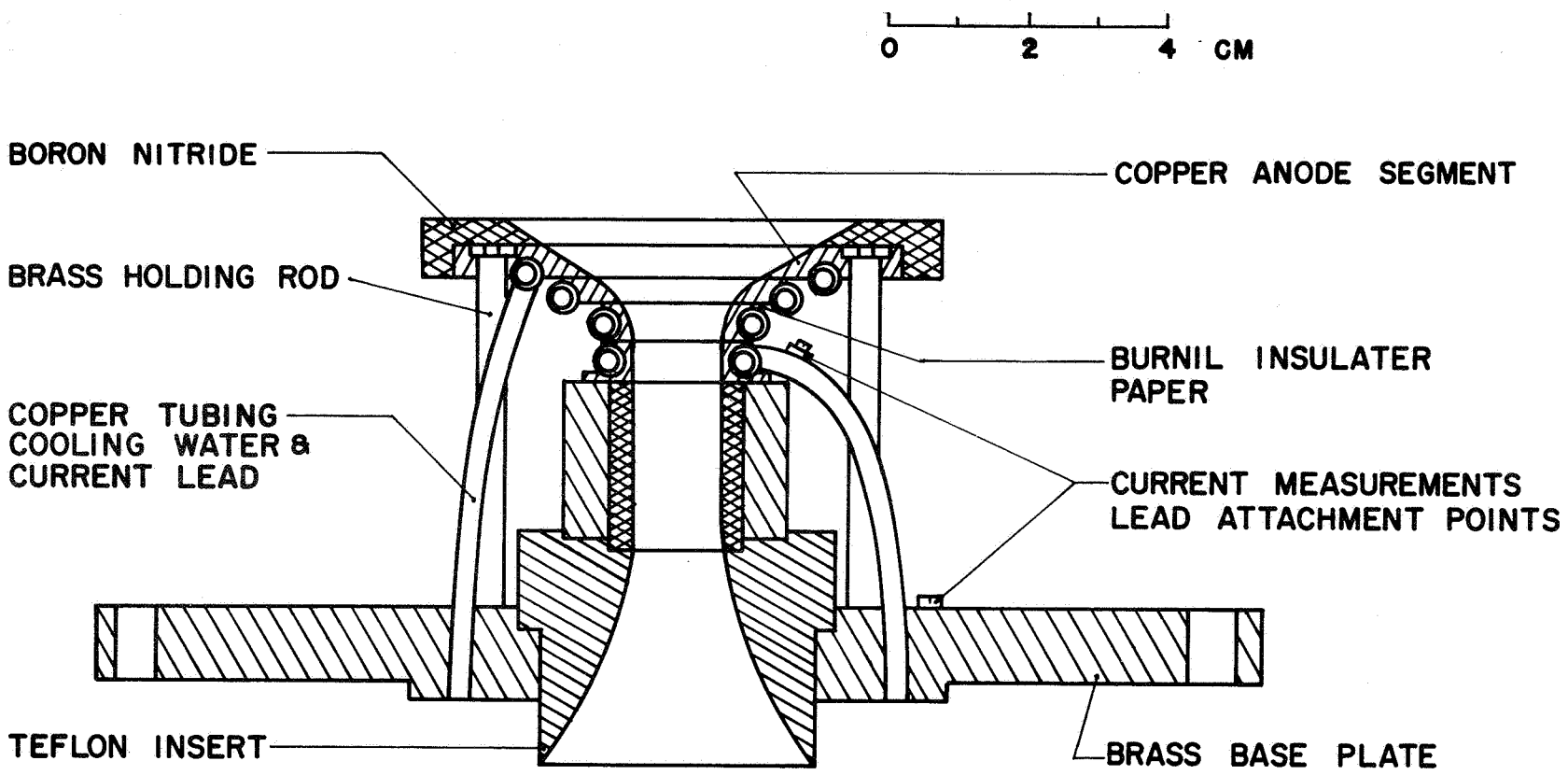

FIGURE 9 AXIALLY SEGMENTED ANODE

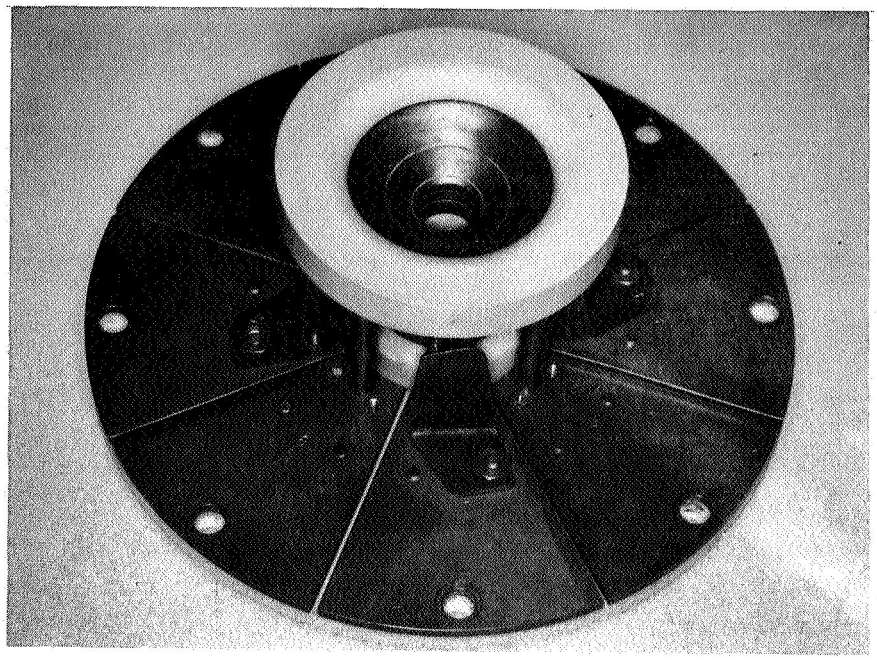

TOP VIEW

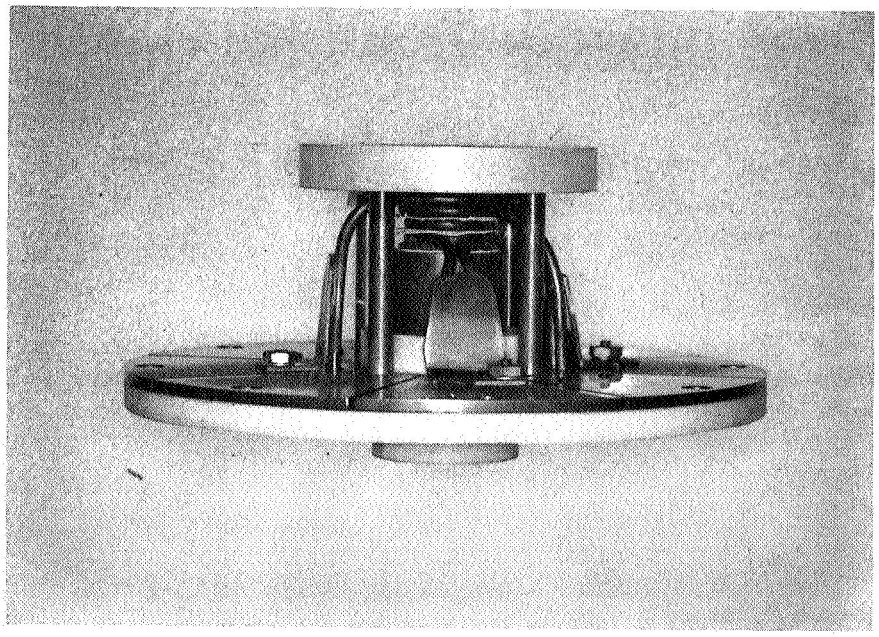

SIDE VIEW

FIGURE 9a AXIALLY SEGMENTED ANODE

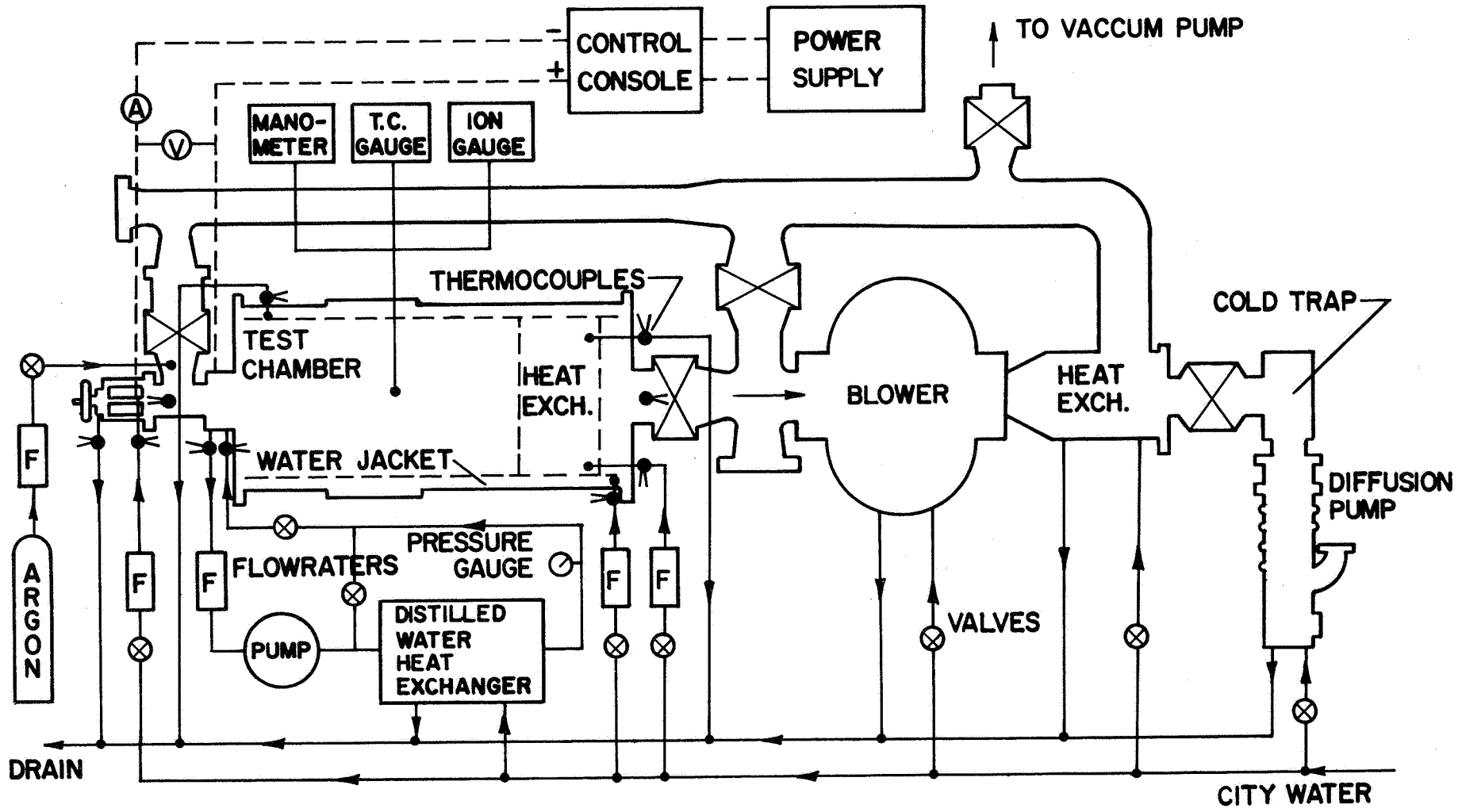

FIGURE 10 ARC TUNNEL SYSTEM SCHEMATIC

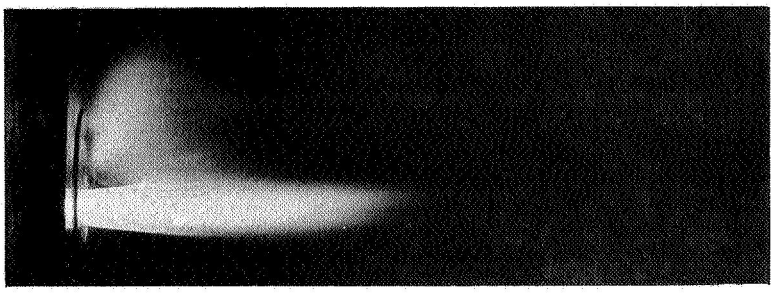

P = 200 mmHg V ≅ 50 m/sec U = 37 volts

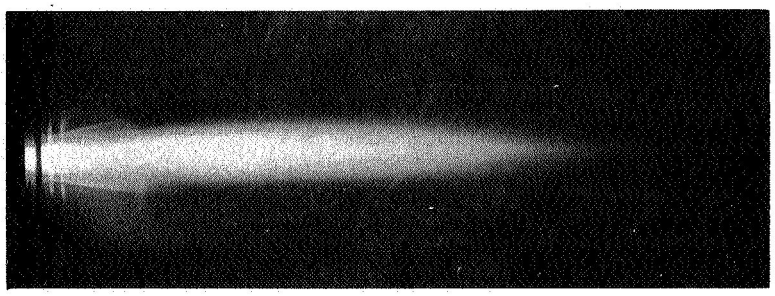

P = 100 mmHg V ≅ 250 m/sec U = 31 volts

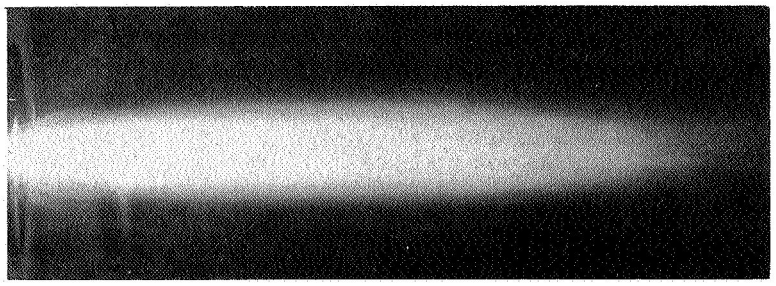

P = 50 mmHg V ≅ 200 m/sec U = 32 volts

FIG. 11 ARGON ARCJET WITHOUT MAGNETIC FIELD (I = 100 amps)

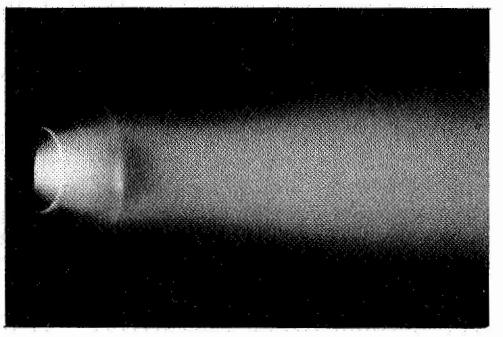

B = 0 gauss

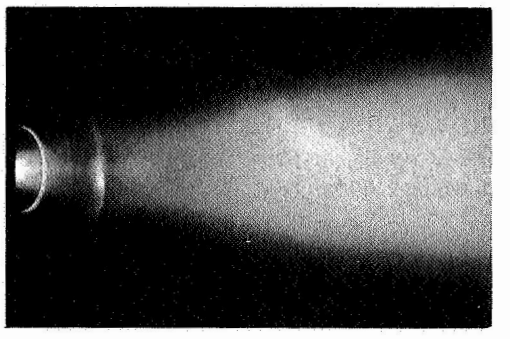

B = 1000 gauss

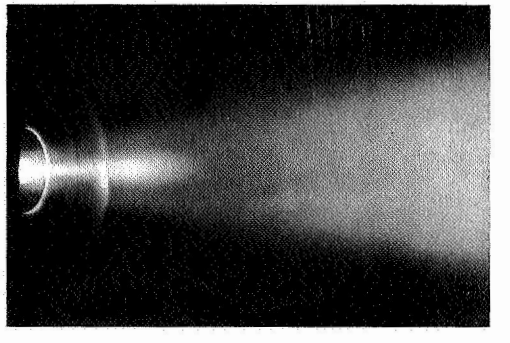

B = 2000 gauss

FIGURE 12 VARIATION OF ARGON ARC WITH MAGNETIC FIELD STRENGTH (I=200amp, P=0.2mmHg, $\dot{m}$ = 0.218 g/sec)

$\dot{m}$ = 0 g/sec

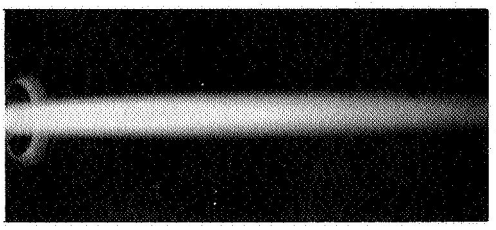

$\dot{m}$ = 0.288 g/sec

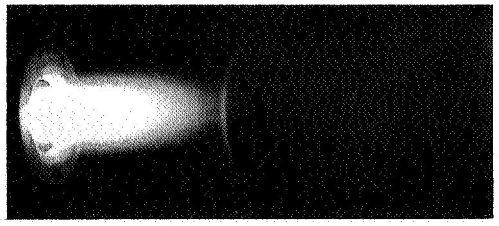

$\dot{m}$ = 0.029 g/sec

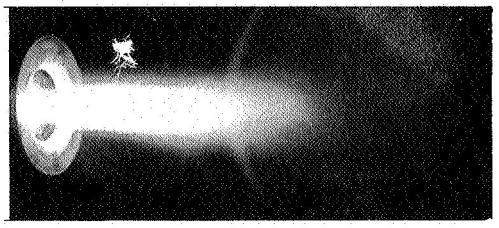

$\dot{m}$ = 0.355 g/sec

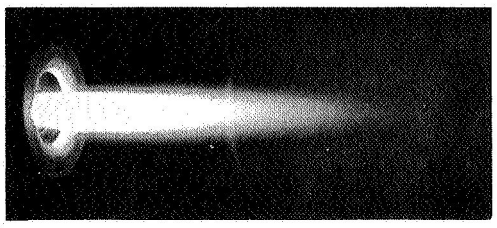

$\dot{m}$ = 0.072 g/sec

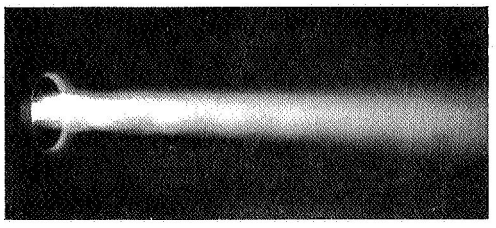

$\dot{m}$ = 1.05 g/sec
(P = 5 mmHg)

FIGURE 13 VARIATION OF ARGON ARC WITH MASS FLOW RATE (I = 200 amp, P = 20 mmHg, B = 0 gauss)

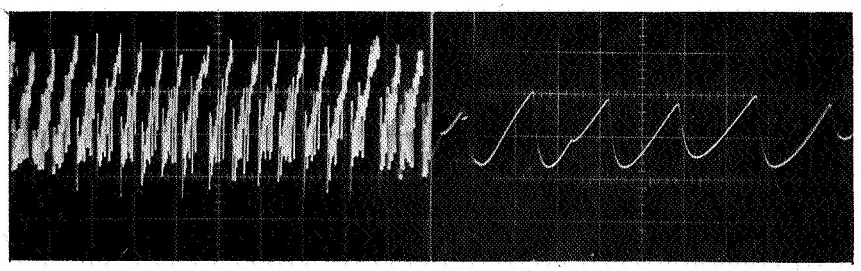

I = 50 amp
P = 200 mmHg
$\dot{m}$ = 1.8 gm/sec
$\overline{U}$ = 27 volt

SWEEP: 10 ms/cm 0.2 ms/cm
VOLTAGE: 2 v/cm 2 v/cm

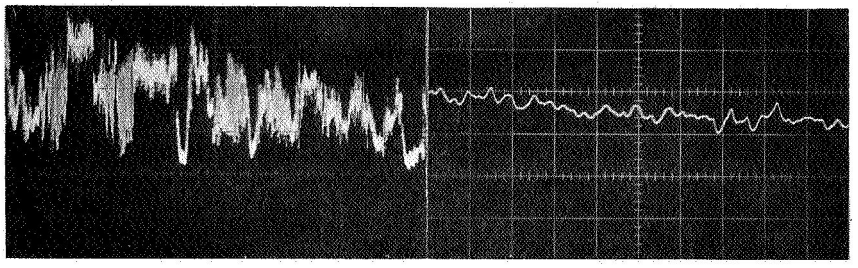

I = 100 amp
P = 200 mmHg
$\dot{m}$ = 7.4 gm/sec
$\overline{U}$ = 34 volt

SWEEP: 10 ms/cm 0.1 ms/cm
VOLTAGE: 2 v/cm 2 v/cm

I = 300 amp
P = 50 mmHg
$\dot{m}$ = 0.96 gm/sec
$\overline{U}$ = 24 volt

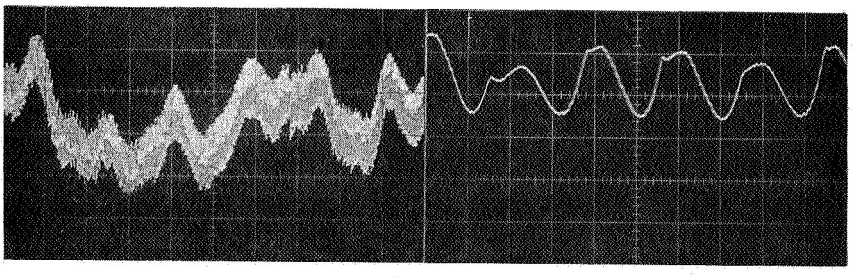

SWEEP: 10 ms/cm 0.1 ms/cm
VOLTAGE: 0.2 v/cm 0.2 v/cm

I = 500 amp
P = 100 mmHg
$\dot{m}$ = 2.2 gm/sec
$\overline{U}$ = 22 volt

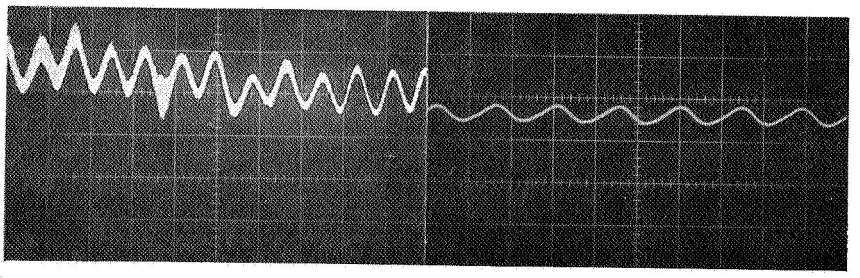

SWEEP: 10 ms/cm 0.02 ms/cm
VOLTAGE: 0.2 v/cm 0.2 v/cm

FIGURE 14 OSCILLOGRAMS OF THE ARC JETS (ARGON)

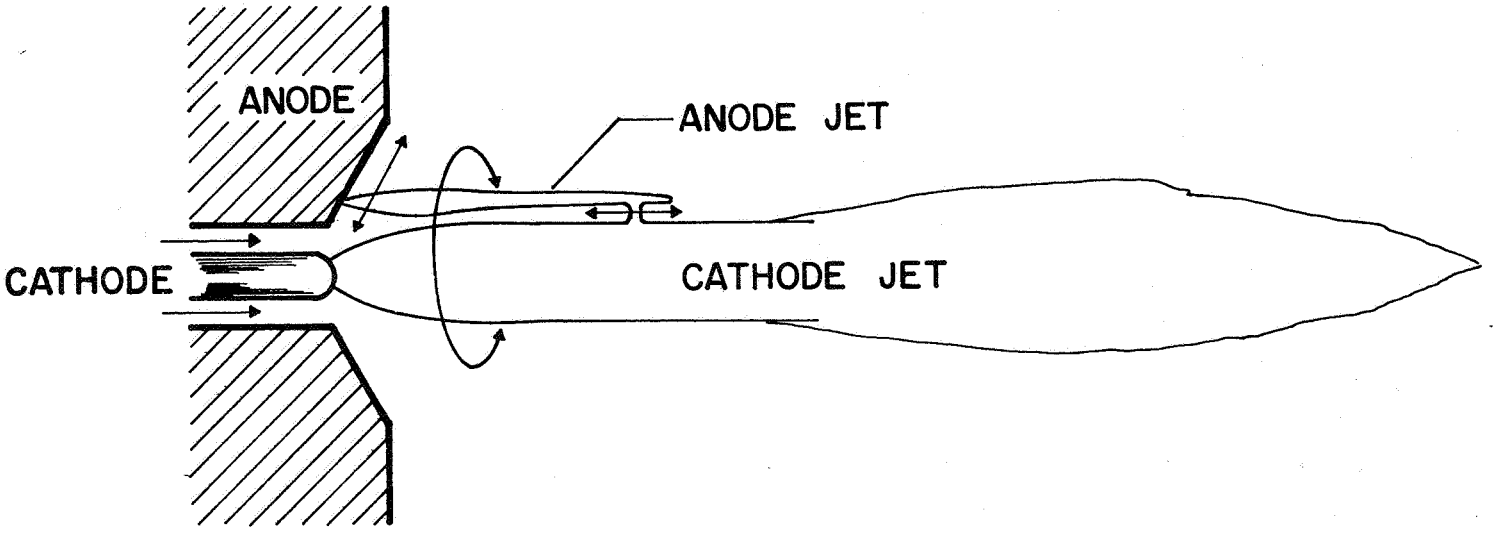

FIGURE 15 SCHEME OF THE ARC JETS

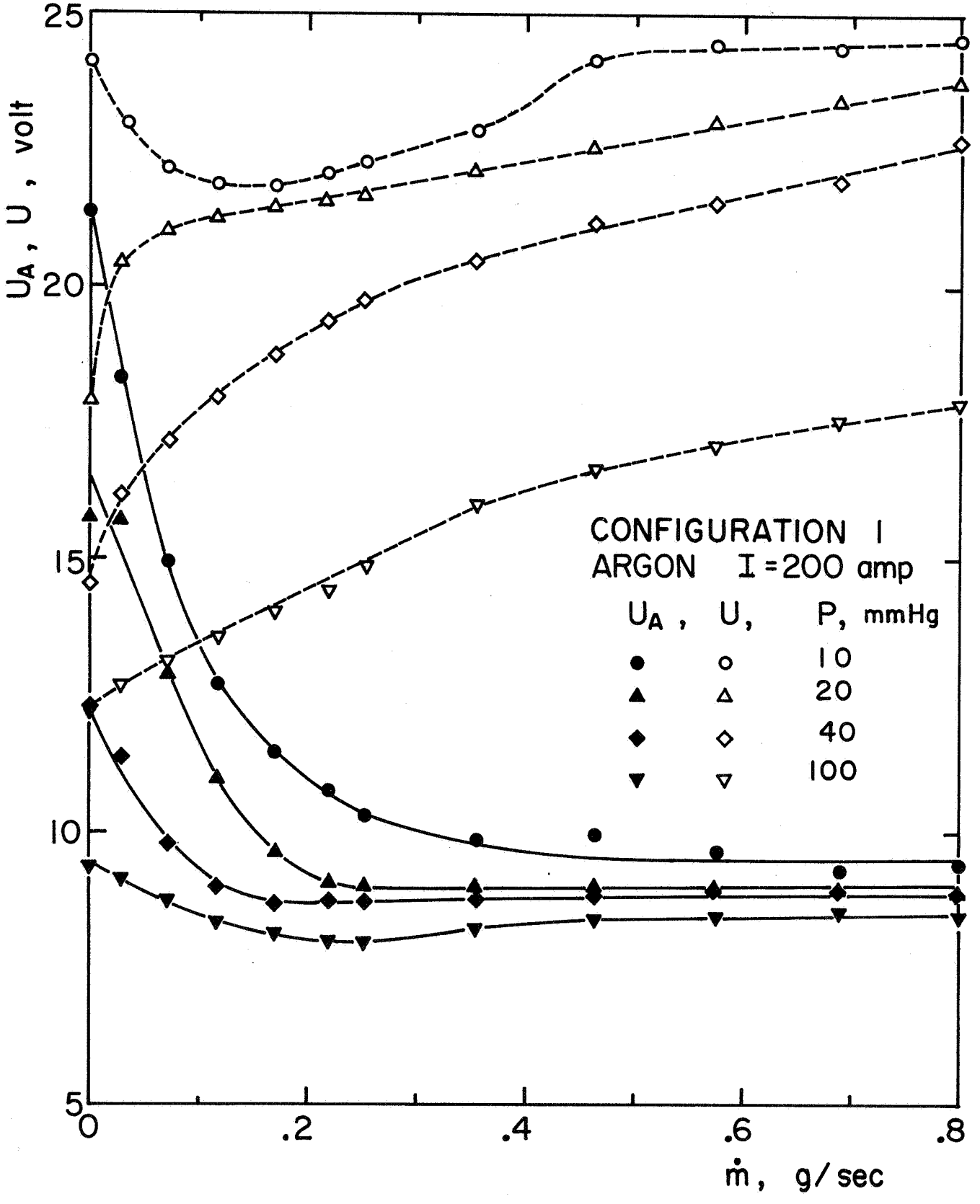

FIGURE 16 EFFECT OF MASS FLOW RATE ON ARC VOLTAGE AND CHARACTERISTIC ANODE VOLTAGE (B=0)

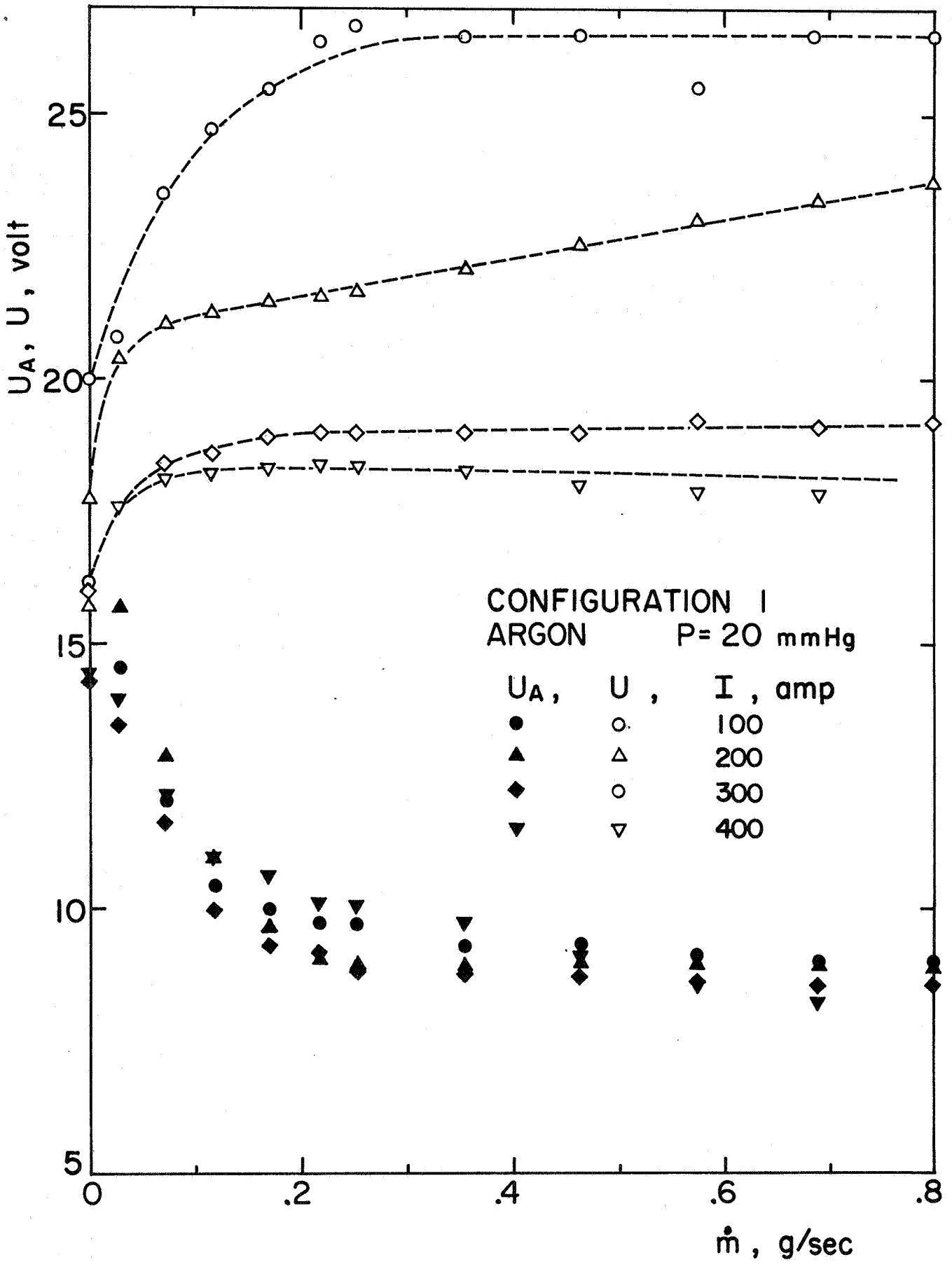

FIGURE 17 EFFECT OF MASS FLOW RATE ON ARC VOLTAGE AND CHARACTERISTIC ANODE VOLTAGE (B=0)

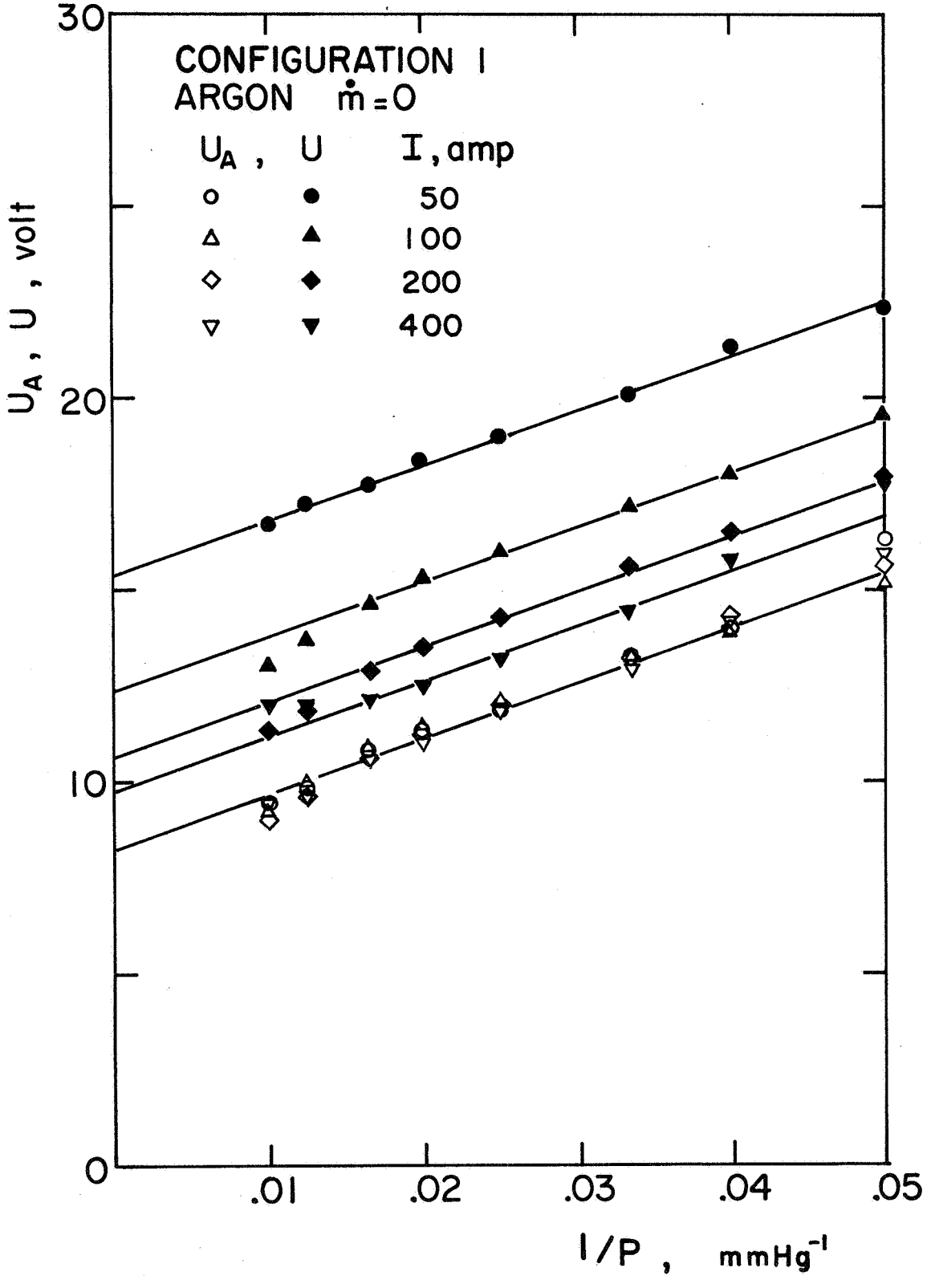

FIGURE 18 ARC VOLTAGE AND CHARACTERISTIC ANODE VOLTAGE AS FUNCTION OF THE RECIPROCAL OF CHAMBER PRESSURE (B=0)

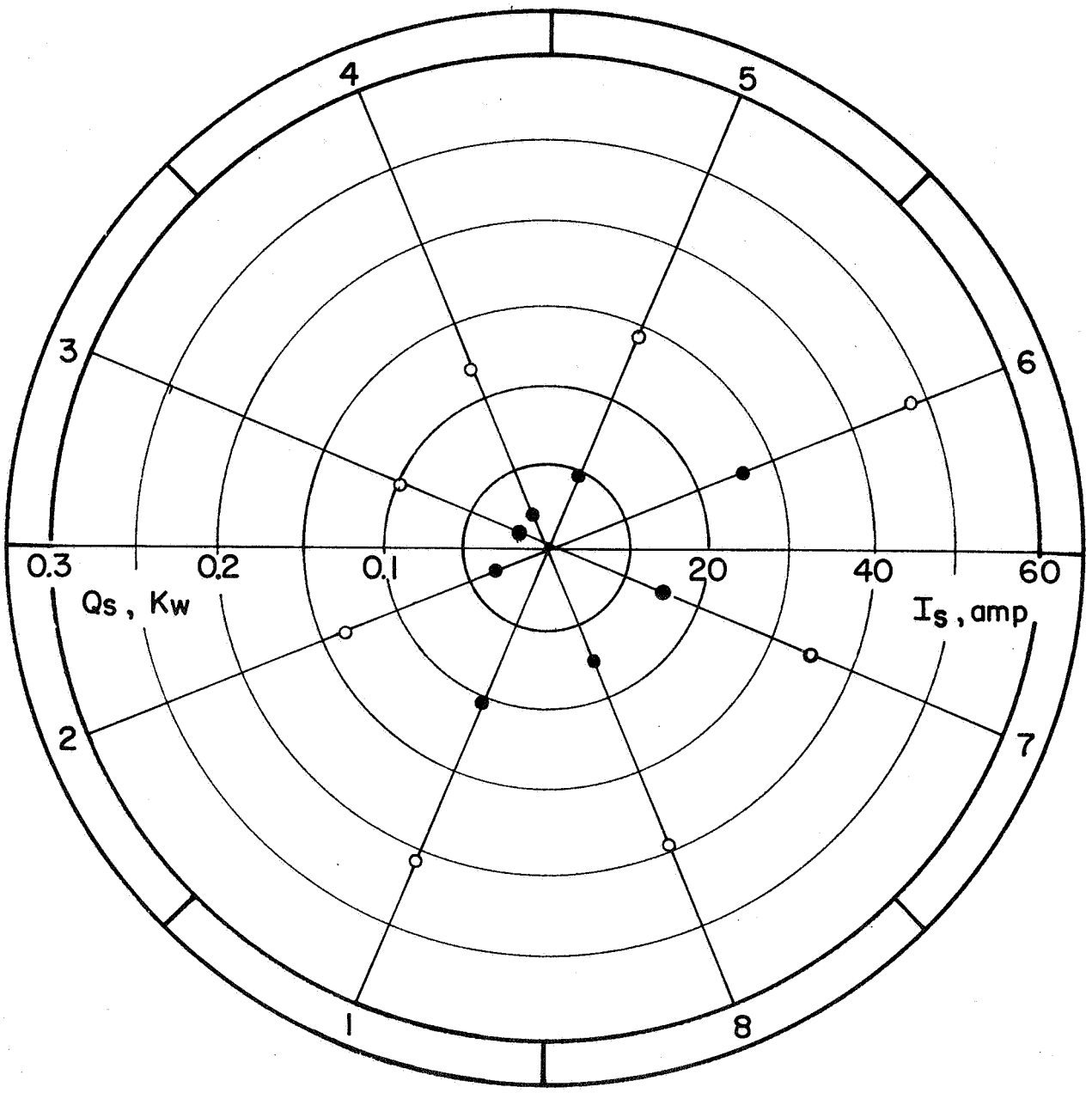

I = 100 amp , P = 30 mmHg , $\dot{m}$ = 0.88 g/sec

- • CURRENT
- ○ HEAT FLUX

FIGURE 19 SEGMENTAL CURRENT AND HEAT FLUX DISTRIBUTION (ARGON, B=0)

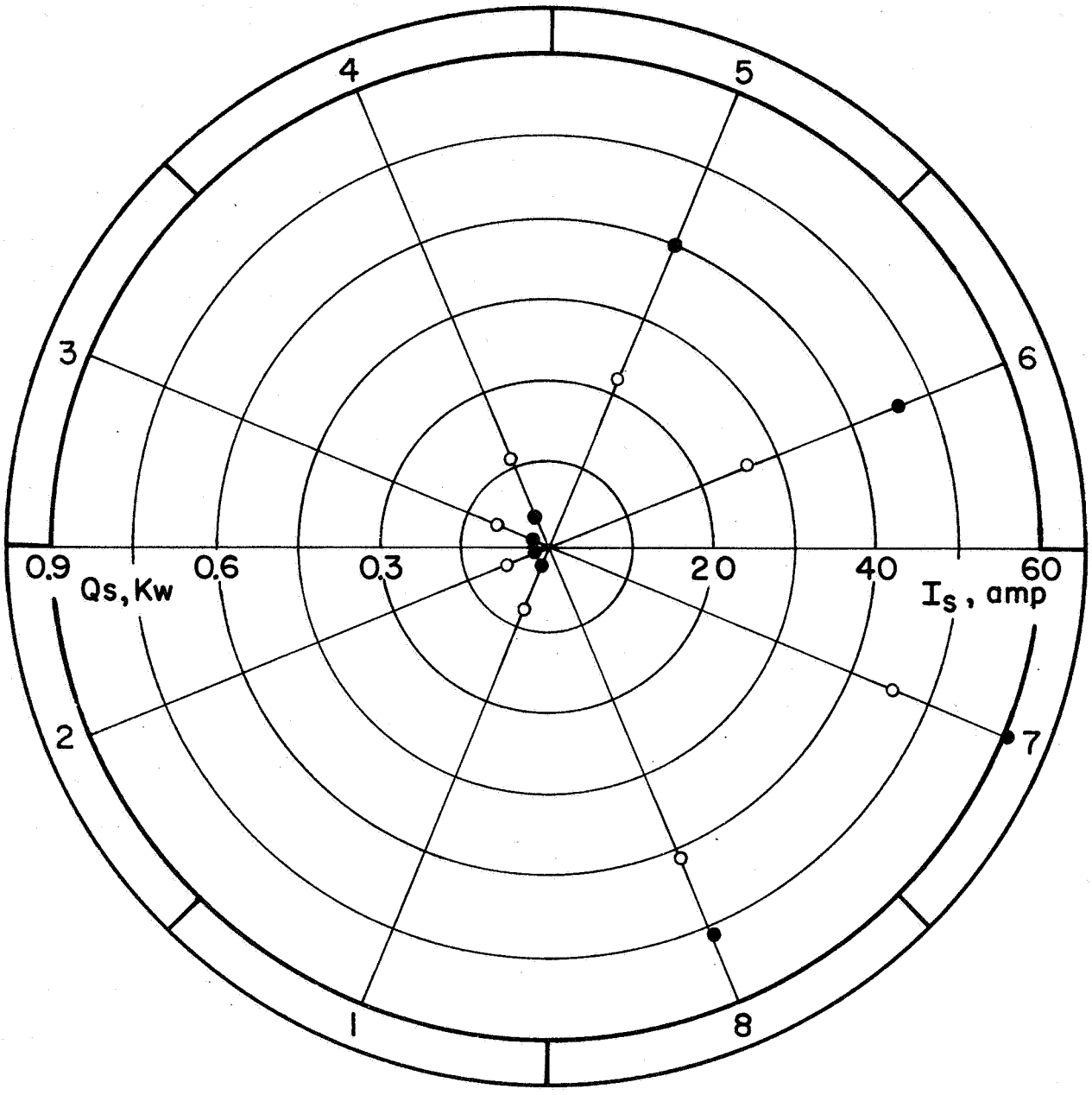

I = 200 amp, P = 30 mm Hg, $\dot{m}$ = 0.8 g/sec

- • CURRENT
- ○ HEAT FLUX

FIGURE 20 SEGMENTAL CURRENT AND HEAT FLUX DISTRIBUTION (ARGON, B=0)

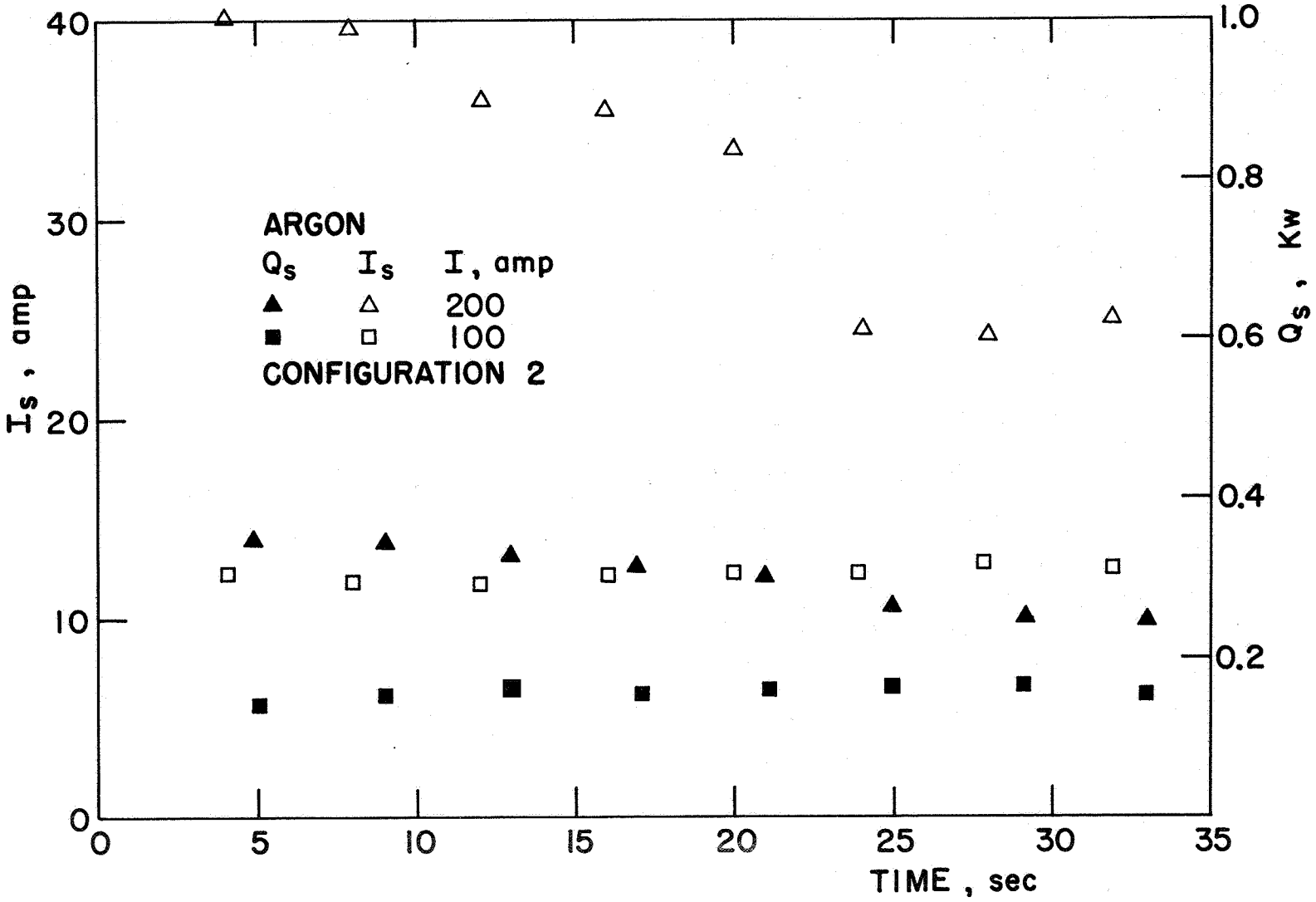

FIGURE 21 TIME DEPEDENCE OF SEGMENTAL CURRENT AND HEAT FLUX (B=0)

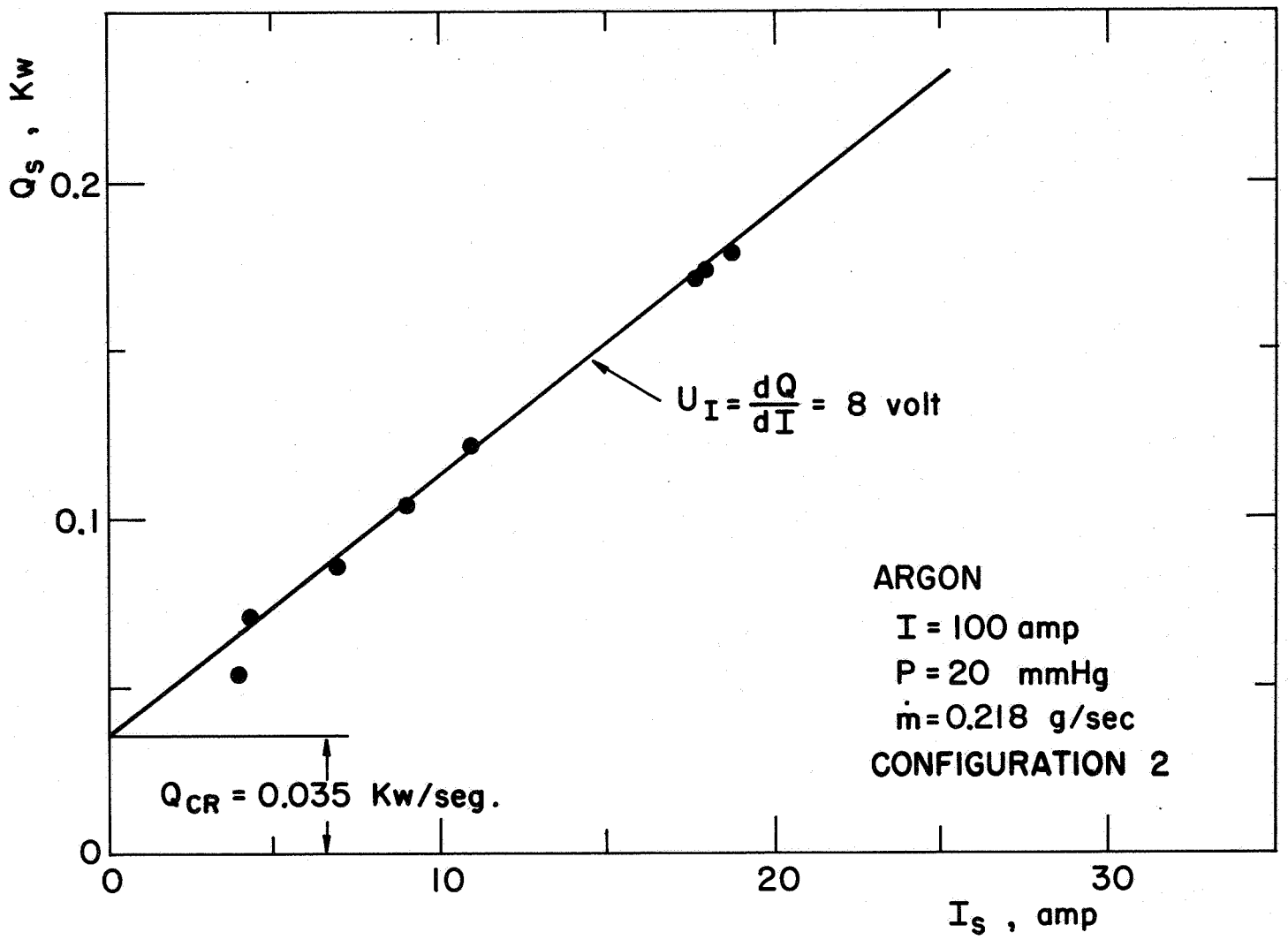

FIGURE 22 SEGMENTAL HEAT FLUX VS. CURRENT (B=0)

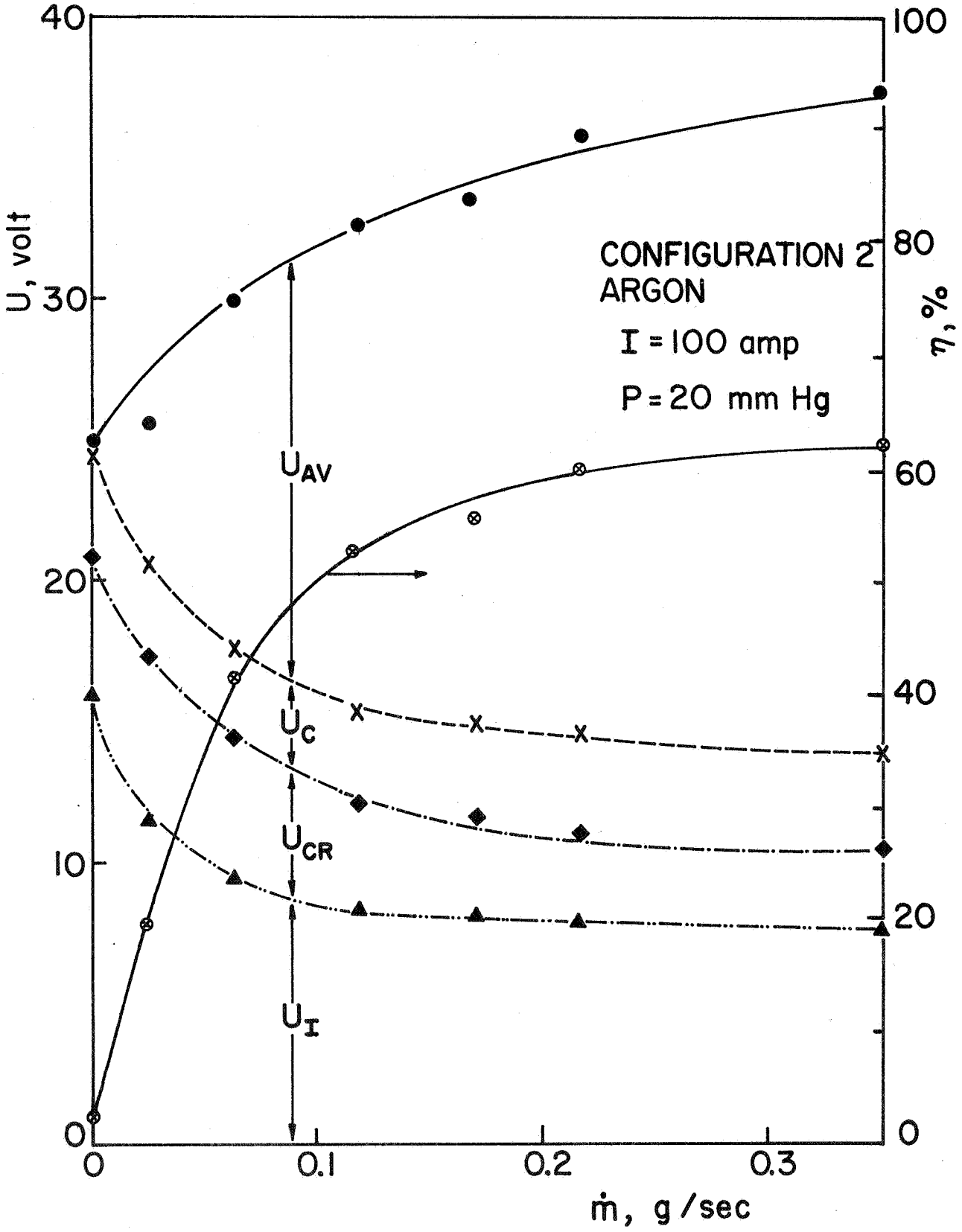

FIGURE 23 MPD ARC ENERGY BALANCE (B=0)

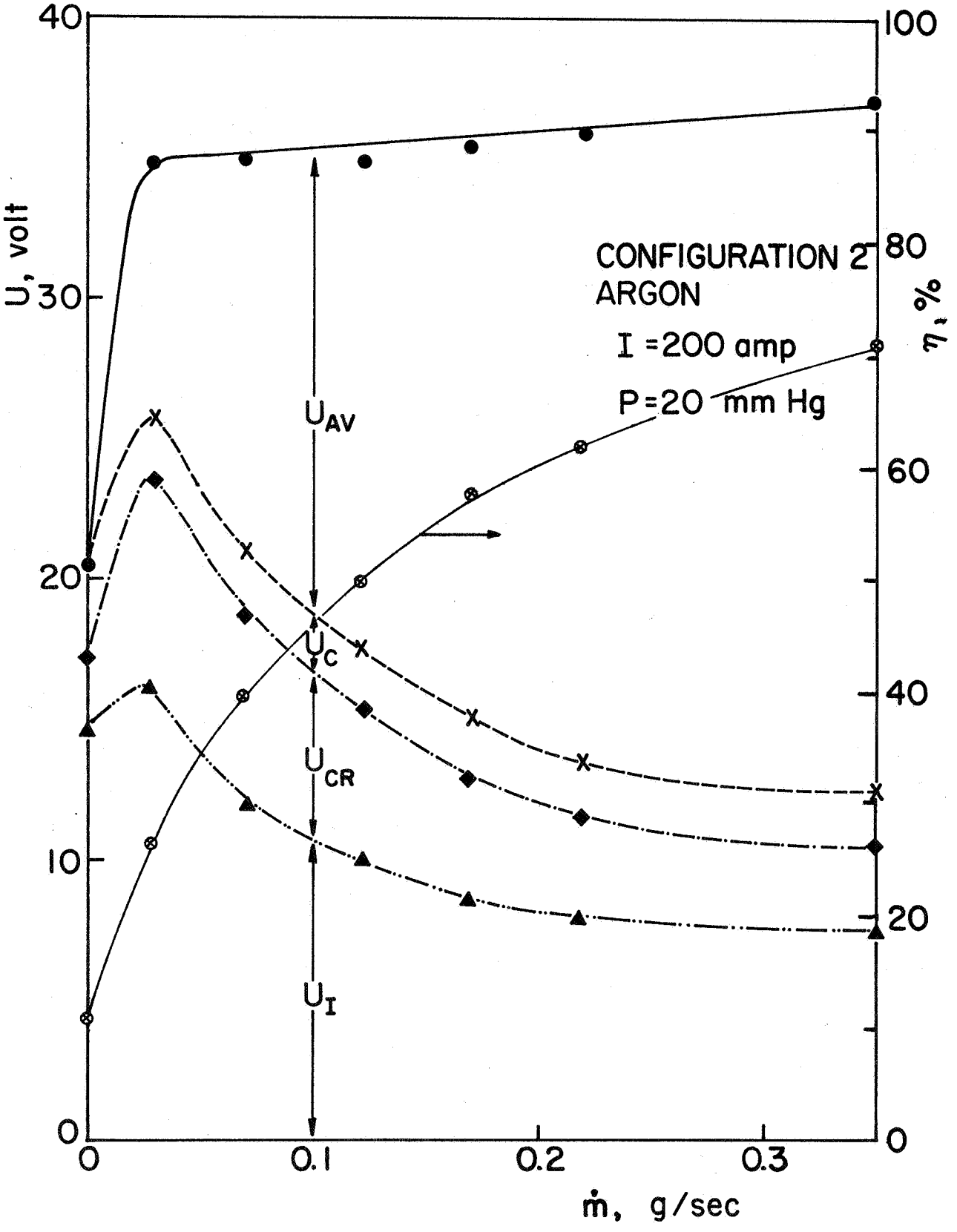

FIGURE 24 MPD ARC ENERGY BALANCE (B=0)

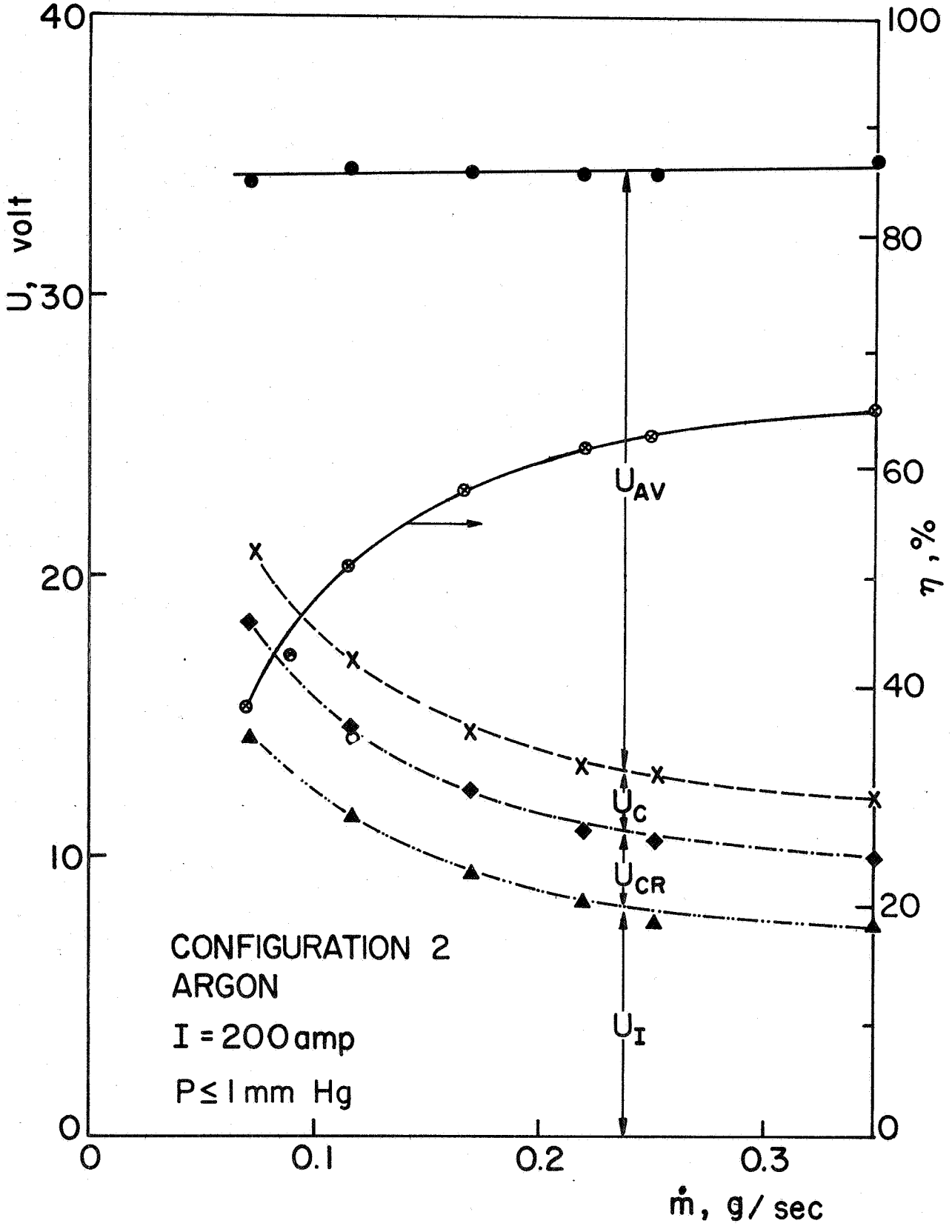

FIGURE 25 MPD ARC ENERGY BALANCE (B=0)

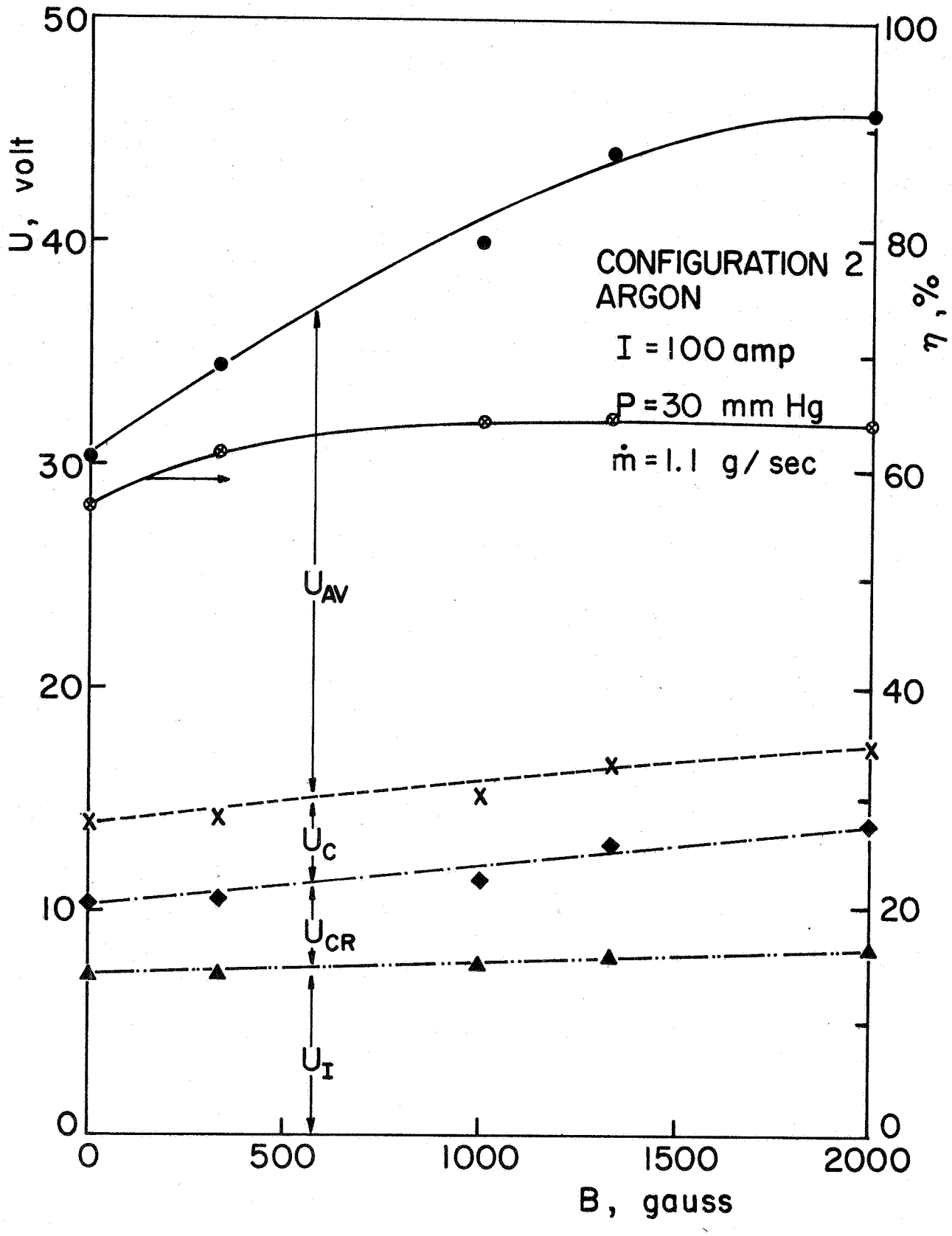

FIGURE 26 EFFECT OF MAGNETIC FIELD STRENGTH ON ENERGY BALANCE

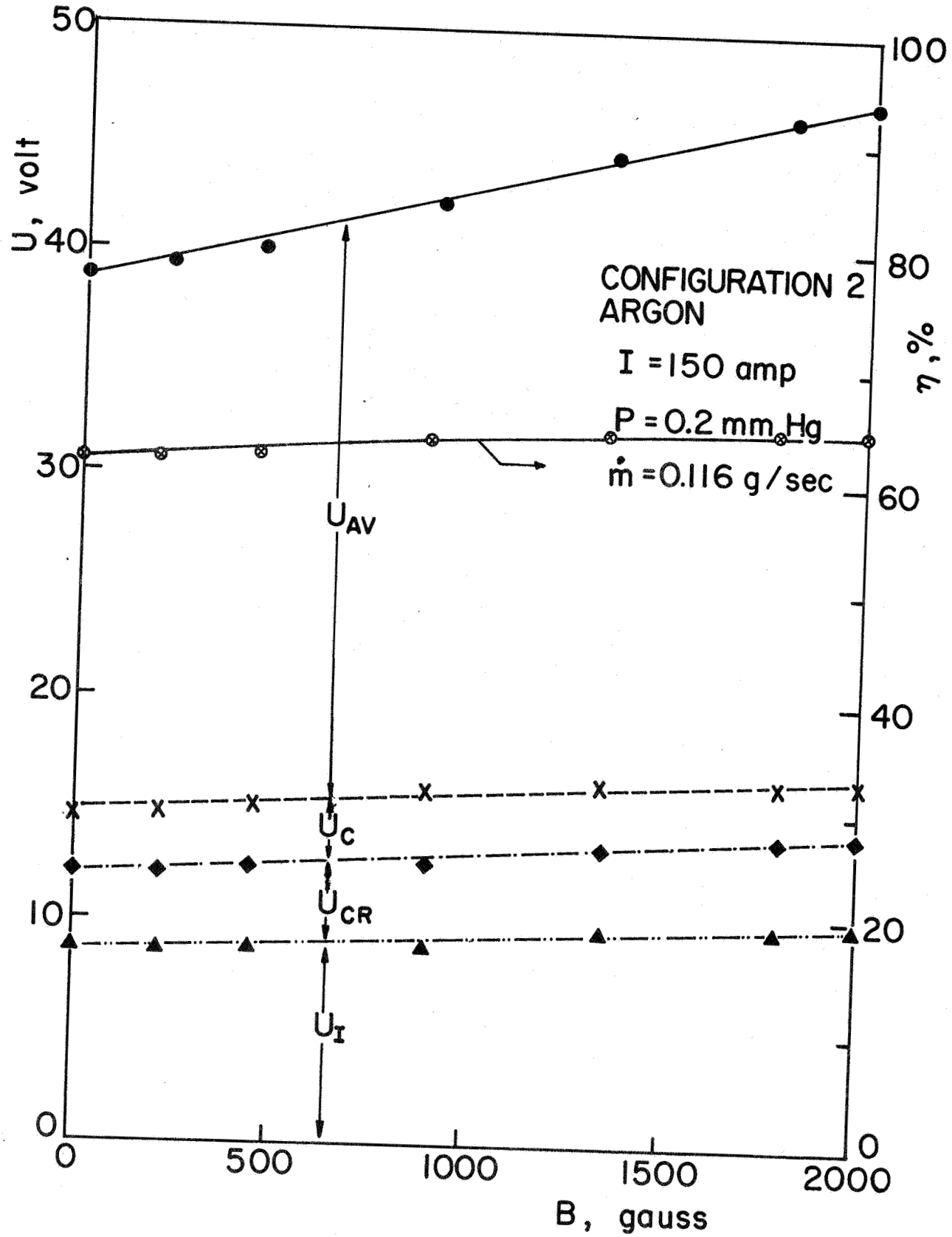

FIGURE 27 EFFECT OF MAGNETIC FIELD STRENGTH ON ENERGY BALANCE

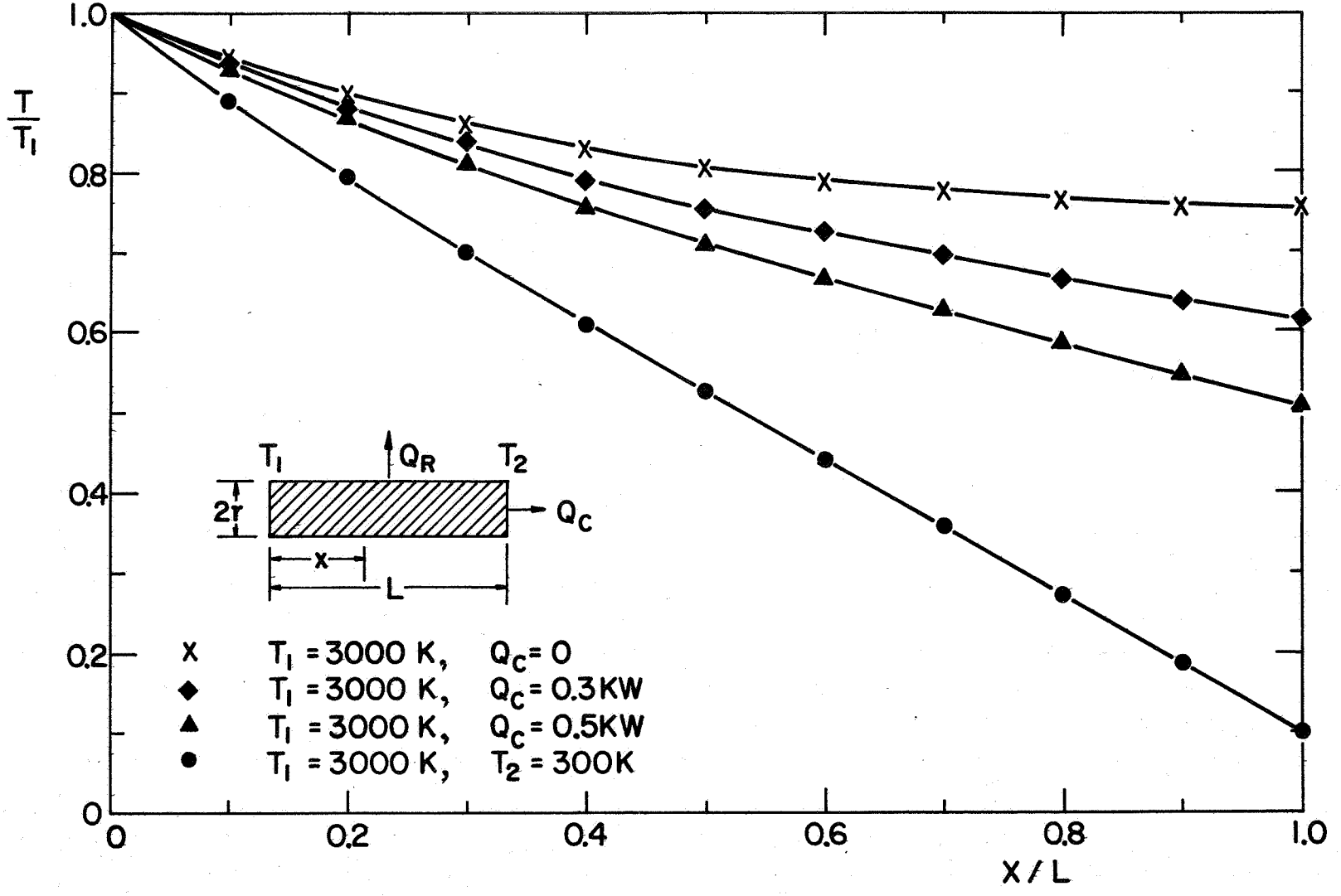

FIGURE 28 CATHODE TEMPERATURE PROFILES

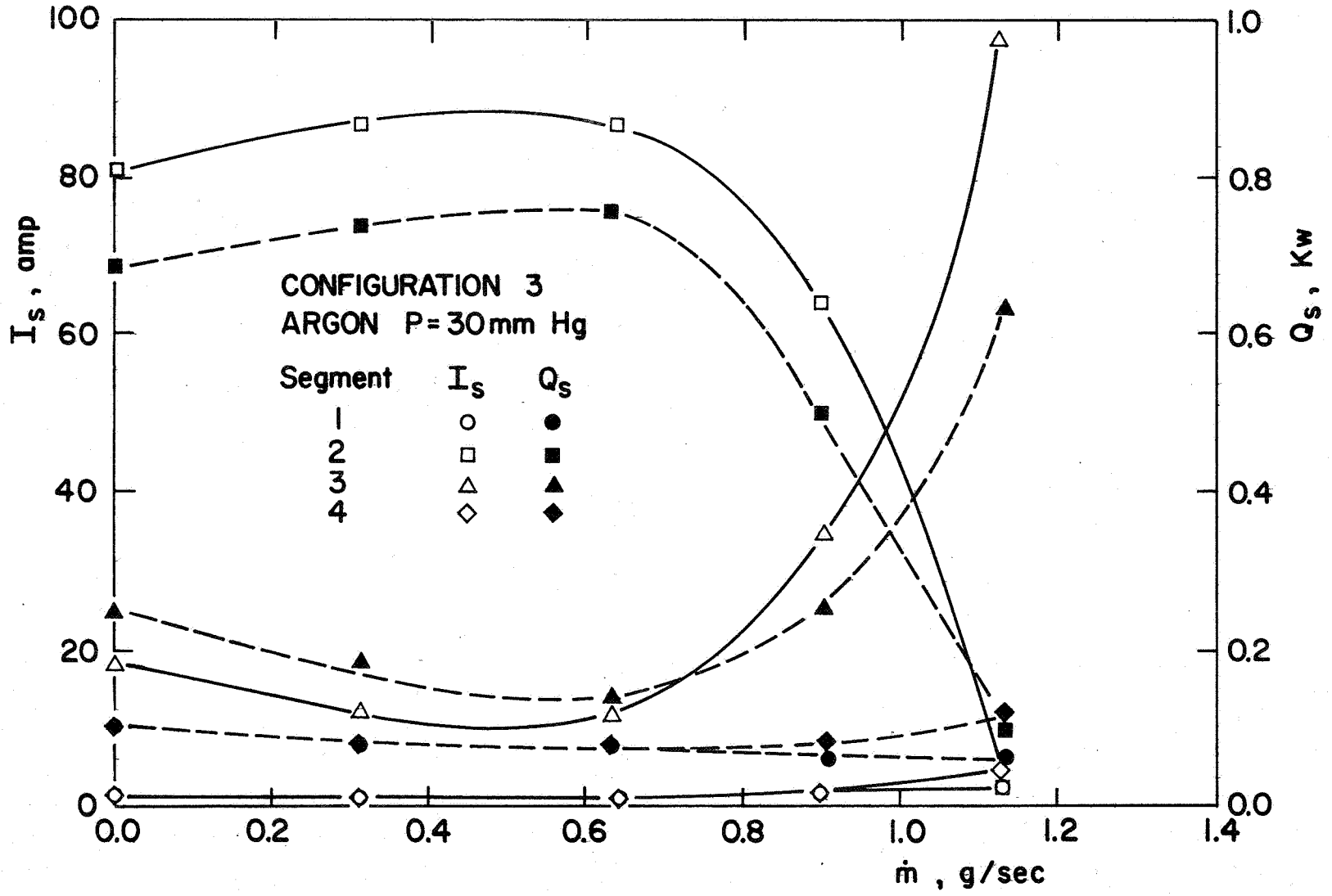

FIGURE 29 SEGMENTAL CURRENT AND HEAT FLUX DISTRIBUTION VS. MASS FLOW RATE (B=0)

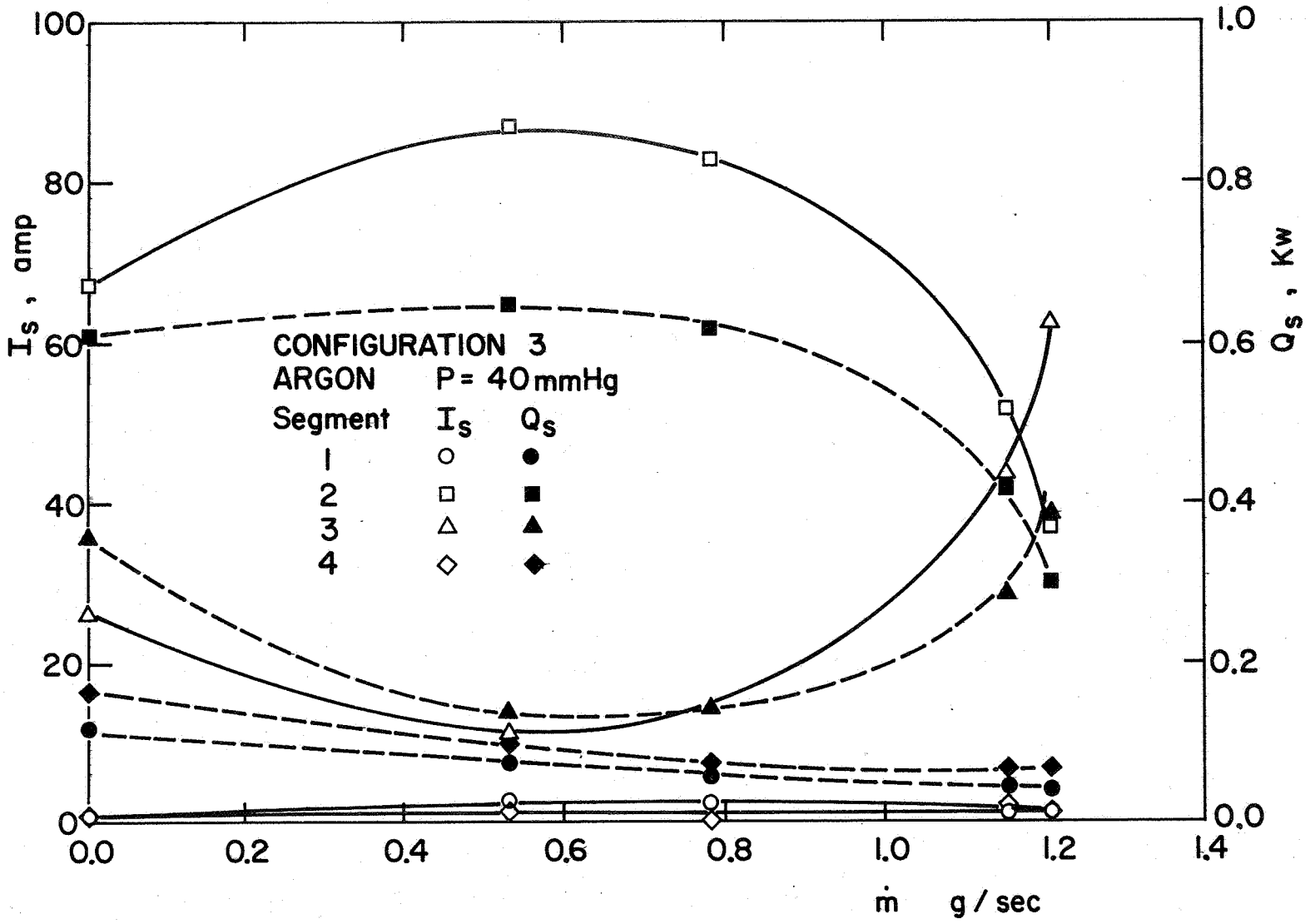

FIGURE 30 SEGMENTAL CURRENT AND HEAT FLUX DISTRIBUTION VS. MASS FLOW RATE (B=0)

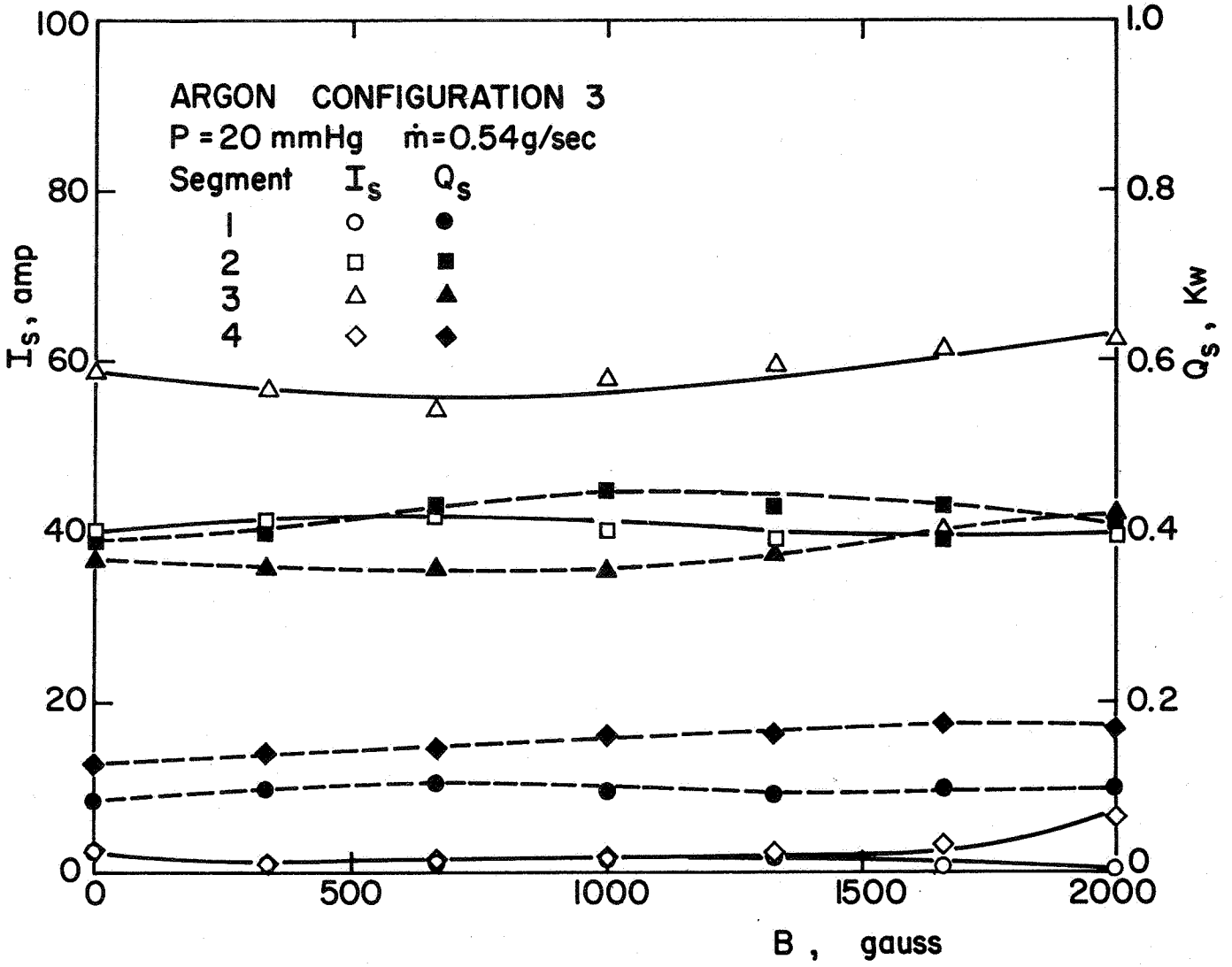

FIGURE 31 SEGMENTAL CURRENT AND HEAT FLUX DISTRBUTION VS. MAGNETIC FIELD STRENGTH

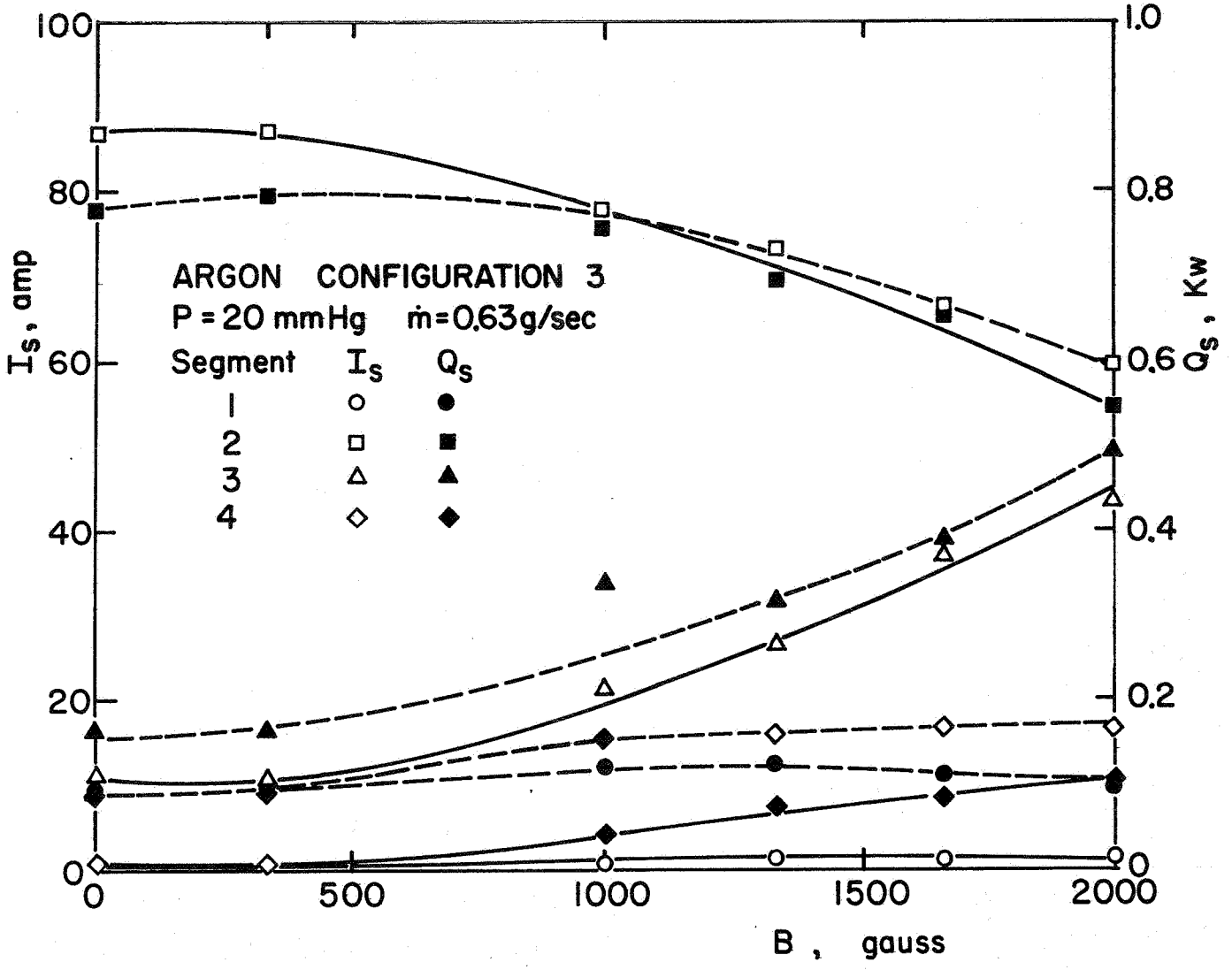

FIGURE 32 SEGMENTAL CURRENT AND HEAT FLUX DISTRIBUTION VS. MAGNETIC FIELD STRENGTH

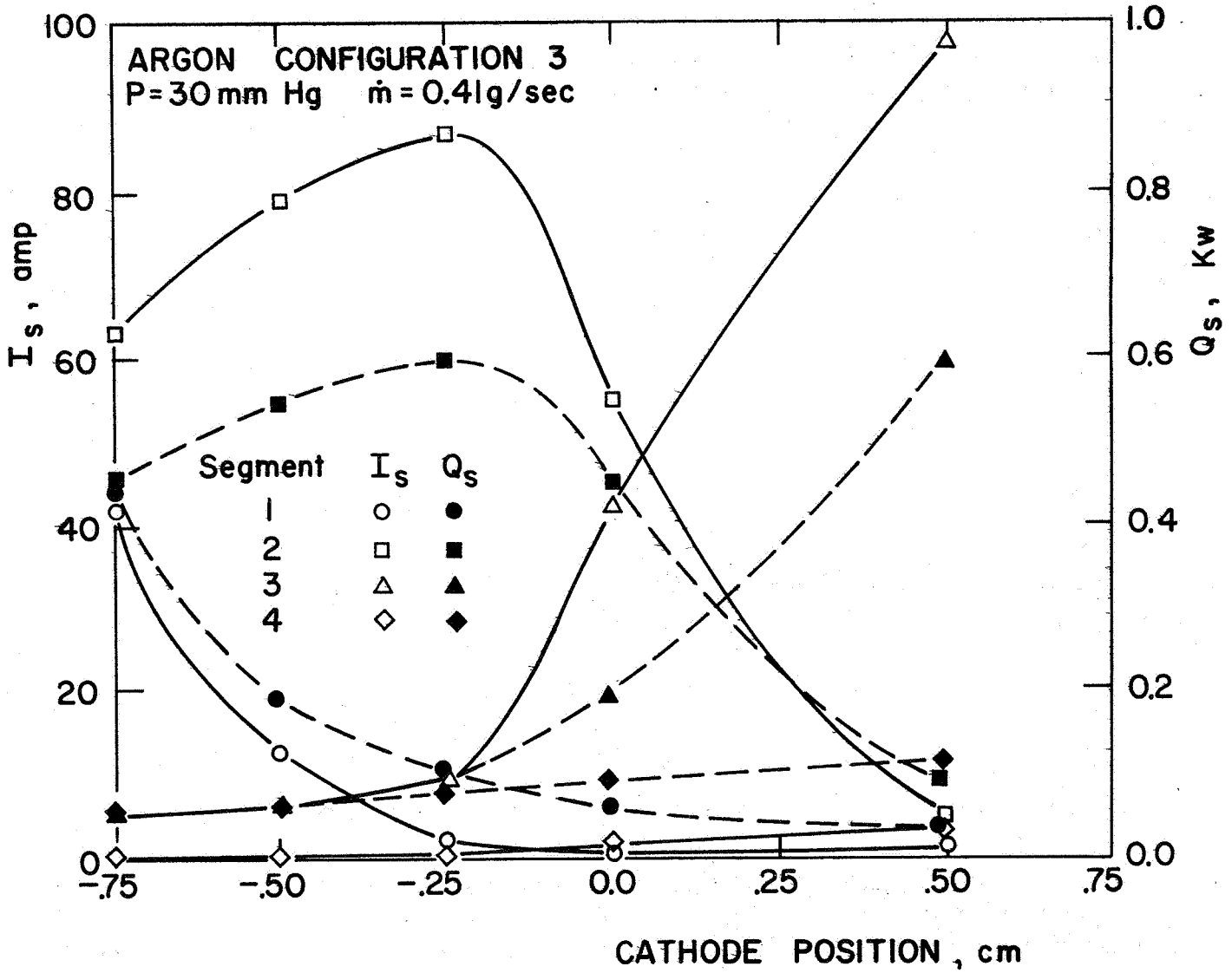

FIGURE 33 SEGMENTAL CURRENT AND HEAT FLUX DISTRIBUTION VS. CATHODE POSITION (B=0)

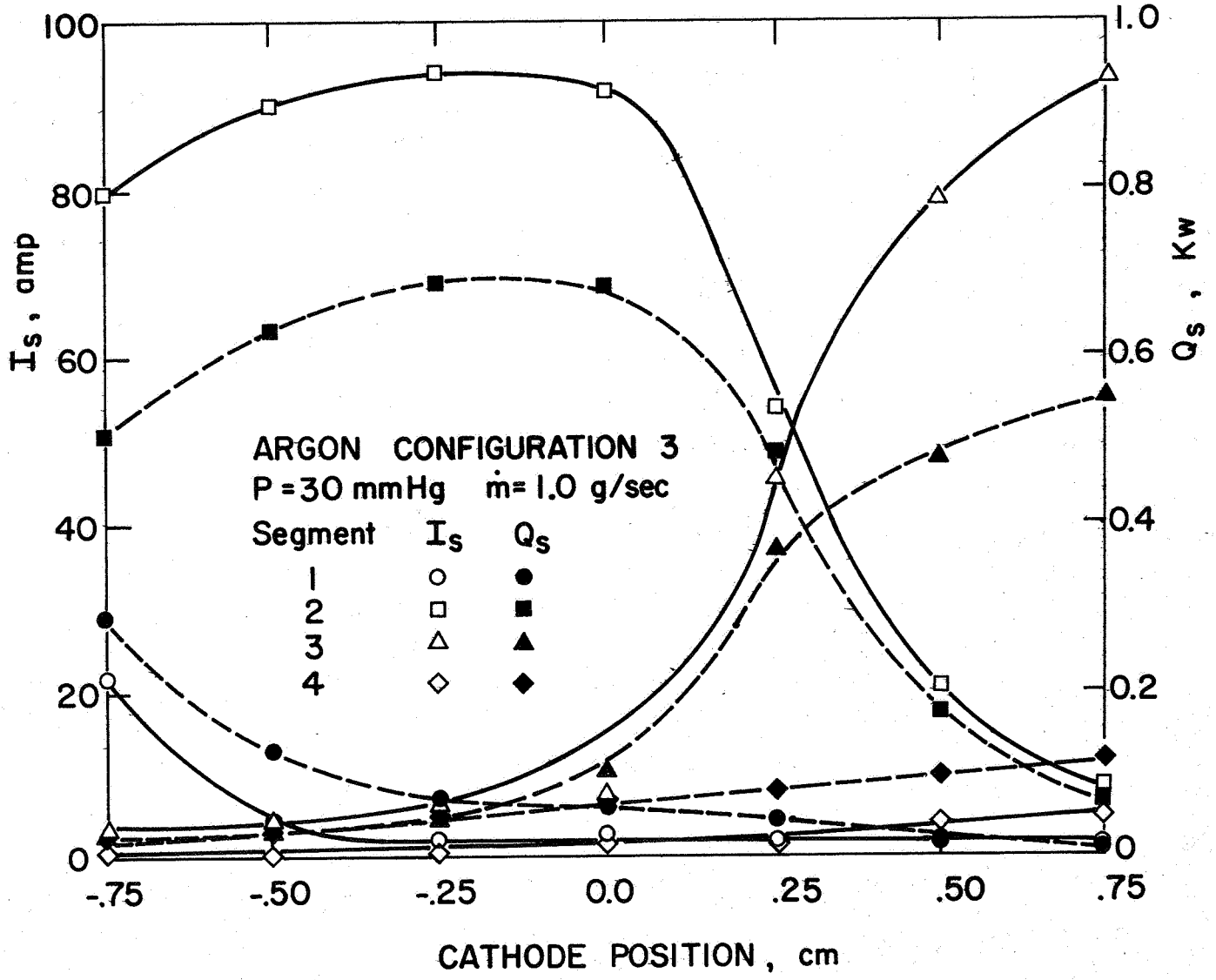

FIGURE 34 SEGMENTAL CURRENT AND HEAT FLUX DISTRIBUTION VS. CATHODE POSITION (B=0)

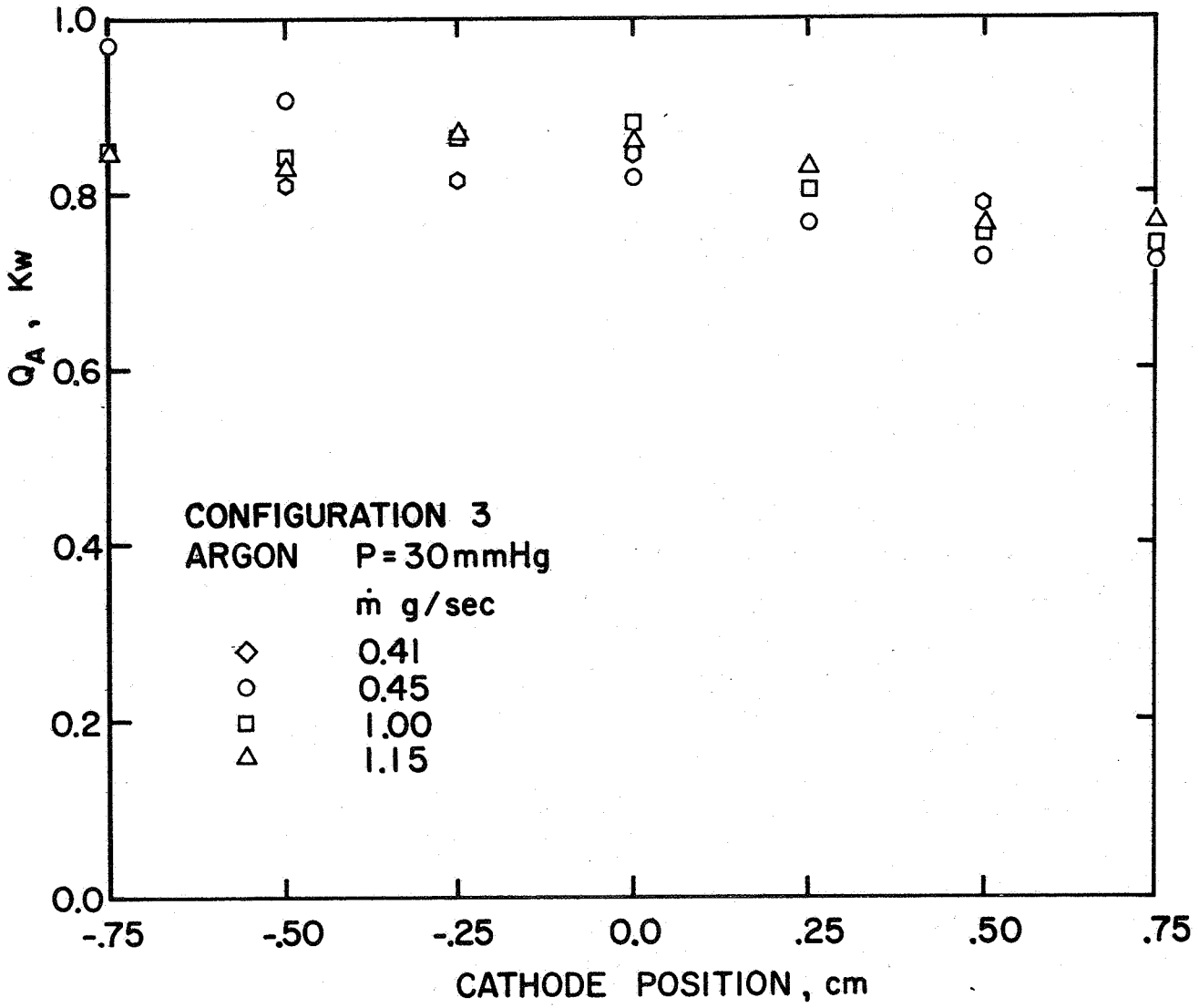

FIGURE 35 TOTAL ENERGY TO THE ANODE VS. CATHODE POSITION (B=0)

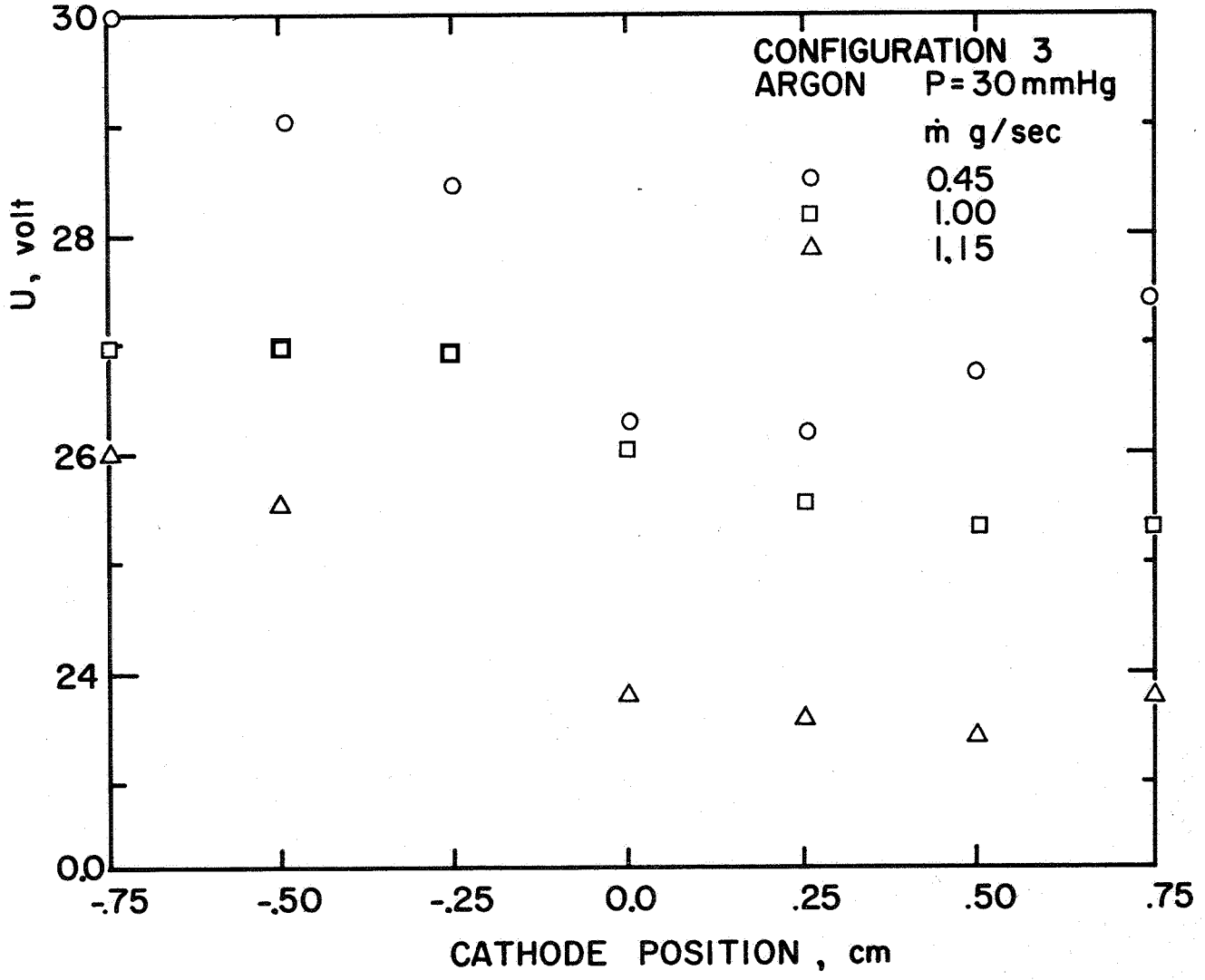

FIGURE 36 ARC VOLTAGE VS. CATHODE POSITION (B=0)

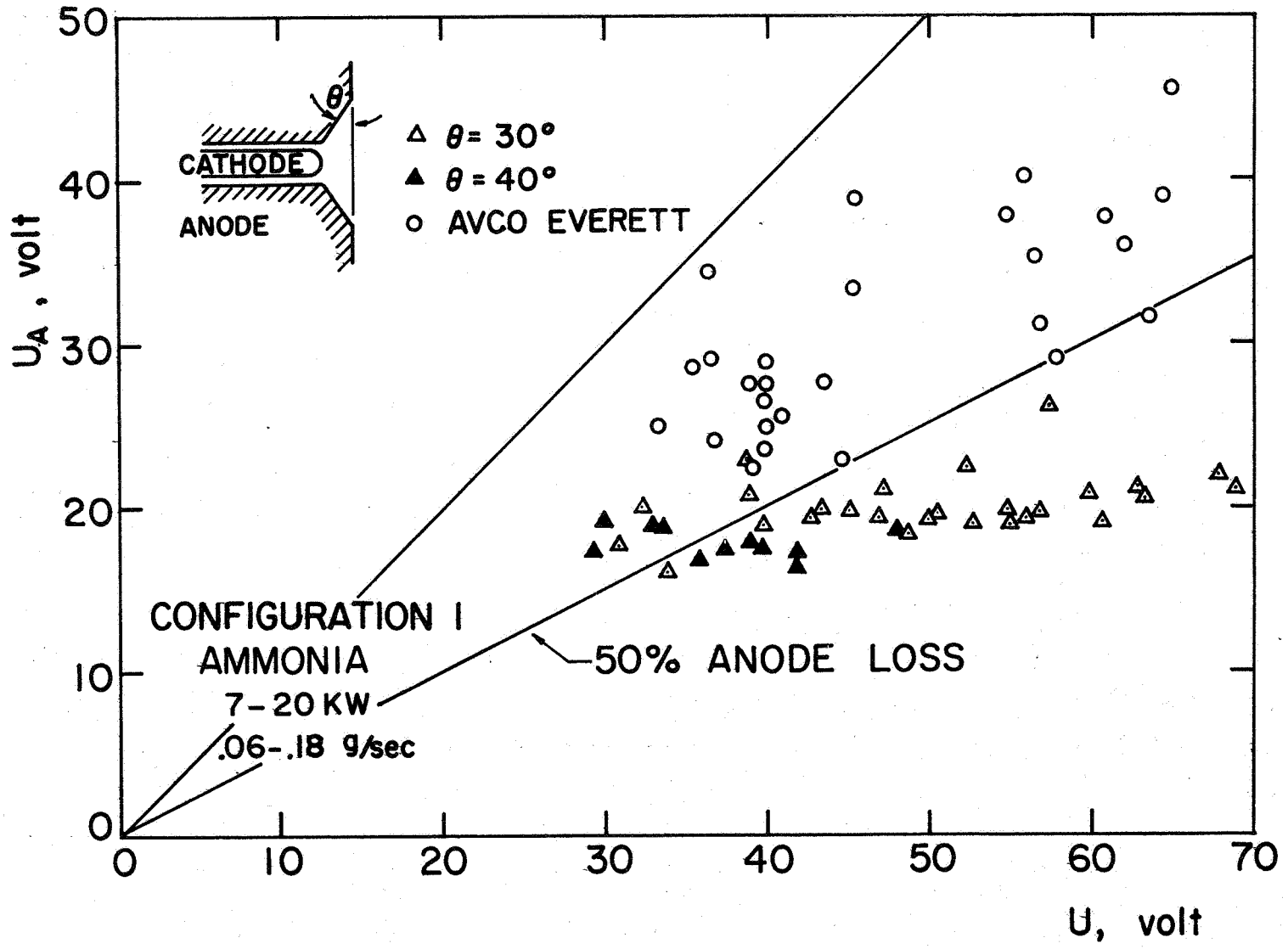

FIGURE 37 CHARACTERISTIC ANODE VOLTAGE VERSUS ARC VOLTAGE

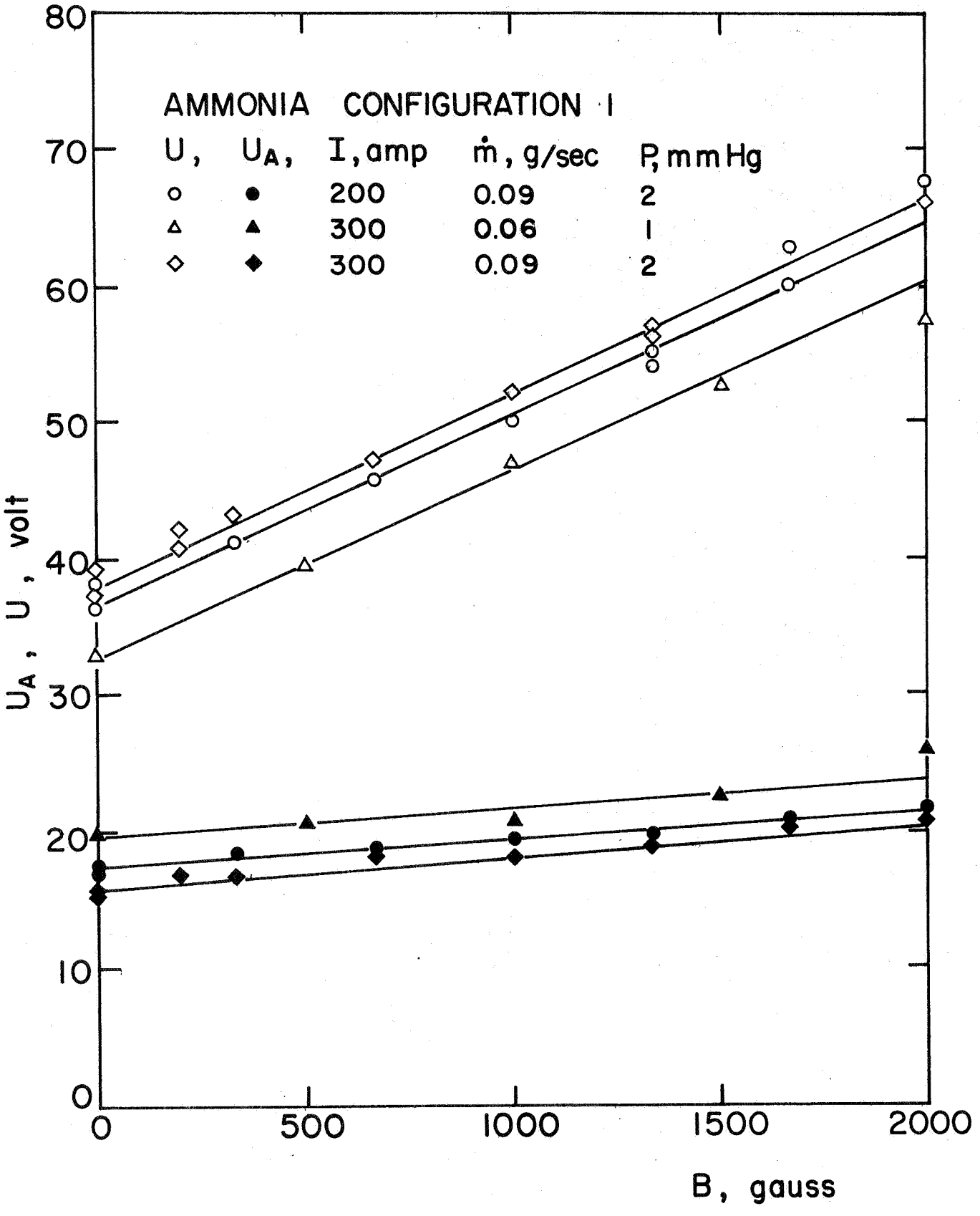

FIGURE 38 ARC VOLTAGE AND CHARACTERISTIC ANODE VOLTAGE VERSUS MAGNETIC FIELD STRENGTH

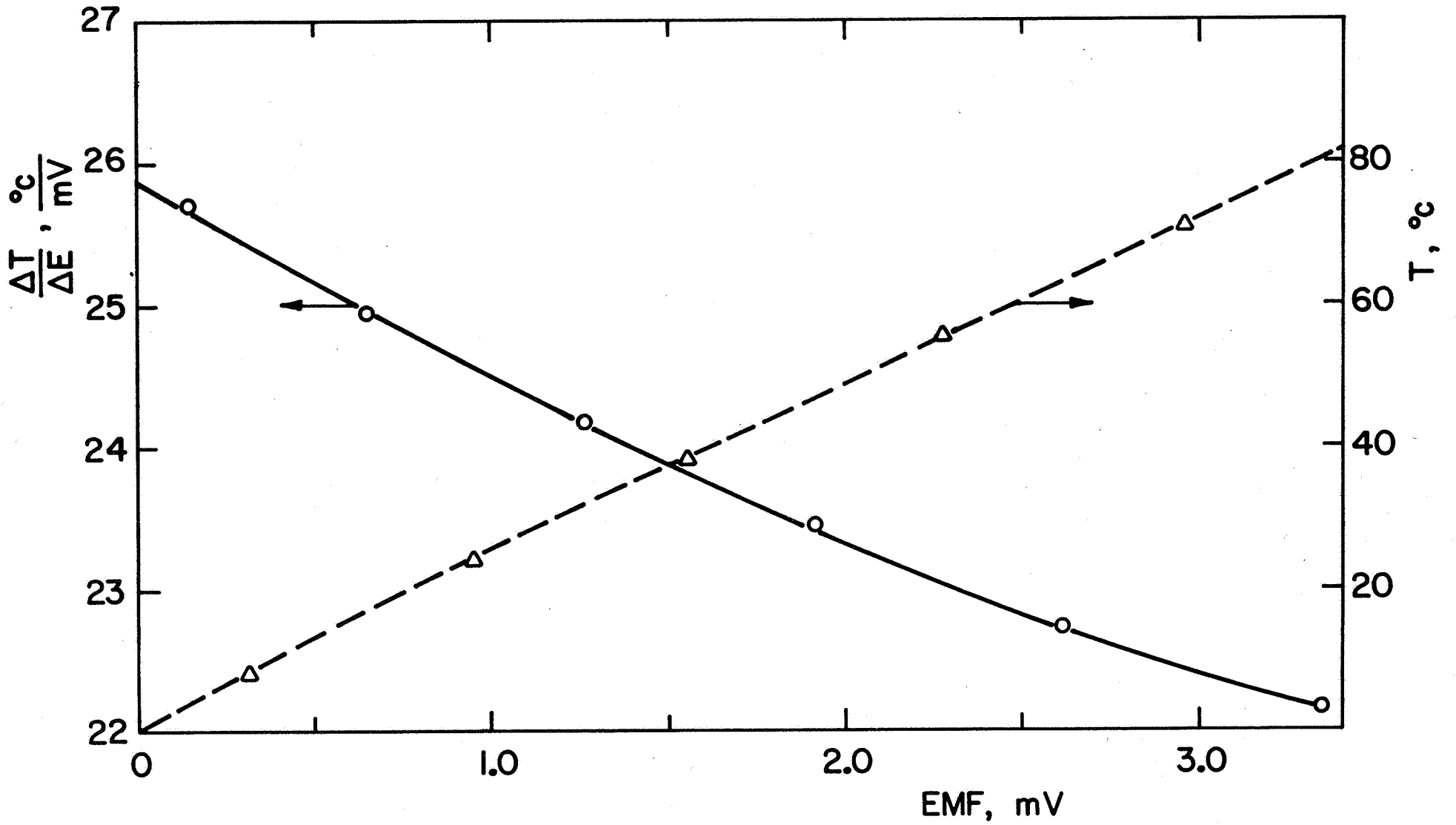

FIGURE AI CALIBRATION OF THERMOCOUPLE (B-1114)

CALIBRATION OF FLOW METERS

Meter reading	10	20	30	40	50	60	70	80	90	100
Anode	.0432	.0863	.1294	.1726	.2158	.2589	.3020	.3452	.3884	.4315
M.H.E.	.0234	.0468	.0701	.0935	.1169	.1403	.1637	.1870	.2104	.2338
Cathode	.0052	.0104	.0156	.0208	.0260	.0312	.0364	.0416	.0468	.0520
Water Jacket	.0123	.0246	.0369	.0492	.0616	.0739	.0862	.0985	.1108	.1231
H.E.	.0494	.0989	.1484	.1978	.2472	,2967	.3462	.3956	.4450	.4945

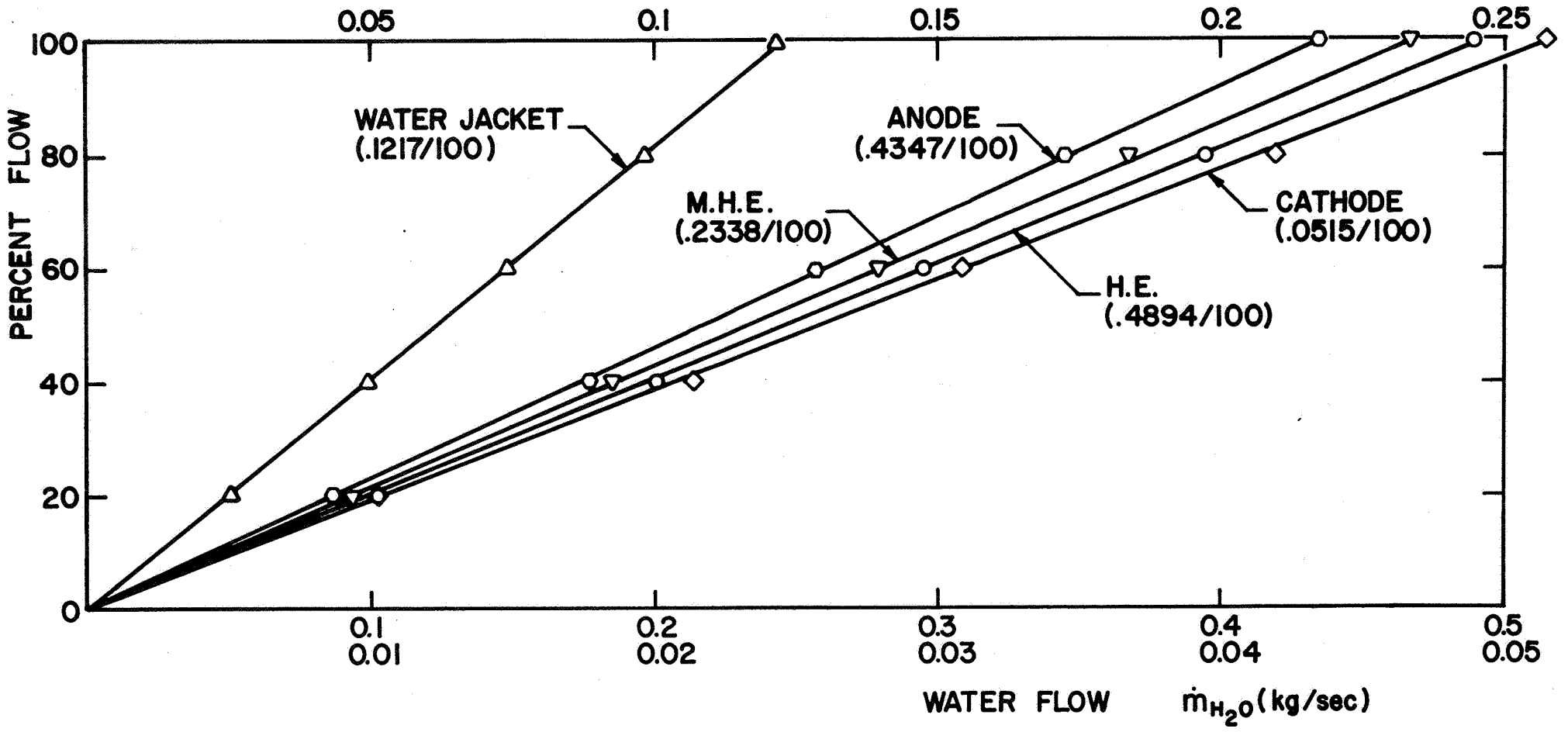

FIGURE A2 CALIBRATION OF WATER FLOWRATORS

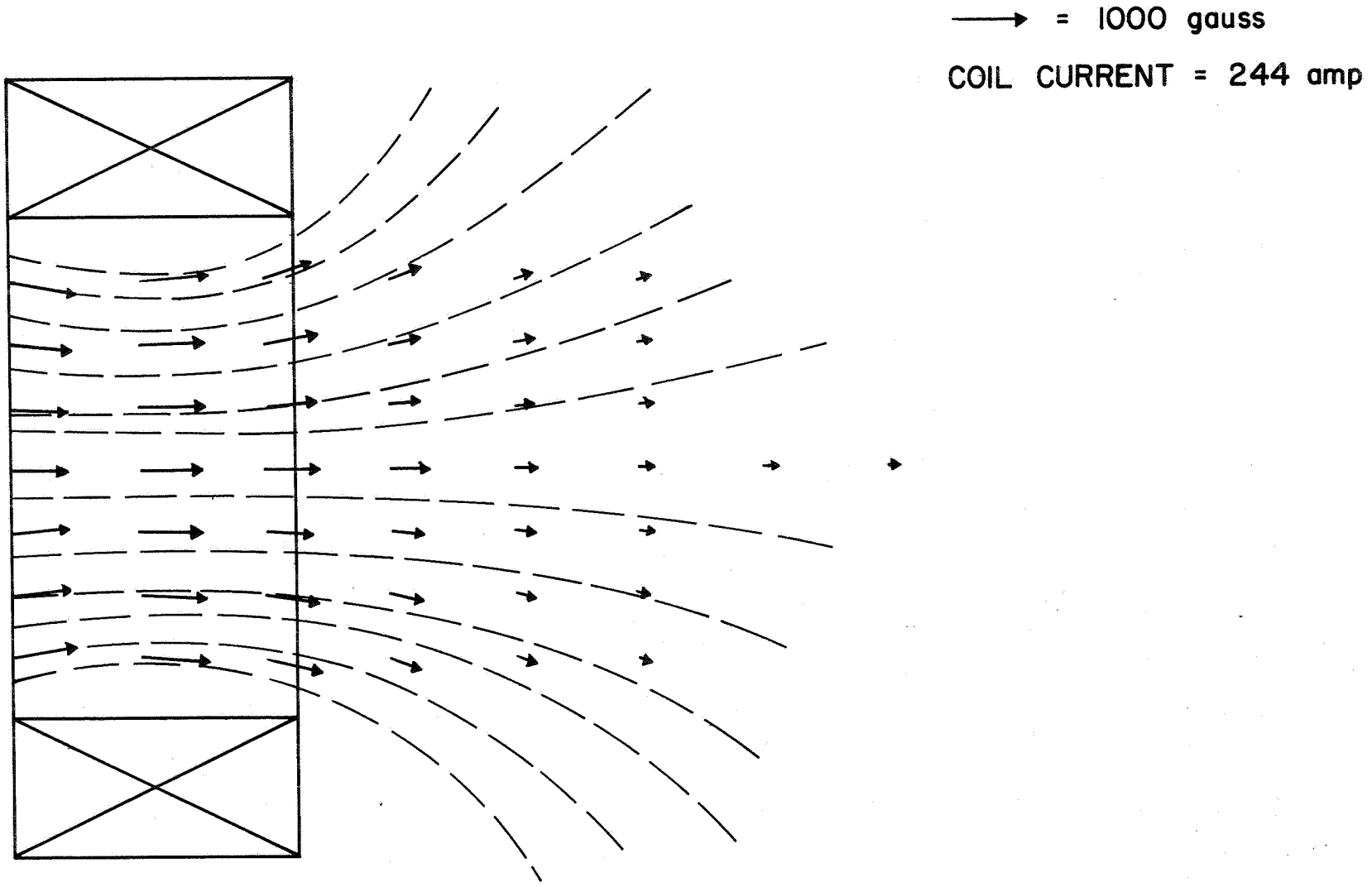

FIGURE A3 MAP OF MAGNETIC FIELD DISTRIBUTION

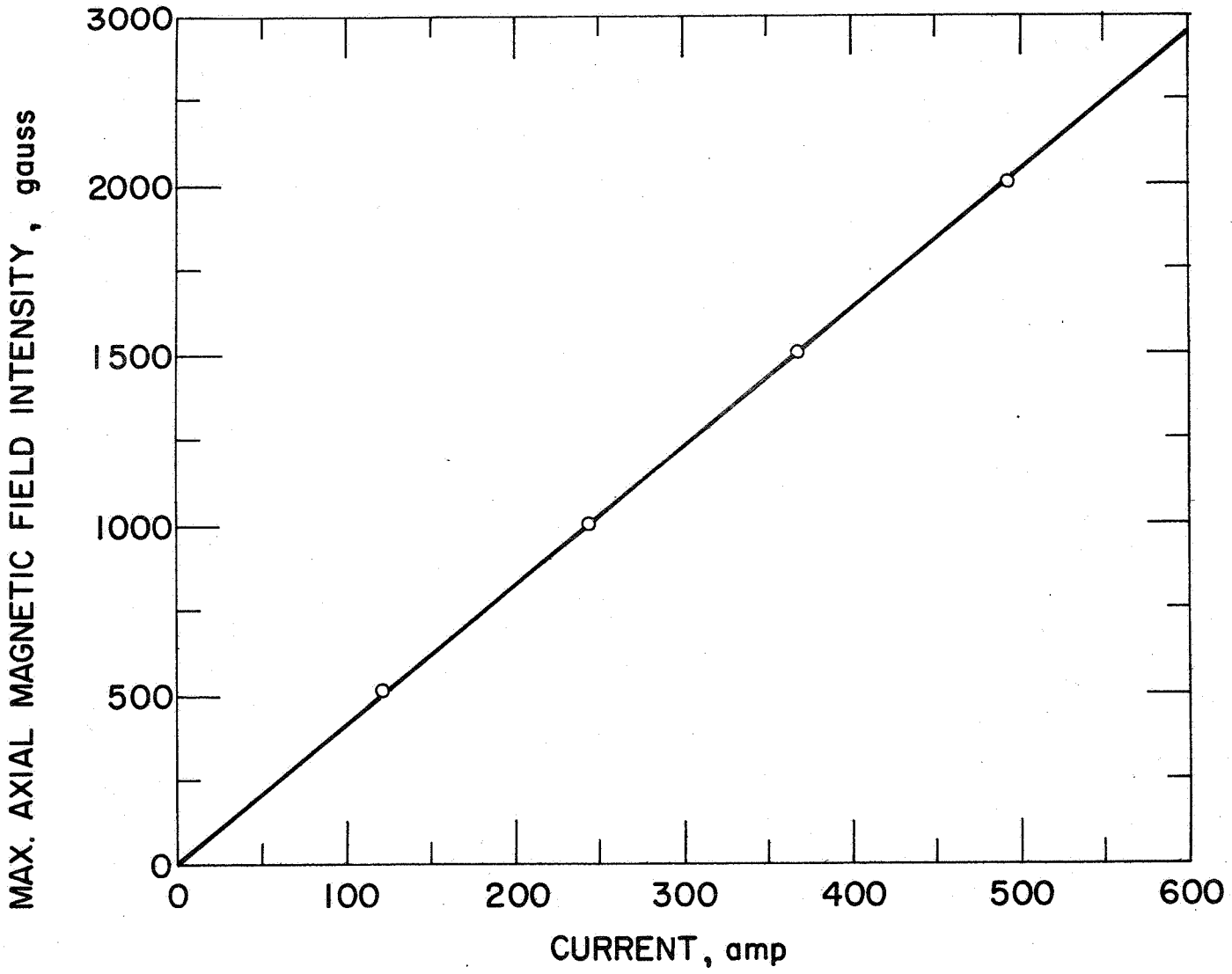

FIGURE A4 MAXIMUM MAGNETIC FIELD INTENSITY VERSUS CURRENT

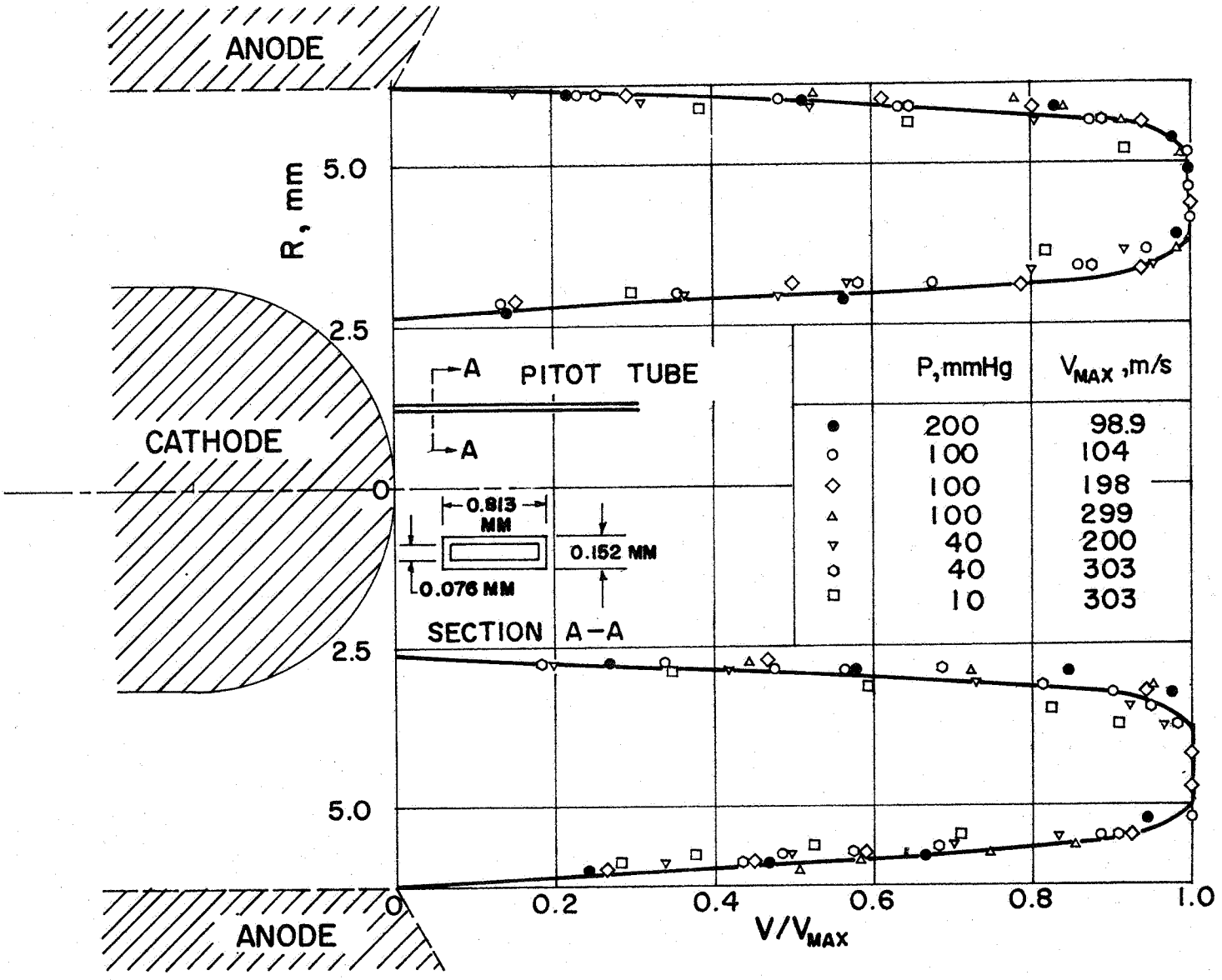

FIGURE A.5 COLD FLOW VELOCITY PROFILES